

## AN ABSTRACT OF THE DISSERTATION OF

Douglas N. Woods for the degree of Doctor of Philosophy in Nuclear Engineering  
presented on June 4, 2018.

Title: Discrete Ordinates Radiation Transport using High-Order Finite Element  
Spatial Discretizations on Meshes with Curved Surfaces

Abstract approved:

---

Todd S. Palmer

We spatially discretize the  $S_N$  transport equation using the high-order (HO) discontinuous finite element method (DFEM) on HO meshes. Previous work provided a proof-of-concept for this spatial discretization method in  $X$ - $Y$  geometry. Included in the present work, we derive a spatial discretization for the  $S_N$  transport equation in  $R$ - $Z$  geometry using HO DFEMs on HO meshes. We characterize the behavior of these methods by solving several numerical test problems. We conclude that the spatial discretization error is dependent upon the angular discretization, the spatial error converges at  $O(p + 1)$  on problems with smooth solutions, the spatial error converges at  $O(3/2)$  for solutions with less regularity, and preserving axisymmetry is a function of finite element order and spatial mesh resolution. Specifically, this method preserves the one-dimensional spherical geometry solution using a smooth manufactured solution.

We also derive and implement a vacuum boundary condition for the modified interior penalty (MIP) diffusion synthetic acceleration (DSA) method to accelerate the source iteration. The testing we perform reveals substantially faster convergence rates in the optically thin and intermediate regimes, while degrading the convergence rates in optically thick regimes when compared to the original MIP DSA equations.

©Copyright by Douglas N. Woods

June 4, 2018

All Rights Reserved

Discrete Ordinates Radiation Transport using High-Order Finite Element Spatial  
Discretizations on Meshes with Curved Surfaces

by  
Douglas N. Woods

A DISSERTATION

submitted to

Oregon State University

in partial fulfillment of  
the requirements for the  
degree of

Doctor of Philosophy

Presented June 4, 2018  
Commencement June 2018

Doctor of Philosophy dissertation of Douglas N. Woods presented on June 4, 2018.

APPROVED:

---

Major Professor, representing Nuclear Engineering

---

Head of the School of Nuclear Science and Engineering

---

Dean of the Graduate School

I understand that my dissertation will become part of the permanent collection of Oregon State University libraries. My signature below authorizes release of my dissertation to any reader upon request.

---

Douglas N. Woods, Author

## ACKNOWLEDGEMENTS

I first want to thank my Lord and Savior for the opportunities and gifts I've been given. I want to thank my major advisor, Dr. Todd Palmer, for piquing my interest in transport discretizations during the advanced courses he taught. He found and presented the opportunity to work on this project, brought immense knowledge, and has been encouraging throughout this entire project. Thanks to Dr. Tom Brunner for serving as my mentor during a summer at Lawrence Livermore National Laboratory and giving me an inordinate amount of time, patience, and attention throughout this degree process. I must thank my parents for being so encouraging, supportive, and loving during my life. All of my family has been so patient with me – I too often neglected visiting them despite my relatively close proximity at Oregon State.

## TABLE OF CONTENTS use “\conheading” in .toc

	<u>Page</u>
1 Introduction	1
1.1 Radiation Transport	3
1.2 Discretization	4
1.2.1 Direction of Travel Discretization	5
1.2.2 Spatial Discretization	6
1.2.3 High Order Finite Elements	7
1.2.4 Meshes	8
1.3 Diffusion Limit	9
1.4 Source Iteration Acceleration	11
1.5 <i>R-Z</i> Geometry	14
1.6 Axisymmetry	15
1.7 Research Objectives	16
1.8 Outline	16
2 Methods	18
2.1 High Order DFEM	18
2.2 Meshes with Curved Surfaces	20
2.3 Solution Method	22
3 Diffusion Synthetic Acceleration	23
3.1 Modified Interior Penalty DSA	25
3.1.1 Spectral Radius Sensitivity to Constant $C$	27
3.1.2 Sensitivity of the Spectral Radius to the Scattering Ratio $c$	32
3.1.3 Infinite Medium MIP DSA Results	33

## TABLE OF CONTENTS (Continued)

	<u>Page</u>
3.2 MIP DSA with Robin Boundary Conditions . . . . .	35
3.2.1 Accuracy . . . . .	36
3.2.2 Sensitivity Study of the Spectral Radius . . . . .	38
3.3 Conclusions . . . . .	42
4 <i>R-Z</i> Geometry . . . . .	43
4.1 Angular Discretization . . . . .	45
4.1.1 Reflecting Boundary at $r = 0$ . . . . .	48
4.2 Spatial Discretization . . . . .	50
4.3 Spatial Convergence Study . . . . .	54
4.3.1 Uniform Infinite Medium . . . . .	54
4.3.2 Angular Dependence Study . . . . .	54
4.3.3 Spatial Convergence Study . . . . .	56
4.4 Axisymmetry Preservation . . . . .	63
4.4.1 Low-Order Mesh . . . . .	65
4.4.2 High-Order Mesh . . . . .	89
4.4.3 Axisymmetry Summary and Discussion . . . . .	112
4.5 Strong Scatter with Alternating Boundaries Test . . . . .	116
4.6 Material Discontinuity Stress Test . . . . .	117
4.7 <i>R-Z</i> Geometry Conclusions . . . . .	118
5 Conclusions . . . . .	124
5.1 FutureWork . . . . .	125

A	Implementation in MFEM	132
A.1	Transport Operators	133
A.2	MIP DSA Operators	134
B	Mesh Examples	139
C	Supplementary Results in $X$ - $Y$ Geometry	140
C.1	Uniform Infinite Medium	140
C.2	Spatial Convergence Study	140
C.3	Alternating Incident Boundary Condition	142
D	Alternative Implementations for DSA with Robin Boundary Conditions	145
E	Mathematica Scripts	147
E.1	Mass Matrix Entries for RZ BLD Gauss-Legendre on Quadrilaterals	147
E.2	Angular Redistribution Matrix Entries for RZ BLD Gauss-Legendre on Quadrilaterals	150
E.3	r-Leakage Matrix Entries for RZ BLD Gauss-Legendre on Quadrilaterals	153
E.4	z-Leakage Matrix Entries for RZ BLD Gauss-Legendre on Quadrilaterals	155
E.5	z-Leakage Matrix Entries for RZ BLD Gauss-Legendre on Quadrilaterals	158
E.6	r Surface-Integral Matrix Entries for RZ BLD Gauss-Legendre on Quadri- laterals	161
E.7	z Surface-Integral Matrix Entries for RZ BLD Gauss-Legendre on Quadri- laterals	163
E.8	LinearForm Angular Redistribution Matrix Entries for RZ BLD Gauss- Legendre on Quadrilaterals	165
E.9	LinearForm Scattering/Fixed Source Matrix Entries for RZ BLD Gauss- Legendre on Quadrilaterals	167

## LIST OF FIGURES use “\contlofheading” in .lof

<u>Figure</u>		<u>Page</u>
1	The positive octant for $S_6$ level-symmetric angular quadrature. . . . .	6
2	Example of mapping the reference element to a physical element. . . . .	21
3	Spectral radius data for varying $p$ with $C = 2$ on an orthogonal mesh with homogeneous Dirichlet boundary conditions in the DSA solve; plot reproduced from Woods et al. [1]. . . . .	28
4	Spectral radius data for varying $p$ with $C = 4$ on an orthogonal mesh with homogeneous Dirichlet boundary conditions in the DSA solve; plot reproduced from Woods et al. [1]. . . . .	30
5	Spectral radius data for varying $p$ with $C = 6$ on an orthogonal mesh with homogeneous Dirichlet boundary conditions in the DSA solve; plot reproduced from Woods et al. [1]. . . . .	31
6	Spectral radius data for various scattering ratios $c$ using 4 <sup>th</sup> -order finite elements, constant $C = 4$ , and orthogonal mesh. . . . .	32
7	Spectral radius data for various scattering ratios $c$ using 4 <sup>th</sup> -order finite elements, constant $C = 4$ , and 3 <sup>rd</sup> -order mesh. . . . .	33
8	Spectral radius data for varying $p$ with $C = 2$ on a periodic orthogonal mesh. . . . .	33
9	Spectral radius data for varying $p$ with $C = 4$ on a periodic orthogonal mesh. . . . .	34
10	Spectral radius data for varying $p$ with $C = 6$ on a periodic orthogonal mesh. . . . .	34
11	Spectral radius data for varying $p$ with $C = 2$ on an orthogonal mesh using the vacuum boundary MIP DSA method. . . . .	39

## LIST OF FIGURES (Continued)

<u>Figure</u>		<u>Page</u>
12 Spectral radius data for varying $p$ with $C = 4$ on an orthogonal mesh using the zero incident current DSA method. . . . .		40
13 Spectral radius data for varying $p$ with $C = 6$ on an orthogonal mesh using the zero incident current DSA method. . . . .		41
14 Cylindrical space-angle coordinate system showing the position $(r, z)$ and direction of travel $\Omega$ . . . . .		44
15 Angular discretization showing $(\xi, \mu)$ pairs; adapted from [2] . . . . .		46
16 Example of incident and outgoing surface. . . . .		54
17 Uniform infinite medium solution. . . . .		55
18 MMS solution for Equation 74. . . . .		56
19 MMS solution for Equation 75. . . . .		57
20 MMS solution to Equation 76. . . . .		58
21 $L^2$ -norm of the errors from the manufactured solution and reference lines, where $N_{\text{unknowns}} = N_{\text{cells}}(p + 1)^2$ . . . . .		59
22 MMS solution to Equation 77. . . . .		61
23 $L^2$ -norm of the errors from the manufactured solution and reference lines, where $N_{\text{unknowns}} = N_{\text{cells}}(p + 1)^2$ . . . . .		62
24 Relative asymmetry for 1 <sup>st</sup> -order finite elements on a 1 <sup>st</sup> -order mesh for given order of level-symmetric angular quadrature. . . . .		67
25 Measure of the asymmetry for each finite element node for the given level-symmetric angular quadrature order for 1 <sup>st</sup> -order DFEM and 1 <sup>st</sup> -order mesh with 120 zones (see Figure 24). . . . .		68

26	Accuracy of solutions for given angular quadrature using $p = 1$ on a 1 <sup>st</sup> -order mesh with 120 zones. . . . .	68
27	Relative asymmetry for 2 <sup>st</sup> -order finite elements on a 1 <sup>st</sup> -order mesh for given order of level-symmetric angular quadrature. . . . .	70
28	Measure of the asymmetry for each finite element node for the given level-symmetric angular quadrature order for 2 <sup>nd</sup> -order DFEM and 1 <sup>st</sup> -order mesh with 120 zones (see Figure 27). . . . .	71
29	Accuracy of solutions for given angular quadrature using $p = 2$ on a 1 <sup>st</sup> -order mesh with 120 zones. . . . .	71
30	Relative asymmetry for 4 <sup>st</sup> -order finite elements on a 1 <sup>st</sup> -order mesh for given order of level-symmetric angular quadrature. . . . .	73
31	Measure of the asymmetry for each finite element node for the given level-symmetric angular quadrature order for 4 <sup>th</sup> -order DFEM and 1 <sup>st</sup> -order mesh with 120 zones (see Figure 30). . . . .	74
32	Accuracy of solutions for given angular quadrature using $p = 4$ on a 1 <sup>st</sup> -order mesh with 120 zones. . . . .	74
33	Relative asymmetry for 8 <sup>st</sup> -order finite elements on a 1 <sup>st</sup> -order mesh for given order of level-symmetric angular quadrature. . . . .	76
34	Measure of the asymmetry for each finite element node for the given level-symmetric angular quadrature order for 8 <sup>th</sup> -order DFEM and 1 <sup>st</sup> -order mesh with 120 zones (see Figure 33). . . . .	77
35	Accuracy of solutions for given angular quadrature using $p = 8$ on a 1 <sup>st</sup> -order mesh with 120 zones. . . . .	77
36	Relative asymmetry for $p = \{1, 2, 4\}$ finite elements on a 1 <sup>st</sup> -order mesh with 120 zones for $S_8$ level-symmetric angular quadrature. . . . .	79

37	Measure of the asymmetry for each finite element node for the given finite element order using $S_8$ level-symmetric angular quadrature on a 1 <sup>st</sup> -order mesh with 120 zones (see Figure 36). . . . .	80
38	Accuracy of solutions for given finite element order using $S_8$ level-symmetric angular quadrature on a 1 <sup>st</sup> -order mesh with 120 zones. . . . .	80
39	Relative asymmetry for $p = 1$ finite elements on a 1 <sup>st</sup> -order mesh for $S_8$ level-symmetric angular quadrature for $N_{\text{zones}} = \{6, 28, 120\}$ . . . . .	82
40	Relative asymmetry for $p = 1$ finite elements on a 1 <sup>st</sup> -order mesh for $S_8$ level-symmetric angular quadrature for $N_{\text{zones}} = \{496, 2016, 8128\}$ ; mesh overlay may be removed for clarity. . . . .	83
41	Measure of the asymmetry for each finite element node for 1 <sup>th</sup> -order finite elements using $S_8$ level-symmetric angular quadrature on a 1 <sup>st</sup> -order mesh with various number of zones (see Figures 39-40). . . . .	84
42	Accuracy of solutions for given mesh refinement for $p = 1$ using $S_8$ level-symmetric angular quadrature on a 1 <sup>st</sup> -order mesh. . . . .	84
43	Relative asymmetry for $p = 4$ finite elements on a 1 <sup>st</sup> -order mesh for $S_8$ level-symmetric angular quadrature for $N_{\text{zones}} = \{6, 28, 120\}$ . . . . .	86
44	Relative asymmetry for $p = 4$ finite elements on a 1 <sup>st</sup> -order mesh for $S_8$ level-symmetric angular quadrature for $N_{\text{zones}} = \{496, 2016, 8128\}$ ; mesh overlay may be removed for clarity. . . . .	87
45	Measure of the asymmetry for each finite element node for 4 <sup>th</sup> -order finite elements using $S_8$ level-symmetric angular quadrature on a 1 <sup>st</sup> -order mesh with various number of zones (see Figures 43-44). . . . .	88
46	Accuracy of solutions for given mesh refinement for $p = 4$ using $S_8$ level-symmetric angular quadrature on a 1 <sup>st</sup> -order mesh. . . . .	88

47	Relative asymmetry for 1 <sup>st</sup> -order finite elements on a 2 <sup>nd</sup> -order mesh for given order of level-symmetric angular quadrature. . . . .	90
48	Measure of the asymmetry for each finite element node for the given level-symmetric angular quadrature order for 1 <sup>st</sup> -order DFEM and 2 <sup>nd</sup> -order mesh with 120 zones (see Figure 47). . . . .	91
49	Accuracy of solutions for given angular quadrature using $p = 1$ on a 2 <sup>nd</sup> -order mesh with 120 zones. . . . .	91
50	Relative asymmetry for 2 <sup>nd</sup> -order finite elements on a 2 <sup>nd</sup> -order mesh for given order of level-symmetric angular quadrature. . . . .	93
51	Measure of the asymmetry for each finite element node for the given level-symmetric angular quadrature order for 2 <sup>nd</sup> -order DFEM and 2 <sup>nd</sup> -order mesh with 120 zones (see Figure 50). . . . .	94
52	Accuracy of solutions for given angular quadrature using $p = 2$ on a 2 <sup>nd</sup> -order mesh with 120 zones. . . . .	94
53	Relative asymmetry for 4 <sup>th</sup> -order finite elements on a 2 <sup>nd</sup> -order mesh for given order of level-symmetric angular quadrature. . . . .	96
54	Measure of the asymmetry for each finite element node for the given level-symmetric angular quadrature order for 4 <sup>th</sup> -order DFEM and 2 <sup>nd</sup> -order mesh with 120 zones (see Figure 53). . . . .	97
55	Accuracy of solutions for given angular quadrature using $p = 4$ on a 2 <sup>nd</sup> -order mesh with 120 zones. . . . .	97
56	Relative asymmetry for $p = \{1, 2, 4\}$ finite elements on a 2 <sup>nd</sup> -order mesh for $S_8$ level-symmetric angular quadrature. . . . .	99
57	Measure of the asymmetry for each finite element node for the given finite element order using $S_8$ level-symmetric angular quadrature on a 2 <sup>nd</sup> -order mesh with 120 zones (see Figure 56). . . . .	100

58	Accuracy of solutions for given angular quadrature using $S_8$ level-symmetric angular quadrature on a 2 <sup>nd</sup> -order mesh with 120 zones. . . . .	100
59	Relative asymmetry for $p = 1$ finite elements on a 2 <sup>nd</sup> -order mesh for $S_8$ level-symmetric angular quadrature. . . . .	102
60	Relative asymmetry for $p = 1$ finite elements on a 2 <sup>nd</sup> -order mesh for $S_8$ level-symmetric angular quadrature; mesh overlay may be removed for clarity. . . . .	103
61	Measure of the asymmetry for each finite element node for 1 <sup>st</sup> -order finite elements using $S_8$ level-symmetric angular quadrature on a 2 <sup>nd</sup> -order mesh with various number of zones (see Figures 59-60). . . . .	104
62	Accuracy of solutions for mesh refinement study using $p = 1$ , $S_8$ level-symmetric angular quadrature, on a 2 <sup>nd</sup> -order mesh. . . . .	104
63	Relative asymmetry for $p = 4$ finite elements on a 2 <sup>nd</sup> -order mesh for $S_8$ level-symmetric angular quadrature. . . . .	106
64	Relative asymmetry for $p = 4$ finite elements on a 2 <sup>nd</sup> -order mesh for $S_8$ level-symmetric angular quadrature; mesh overlay may be removed for clarity. . . . .	107
65	Measure of the asymmetry for each finite element node for 4 <sup>th</sup> -order DFEM, $S_8$ level-symmetric angular quadrature, and 2 <sup>nd</sup> -order mesh with various number of zones (see Figures 63 - 64). . . . .	108
66	Accuracy of solutions for mesh refinement study using $p = 4$ , $S_8$ level-symmetric angular quadrature, on a 2 <sup>nd</sup> -order mesh. . . . .	108
67	Relative asymmetry for $p = 1$ finite elements on a 2 <sup>nd</sup> -order mesh with 8128 zones; mesh overlay may be removed for clarity. . . . .	110

68	Measure of the asymmetry for each finite element node for the given level-symmetric angular quadrature order for 1 <sup>st</sup> -order DFEM and 2 <sup>nd</sup> -order mesh with 8128 zones. . . . .	111
69	Accuracy of solutions for given angular quadrature using $p = 4$ on a 2 <sup>nd</sup> -order mesh with 8128 zones. . . . .	111
70	Measure of the asymmetry for each finite element node for the given level-symmetric angular quadrature order for 1 <sup>st</sup> -order DFEM on the given mesh with 120 zones. . . . .	112
71	Measure of the asymmetry for each finite element node for the given level-symmetric angular quadrature order for 4 <sup>th</sup> -order DFEM on the given mesh with 120 zones. . . . .	113
72	Measure of the asymmetry for each finite element node for 4 <sup>th</sup> -order DFEM, $S_8$ level-symmetric angular quadrature, on the given mesh with various number of zones. . . . .	113
73	Analytic representation of each term of the transport equation using the manufactured solution, Equation 82, for $(\mu, \xi) \approx (0.218, 0.951)$ . The complicated shapes of the streaming and source terms are typical of the other $\Omega$ directions. . . . .	115
74	Strong scatter with discontinuous BCs with MIP DSA problem geometry; gray boundaries indicate incident boundary locations. . . . .	117
75	Solution to strong scatter with discontinuous boundary conditions with $p = 1$ finite elements and $S_4$ level-symmetric angular quadrature. White regions indicate negative scalar fluxes. . . . .	118
76	Solution to strong scatter with discontinuous boundary conditions with $p = 4$ finite elements and $S_8$ level-symmetric angular quadrature. White regions indicate negative scalar fluxes. . . . .	119

77	Solution to strong scatter with discontinuous boundary conditions with $p = 4$ finite elements and $S_{12}$ level-symmetric angular quadrature on a 2 <sup>nd</sup> -order mesh. White regions indicate negative scalar fluxes. . . . .	120
78	Material discontinuity stress test with MIP DSA problem geometry; materials defined in Table 4. . . . .	121
79	Solution to multi-material stress test. White regions indicate negative scalar fluxes. . . . .	122
80	Uniform infinite medium scalar flux solution. . . . .	140
81	MMS on a <i>highly</i> curved mesh. . . . .	141
82	Errors between the manufactured and DFEM solutions. Reference lines depict order of spatial convergence $O(n) \equiv O\left((N_{\text{zones}})^{n/2}\right)$ . . . . .	142
83	Alternating incident flux problem solution. . . . .	143
84	Scalar flux solution to alternating incident flux problem. . . . .	144

## LIST OF TABLES

<u>Table</u>	<u>Page</u>
1 Gaussian quadrature locations. . . . .	19
2 $L_2$ norm of the errors between the diffusion equation using the given boundary condition method and the reference solution (1-D analytic solution) using 3 <sup>rd</sup> -order elements, $C = 4$ , on an orthogonal mesh with 2304 zones. . . . .	37
3 Summary of discretizations and determination of whether they reduce the asymmetry. . . . .	114
4 Material discontinuity stress test with MIP DSA material properties. . . . .	118
5 MFEM transport operator function calls where the arguments have been dropped. . . . .	135
6 MFEM $R$ - $Z$ transport operator function calls where the arguments have been dropped. . . . .	136
7 MFEM default integration orders for transport operators. The notation for the finite element order is $p$ , mesh order is $g$ , and problem spatial dimension is $d$ . . . . .	137
8 MFEM diffusion equation function calls. . . . .	138
9 $L_2$ norm of the errors between the diffusion equation using the given boundary condition method and the reference solution (1-D analytic solution) using 3 <sup>rd</sup> -order elements, $C = 4$ , on an orthogonal mesh with 2304 zones. . . . .	147

# 1 Introduction

The solution to the radiation transport equation is valuable in the design and analysis of many physical systems. A few examples are nuclear reactors [3], medical radiation treatments [4], and high energy density physics systems like those found in astrophysics [5] or inertial confinement fusion (ICF). ICF experiments are being performed at facilities such as the National Ignition Facility<sup>1</sup> (NIF) and the Omega Laser Facility<sup>2</sup>. Nuclear fusion occurs in the high energy density physics (HEDP) regime where mass and energy densities of a material are very high [5, 6]. Since material temperatures are very high, materials emit black body radiation (also called thermal radiation) in tremendous quantities. This thermal radiation field deposits energy back to the material influencing the material internal energy, momentum, temperature, and density. This complicated system of thermal radiation transport with hydrodynamics is studied in radiation hydrodynamics. While all of the forces in these HEDP systems are important, we can develop some of the computational models independently. For instance, we may develop hydrodynamics model (and software tools) separately from those for radiation transport.

Lawrence Livermore National Laboratory (LLNL) is developing a hydrodynamics code called BLAST<sup>3</sup> [7]. BLAST solves the Euler equations using a general finite element method (FEM) on meshes with curved surfaces for the conservation of mass, energy, and momentum of a fluid [8]. Novel features include: higher-order elements to represent the thermodynamic and kinematic variables, and meshes with curved surfaces. Compared to the most common method, staggard grid hydrodynamics, Dobrev et al. [8] demonstrated that BLAST can more accurately model flow geometry, symmetry of radial flow, and an increased resolution of a shock front — observing

---

<sup>1</sup><https://lasers.llnl.gov>

<sup>2</sup>[http://www.lle.rochester.edu/omega\\_facility/omega/](http://www.lle.rochester.edu/omega_facility/omega/)

<sup>3</sup><https://computation.llnl.gov/project/blast/>

that the FEM approach has the ability to model the shock within a single mesh element. These improvements have reduced some of the numerical errors that have been exhibited by previous methods.

BLAST employs the Modular Finite Element Methods Library<sup>4</sup> (MFEM) [9], a general finite element library also being developed at LLNL, to spatially discretize using the high-order (HO) FEM on meshes with curved surfaces. To become an effective radiation hydrodynamics package, BLAST will need to integrate with a radiation transport package that is able to model the radiation field in these HEDP regimes in the same geometries and spatial discretizations as the hydrodynamics being modeled. That is, the radiation transport must be solved using the spatial discretizations that BLAST uses to solve the hydrodynamics equations. The main topic of this thesis is rooted in the spatial discretization of the radiation transport equation using HO finite elements on HO meshes.

This chapter introduces the radiation transport equation and establishes the motivation for using the HO methods. In Section 1.1, we give a brief introduction to the radiation transport equation and nomenclature. In Section 1.2, we describe various discretization methods used to solve the radiation transport equation. In Section 1.3, we describe the diffusion limit and its application to optically thick problems found in HEDP regimes. In Section 1.4, we discuss some of the research conducted for accelerating the source iteration method. In Section 1.5, we introduce the research that has been performed solving the transport equation using *R-Z* geometry. In Section 1.6, we further the *R-Z* geometry discussion by motivating a need for solving a spherically symmetry system using *R-Z* geometry. In Section 1.7, we state the research objectives for this dissertation. Finally, in Section 1.8, we outline the remainder of this dissertation.

---

<sup>4</sup>[mfem.org](http://mfem.org)

## 1.1 Radiation Transport

The steady-state, mono-energetic radiation transport equation,

$$\boldsymbol{\Omega} \cdot \nabla \psi(\mathbf{x}, \boldsymbol{\Omega}) + \sigma_t(\mathbf{x})\psi(\mathbf{x}, \boldsymbol{\Omega}) = \frac{1}{4\pi}\sigma_s(\mathbf{x}) \int_{4\pi} \psi(\mathbf{x}, \boldsymbol{\Omega}') d\Omega' + \frac{1}{4\pi}S_0(\mathbf{x}), \quad (1)$$

describes the angular flux distribution,  $\psi(\mathbf{x}, \boldsymbol{\Omega})$ , as a function of position,  $\mathbf{x}$ , and direction of travel,  $\boldsymbol{\Omega}$ . We also define the scalar flux by

$$\phi(\mathbf{x}) = \int_{4\pi} \psi(\mathbf{x}, \boldsymbol{\Omega}') d\Omega', \quad (2)$$

which accounts for the angular fluxes in all directions at spatial position  $\mathbf{x}$ . Both the angular and scalar fluxes describe a particle density in a phase space denoted by their dependent variables and have units  $\text{cm}^{-2} \text{ s}^{-1}$ . In general, the total macroscopic cross section,  $\sigma_t(\mathbf{x}) = \varsigma_t(\mathbf{x})N(\mathbf{x})$ , is a property of the microscopic total cross section,  $\varsigma_t(\mathbf{x}) \text{ cm}^2$ , and the number density of the material,  $N(\mathbf{x}) \text{ cm}^{-3}$ . The absorption and scattering cross sections are related to the total cross section by  $\sigma_t(\mathbf{x}) = \sigma_a(\mathbf{x}) + \sigma_s(\mathbf{x})$ . Additionally, the isotropic volumetric source,  $S_0(\mathbf{x})/4\pi$  is some isotropically emitting external source (e.g., fission neutrons or blackbody radiation).

There are only a few specific cases where the radiation transport equation can be solved exactly. Problems of interest typically fall outside of this subset and numerical methods must be employed to obtain approximate solutions. There are two general categories of methods used to solve this equation: stochastic and deterministic methods.

Stochastic methods take a statistical approach. In any particular source region, a single particle is emitted and tracked through its “random walk”, traversing the problem domain until it is either absorbed or escapes the domain. One can simply tally the number of particles that get absorbed into a region of interest. This method is rooted in the physics of the stochastic particle-material interactions. If

enough particles are simulated, a statistically significant conclusion can be drawn about the particle density in a region of interest. This can be very accurate but also computationally demanding because of the large number of particles required to be simulated.

Alternatively, deterministic methods solve the radiation transport equation for the scalar flux by discretizing the equation in each of the dependent variables (i.e., space and direction of travel). The discretized equation results in a linear system of equations that can be solved with linear algebra techniques. Deterministic methods are generally faster than stochastic methods but involve discretization or truncation errors. However, employing certain discretizations can reduce the impact of these errors.

## 1.2 Discretization

Physically, particles can be distributed continuously in 3-dimensional space. Numerically, it is impossible to compute a solution at a continuum of locations so we discretize the spatial domain into a small subset of discrete locations. Similarly, a particle's direction of travel can be distributed continuously so we approximate it traveling in only a few discrete directions. It is common to discretize the direction of travel into a finite number of directions by using the discrete ordinates ( $S_N$ ) method [10]. Particles with various energies may behave or interact with material differently. It is common to approximate the continuum of particle energies by grouping them into a finite number of energy groups. If a problem evolves through time, we discretize the time continuum with discrete time steps. Ideally, we would model the continuous phase space because it describes the physical behavior of neutral particles. Since we cannot numerically account for a continuum of variables, we must make these discrete approximations. In this light, we discretize each of the continuous variables

to approximate each as closely as practical. In general, this can mean refining the discretization, e.g., refining the spatial mesh or using a higher order discrete ordinates approximation. However, the cost of higher accuracy is increased computational time, which may become prohibitively expensive.

This research discretizes the energy domain into one group, thereby making the problem energy independent. We also assume the solution of the transport equation has reached steady-state, making the problem time independent. We discretize the two remaining dependent variables (space and direction of travel) where the spatial discretization is the main focus of this dissertation.

### 1.2.1 Direction of Travel Discretization

We approximate the continuum of directions in which particles can travel by assuming they only travel in discrete ordinate ( $S_N$ ) directions. Figure 1 shows an example of a set of discrete ordinates. Specifically, this octant of the  $S_6$  level-symmetric quadrature demonstrates that  $\Omega$  is discretized into discrete directions  $\Omega_m$ , which can be described as a function of  $\mu$ ,  $\eta$ , and  $\xi$ .

We utilize the discrete ordinate weights to approximate the integral in Equation 2 by

$$\phi \approx \sum_m^M w_m \psi_m, \quad (3)$$

where  $M = N(N + 2)$ . This relation is utilized in these numerical methods outlined below. The set of angular quadrature data includes the  $\mu_m$ ,  $\eta_m$ ,  $\xi_m$ , and  $w_m$  values for each discrete ordinate direction  $m$  for  $m = 1, \dots, M$ . It is possible to generate these data sets [11] but we employ pre-generated data sets from ARDRA,<sup>5</sup> a  $S_N$  radiation transport code being developed at LLNL.

---

<sup>5</sup><https://wci.llnl.gov/simulation/computer-codes>

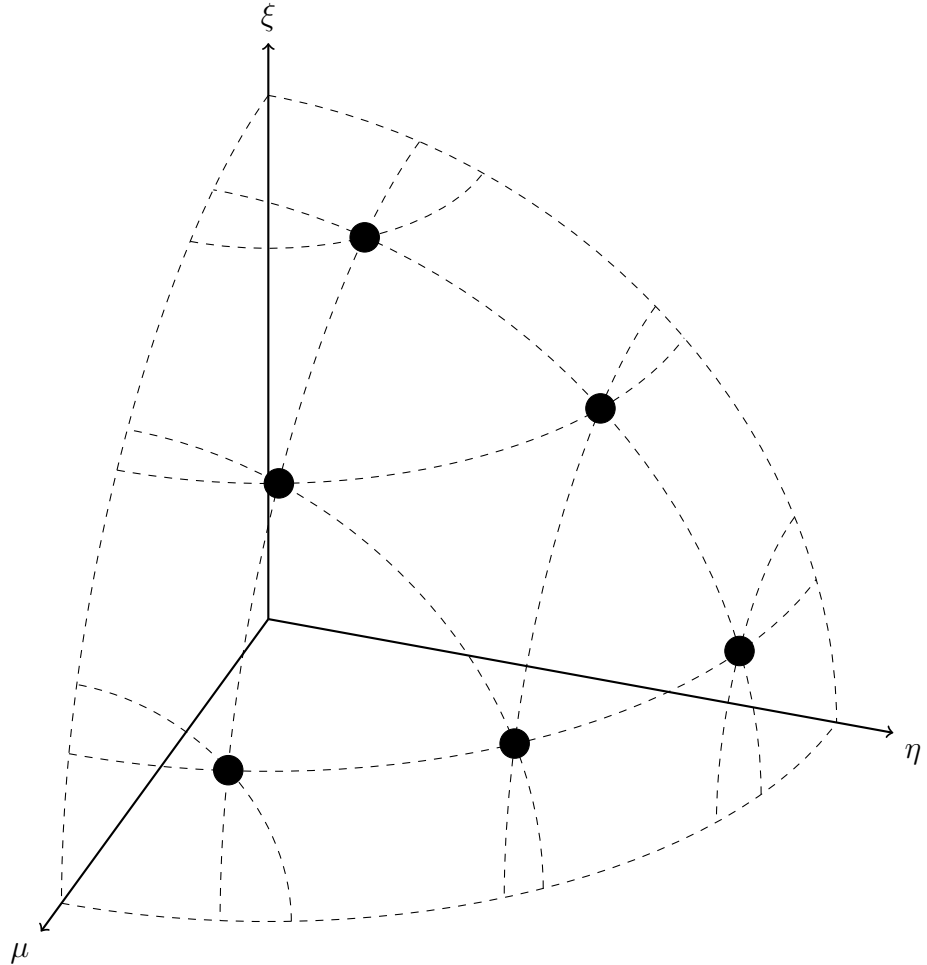


Figure 1: The positive octant for  $S_6$  level-symmetric angular quadrature.

### 1.2.2 Spatial Discretization

There are several methods of spatial discretization that appear in the transport community. Among the most common are characteristic methods [12], finite difference methods [2], finite volume methods, and finite element methods (FEM) [2]. Typically, the problem domain is divided into a larger number of smaller domains. The equations are then numerically solved on each of these smaller regions where the solution is likely to be less varying when compared to the entire problem. The FEM was introduced to the transport community in the 1970's. The utility of this method was

that it was more accurate than finite differencing methods [13]. Since then, radiation transport research using the FEM has proliferated. In particular, the discontinuous FEM (DFEM) has been favored for its accuracy in the thick diffusion limit [14] (discussed in Section 1.3). Thus, this research uses the DFEM in which the solution is approximated to have a functional form within each mesh element. More discussion of various discretization methods can be found in Lewis and Miller [2].

Additionally, these radiation transport problems are solved in each of Cartesian, cylindrical, and spherical coordinates in one-, two-, and three-dimensions. The present research is concerned with  $X$ - $Y$  and  $R$ - $Z$  geometries — two-dimensional Cartesian and cylindrical geometries, respectively. Difficulties arise in  $R$ - $Z$  geometry because of the introduction of angular derivatives. While a particle travels in a straight line in direction  $\Omega$ , the cosines of the angles relative to the coordinate axes change as the  $r$  and  $z$  coordinates change.

### 1.2.3 High Order Finite Elements

The FEM spatial discretization for the radiation transport equation has been continually investigated since the 1970s [13, 15]. Although FEMs require more computer memory than finite-difference methods, low-order (LO) methods, such as the linear discontinuous FEM (LD), have been used because of their increased accuracy [14] and continue to be used and researched [16, 17, 18]. Studying and implementing more accurate methods becomes increasingly important as computational hardware performance increases. Computers can process and communicate quicker, and larger memory can store more variables. LO FEMs have since been used and shown to be accurate in production codes like Attila [19], a three-dimensional transport code. Attila later adapted Trilinear DFEM (TLD), the three-dimensional analog to bilinear DFEM (BLD) [20]. Other methods have been studied as well, such as the piece-wise

linear DFEM (PWLD) [21].

Higher order DFEMs (polynomial orders  $p \geq 2$ ) have become more popular as modern computer performance improves. Several authors [22, 23, 24, 25] saw increased accuracy for up to 4<sup>th</sup>-order finite elements. Woods et al. [26] saw increased accuracy for up to 8<sup>th</sup>-order finite elements. These results further motivate the need for additional investigation of these HO methods.

Negative solutions can arise from oscillations within the HO FEM when the solution is near zero [27, 26]. These negative solutions are non-physical and must be corrected. Several authors have addressed negative scalar fluxes [17, 18, 28, 29, 30], with corrective methods generally falling into two categories: *ad hoc* modification after calculating a solution, and modifying the equations beforehand to yield positive results. In this dissertation, we retain the negative fluxes as results of this methodology. We leave the relevant investigation of negative flux corrections to future work.

#### 1.2.4 Meshes

There are a wide variety of meshes used with triangular and quadrilateral (and their three-dimensional equivalents) being the most common. Modeling curved boundaries with quadrilateral spatial meshes can be difficult without significant mesh refinement. Triangular meshes may be used in these cases and are often seen in literature [13, 23, 24, 31]. Additionally, unstructured meshes are popular for modeling difficult spatial geometries. For example, in three-dimensions, Attila can discretize the spatial domain using unstructured tetrahedral meshes [19].

Recently, meshes with curved surfaces have been investigated using finite elements for radiation transport. Liu and Larsen [32] used meshes with circular arcs to model a fuel pin geometry exactly. They performed their calculations using an average normal direction for the zone surface and swept through the mesh with surface averages fluxes

equal to the zone average fluxes. Schunert et al. [33] used 1<sup>st</sup>-order FEM but with 2<sup>nd</sup>-order mesh surfaces instead of circular arcs for their fuel lattice geometry. They demonstrated an increase in accuracy using the higher-order mesh without an increase in computational time. Woods [27] and Woods et al. [26] demonstrated the use of up to 8<sup>th</sup>-order meshes. Again, the motivation behind using meshes with curved surfaces is to model curved boundaries within a problem without requiring additional mesh refinement. Woods et al. [26] performed a spatial convergence study using meshes with curved surfaces and saw convergence rates of  $(p + 1)$ , which is consistent with predictions and results from Lasaint and Raviart [15] and Wang and Ragusa [23].

Other fields have investigated the use of meshes with curved surfaces. Cheng [34] demonstrated that straight-edged meshes, compared to curved meshes, restricted the accuracy of the solution of the compressible Euler equations, pointing to the necessity of curved meshes for higher-order accuracy. Dobrev et al. [7] saw increased accuracy using such meshes for Lagrangian hydrodynamics. They mapped the reference element to the physical element using the basis functions, which results in curved surfaces for HO finite elements. Subsequently, Dobrev et al. [35] demonstrated the use of curved meshes in axisymmetric geometries and noted that it modeled some features of the flow more accurately, among other improvements.

### 1.3 Diffusion Limit

In high energy density physics (HEDP) problems, a particle can have a very small mean free path (mfp) compared to the size of a spatial zone. The mfp is the inverse of the total cross section  $\Lambda = \sigma_t^{-1}$ . Therefore, when the total macroscopic cross section,  $\sigma_t$ , becomes very large, a span of length can be described as being many mfp's long. These problems are called “optically thick”. We require the transport equation (Equation 1) to resolve solutions in the optically thick regime. We can assess

the behavior of Equation 1 as the problem becomes increasingly optically thick by performing an asymptotic analysis. Specifically, a small factor  $\varepsilon$  can be used to scale the physical processes of Equation 1:

$$\boldsymbol{\Omega} \cdot \nabla \psi + \frac{\sigma_t}{\varepsilon} \psi = \frac{1}{4\pi} \left( \frac{\sigma_t}{\varepsilon} - \varepsilon \sigma_a \right) \int_{4\pi} \psi d\Omega' + \varepsilon S_0, \quad (4)$$

where arguments have been dropped for brevity. Then, as  $\varepsilon \rightarrow 0$ , the mean free path  $\Lambda = \varepsilon/\sigma_t \rightarrow 0$ . In this limit, the problem is said to be optically thick and diffusive. It can be shown [36, 37] that this scaled analytic transport equation limits to the analytic radiation diffusion equation to  $O(\varepsilon^2)$ . The diffusion equation provides accurate solutions to optically thick and diffusive problems in the problem interior. Determining that the analytic transport equation limits to the analytic diffusion equation is physically meaningful. Optically thick and diffusive problems that may be typically solved with the radiation diffusion equation may also be solved using the radiation transport equation.

The diffusion equation has substantially fewer degrees of freedom making it much quicker to solve numerically. This benefit is accompanied by some drawbacks. The diffusion equation cannot resolve optically thin problems nor solutions near highly absorbing regions, voids, nor strong material discontinuities [3]. However, the transport equation can resolve solutions in all of these regimes, including the diffusive regions. Therefore, this dissertation employs the transport equation to solve problems that are optically thick and diffusive.

The diffusion limit analysis has been applied to spatially discretized transport problems. The LD and lumped LD (LLD) methods were shown to have the diffusion limit in one-dimension by Larsen and Morel [14] and Larsen [38], respectively, which is one of the reasons for their continued popularity in literature. In multiple dimensions, the LD method generally fails in the diffusion limit [39], but the LLD [31, 40],

BLD [18], and fully lumped BLD (FLBLD) [41] methods possess the diffusion limit. Lumping the BLD equations in curvilinear geometry has been demonstrated to possess the diffusion limit as well [42, 43]. Attila has been demonstrated to solve problems in the diffusion limit using TLD, despite having the potential for negative fluxes [20].

The PWLD has also been popular for its performance in the diffusion limit. Stone and Adams [44] concluded the PWLD should behave as well as BLD but on unstructured meshes. Bailey et al. [21, 45] corroborated this and extended the PWLD method to RZ geometry and concluded this method has the diffusion limit. Bailey et al. [46] then introduced piece-wise BLD (PWBLD), which allows for more curvature in a solution and has properties favorable to having the diffusion limit, although they do not perform the asymptotic analysis to be conclusive.

Woods et al. [26] numerically demonstrate that two-dimensional Cartesian HO finite elements trend toward the diffusion limit despite not being conclusive about possessing the diffusion limit. Their study was performed without a source iteration acceleration technique so they were unable to perform calculations for optically thick media. This was performed on a quadrilateral mesh with curved surfaces. Their results indicated their method may converge toward the diffusion limit at  $O(\varepsilon)$  rather than  $O(\varepsilon^2)$ , which may have occurred due to the use of curved surfaces [18].

## 1.4 Source Iteration Acceleration

Radiation transport is integral to applications such as inertial confinement fusion and astrophysics. These problems often have materials that are optically thick (material regions are many mean-free-path lengths across) and diffusive (highly scattering) and introduce challenges to the solution methods for the transport equation. Specifically, the source iteration (SI) method [2] is commonly employed to solve the transport

equation. The algorithm

$$\Omega \cdot \nabla \psi^{(\ell+1/2)} + \sigma_t \psi^{(\ell+1/2)} = \frac{1}{4\pi} \sigma_s \phi^{(\ell)} + S_0 \quad (5a)$$

$$\phi^{(\ell+1/2)} = \sum_m w_m \psi_m^{(\ell+1/2)} \quad (5b)$$

$$\phi^{(\ell+1)} = \phi^{(\ell+1/2)} \quad (5c)$$

describes the calculation of the angular flux using the lagged scalar flux followed by an update to the scalar flux. The iteration is continued until  $\phi$  converges to within some defined tolerance. The SI algorithm can converge arbitrarily slowly in highly scattering problems [47], resulting in impractical computational times. Since computational efficiency is important, an alternative option to using the SI method on the transport equation is to solve the problem using the diffusion equation instead. The radiation diffusion equation can resolve these optically thick and diffusive media well and it does not require any source iteration. However, the diffusion equation cannot resolve solutions near highly absorbing regions, optically thin regions, nor at material discontinuities including vacuum boundaries [3]. To obtain accurate solutions in these heterogeneous regions, we must solve the transport equation.

In order to preserve the transport solution on optically thick and diffusive problems, we must reduce the SI computational time in one of two ways. We may refine the mesh until the optical thickness of a typical mesh cell is on the order of a mean-free-path to effectively solve an optically thin problem in each mesh zone. However, this option may not be computationally efficient because it might introduce a large number of degrees of freedom to the problem, thereby increasing the solution time. Alternatively, acceleration techniques may be applied to the SI to compensate for slow convergence.

Several SI acceleration schemes have been developed. The Wareing-Larsen-Adams (WLA) method [48], accelerates the source iterations but its effectiveness was found

to degrade as cells become optically thick [49]. Another alternative, the modified four-step (M4S) [50], is effective in 1-D but is only conditionally stable in 2-D for unstructured meshes. Diffusion synthetic acceleration (DSA) is a very common method. Using DSA, Larsen [47] and Larsen and McCoy [51] showed that one-dimensional LD is unconditionally accelerated. Wareing et al. [48] and Adams and Martin [52] extended unconditionally accelerating DSA to two-dimensions.

Recently, Wang and Ragusa [22] developed the modified interior penalty (MIP) form for the DSA equations. Considered a partially consistent scheme, it was developed from the interior penalty (IP) form of a discretized diffusion equation and was originally applied to HO DFEM  $S_N$  transport on triangular meshes. The IP method is not stable for optically thick media so it was combined with a spatial discretization they derived — diffusion conforming form (DCF) — that is stable in the optically thick regime. The MIP DSA equations switch between the IP and DCF methods and was demonstrated to be an effective SI acceleration scheme for HO DFEM methods. Wang and Ragusa's Fourier analysis demonstrated the effectiveness of this DSA scheme and corroborated it with numerical results. It has since been used with PWLD on arbitrary polygonal meshes [53] and later with BLD [54]. Woods et al. [1] implemented the MIP DSA equations and investigated the performance on meshes with curved surfaces; demonstrating that the method remains unconditionally stable.

The MIP DSA equations were derived with homogeneous Dirichlet boundary conditions according to Kanschat [55] for incompressible flow. It has been acknowledged that homogeneous Dirichlet boundary conditions may degrade performance [25]. Other DSA implementations utilize Robin (Marshak, zero incident current, vacuum) boundary conditions [52, 49]. This allows a nonzero DSA solution on the problem boundaries, thereby allowing a nonzero update to the transport scalar flux solution. In this dissertation, we present an extension of the work done by Woods et al. [1] that

demonstrates the rapid convergence of the MIP DSA equations utilizing the Robin boundary condition.

## 1.5 R-Z Geometry

The radiation transport equation has been solved in *R-Z* geometry for many years. One particular difficulty with cylindrical coordinates is that an angular derivative is present within the streaming term. Hence, the spatial discretization is inherently dependent upon the direction-of-travel discretization. Despite a particle traveling in a straight line, the coordinate system describing that direction changes with position. The common method of handling the spatial discretization, which includes the angular discretization (described in Section 4), is to perform an angular differencing that requires a “starting direction” equation. The system of equations is then closed by using a weighted diamond difference scheme.

Palmer and Adams [42] and Palmer [56] solved the *R-Z*  $S_N$  equations using BLD, mass lumped BLD (MLBLD), surface lumped BLD (SLBLD), FLBLD, and simple corner balance (SCB) methods but found that only the FLBLD and SCB methods are accurate in the thick diffusion limit, as predicted by their asymptotic diffusion limit analysis. They determined that the support points must be sufficiently “local” to achieve a reasonable discretization of the diffusion equation.

Bailey et al. [21] derived the PWLD transport equation for *R-Z* geometry on arbitrary polygonal meshes and showed that their method is accurate in the diffusion limit. Bailey [45] performed an asymptotic diffusion limit analysis for PWLD in *R-Z* geometry on an arbitrary polygonal mesh and found the leading order angular flux is isotropic. The PWLD scheme also displayed  $O(h^2)$  convergence rates in several test problems, as expected.

Morel et al. [31] performed an asymptotic diffusion limit analysis for the LLD

method in *R-Z* geometry on a triangular mesh. The LLD equations satisfy a lumped linear continuous (LLC) diffusion discretization to leading order on the mesh interior. They also numerically demonstrate a  $O(h^2)$  spatial convergence in the thick diffusion limit.

Efforts to maintain positivity on non-orthogonal meshes in *R-Z* geometry have been successful. Morel et al. [43] derived a lumped BLD scheme for quadrilaterals that “is conservative, preserves the constant solution, preserves the thick diffusion limit, behaves well with unresolved boundary layers, and gives second-order accuracy in both the transport and thick diffusion-limit regimes.”

At this time, only Woods and Palmer [57] have applied the HO DFEM in *R-Z* geometry on meshes with curved surfaces. That work is presented in this dissertation in support of the present research objectives.

## 1.6 Axisymmetry

As previously mentioned, radiation-hydrodynamics is the multiphysics solution to a thermal radiation problem coupled with a hydrodynamics problem. Since the hydrodynamics equations are being solved in *R-Z* geometry to preserve radial flow symmetry, the radiation transport equations must also be solved in *R-Z* geometry and preserve the same symmetry. That is, the transport equation must preserve spherical symmetry using the *R-Z* geometry spatial discretization.

Despite the convenience of describing the analytical position within a sphere using spherical coordinates, the spatial discretization becomes much more complicated. It can be more convenient to solve a spherical problem using *R-Z* geometry because there are more angular derivatives in the streaming term of the radiation transport equation in spherical coordinates than in cylindrical. The increased complexity is analogous to the increased complexity of using *R-Z* geometry from Cartesian coordinates.

There has been relatively little research in preserving spherical symmetry with the radiation transport equation in *R-Z* geometry. As previously mentioned, in hydrodynamics, Dobrev et al. [35] demonstrated this spherical symmetry preservation. In radiation diffusion, Brunner et al. [58] demonstrated conditional spherical symmetry preservation. To date, we are only aware of one published article discussing the ability of the *R-Z* transport equation to preserve 1-D spherical symmetry. Chaland and Samba [59] qualitatively demonstrated spherical symmetry preservation in a void with an initial condition of scalar flux in the center of the “sphere”. They demonstrated that ray-effects are created from the  $S_N$  transport equations, whereas their alternative angular discretization qualitatively preserves the 1-D spherical symmetry in a void. We follow the direction of Brunner et al. [58] by determining the spherical symmetry preservation by using the method of manufactured solutions (MMS) [60] with a manufactured solution in spherical geometry.

## 1.7 Research Objectives

The research objectives of this dissertation are to:

- derive, implement, and characterize the modified interior penalty (MIP) diffusion synthetic acceleration (DSA) method using Robin boundary conditions, and
- derive, implement, and characterize the transport equation in *R-Z* geometry using HO DFEM on meshes with curved surfaces.

## 1.8 Outline

The remainder of this dissertation is organized as follows. In Section 2, we discuss the HO DFEM, meshes with curved surfaces, and the solution methods. In Section 3, we

discuss the DSA method, the MIP DSA method for both homogeneous Dirichlet and Robin boundary conditions, and results we obtained. Finally, Section 4 discusses the  $R$ - $Z$  discretization scheme, solution methodology, and results demonstrating accuracy and spherical symmetry preservation.

## 2 Methods

In this section we describe the high-order (HO) basis functions that we employ in this research (Section 2.1), the HO mesh transformation required (Section 2.2), and the solution method that we employ to solve the system of equations (Section 2.3).

### 2.1 High Order DFEM

The basis functions are spatially dependent. Therefore, they are unique to each physical mesh zone due to the shape and location of each zone. We avoid having to perform calculations with arbitrarily large set of basis functions by transforming each physical element into the reference element. The basis functions on the reference element are identical regardless of the physical element shape and position. In general, the basis functions are allowed to be unique to each element, but we use the same set of basis functions across all elements for simplicity.

One requirement for the basis functions is that they are unity at the integration point they “live” on and zero at all of the others. In two-dimensions, the general form of the first-order polynomial basis function is

$$b(x, y) = axy + bx + cy + d, \quad (6)$$

and the second-order basis function,

$$b(x, y) = ax^2y^2 + bx^2y + cx^2 + dxy^2 + exy + fx + gy^2 + hy + j, \quad (7)$$

where the sets  $\{a, b, c, d\}$  and  $\{a, b, c, d, e, f, g, h, j\}$  are the sets of coefficients that define the unique basis function for each integration point, respectively. The location of the integration points is important. For example, we may place these evenly across the reference element or at Gaussian quadrature locations. On the unit square  $[0, 1] \times [0, 1]$ , the Gaussian integration points are located at the cross product of the

nodes on  $[0, 1]$ . Listed for linear, quadratic, and cubic finite elements in Table 1, the Gaussian integration point locations were transformed from the traditional  $[-1, 1]$  to the reference element length  $[0, 1]$ .

Table 1: Gaussian quadrature locations.

FE order	Points on $[-1, 1]$	Points on $[0, 1]$
1	$\pm \frac{1}{\sqrt{3}}$	$\frac{1}{3 + \sqrt{3}}$ $1 - \frac{1}{3 + \sqrt{3}}$
2	0 $\pm \sqrt{\frac{3}{5}}$	$\frac{1}{5 + \sqrt{15}}$ 0.5 $1 - \frac{1}{5 + \sqrt{15}}$
3	$\pm \sqrt{\frac{3}{7} - \frac{2}{7}\sqrt{\frac{6}{5}}}$ $\pm \sqrt{\frac{3}{7} + \frac{2}{7}\sqrt{\frac{6}{5}}}$	$\frac{10 + \sqrt{30}}{35 + \sqrt{35(15 - 2\sqrt{30})}}$ $\frac{10 - \sqrt{30}}{35 + \sqrt{35(15 - 2\sqrt{30})}}$ $1 - \frac{10 + \sqrt{30}}{35 + \sqrt{35(15 - 2\sqrt{30})}}$ $1 - \frac{10 - \sqrt{30}}{35 + \sqrt{35(15 - 2\sqrt{30})}}$

Once the finite element order and the set of integration points is determined, the linear system can be arranged to determine the coefficients. For example, to determine the first-order basis function that “lives” at integration point  $(x_1, y_1)$  (and is equal to unity at that integration point and is zero at the remaining three), we

assemble the system of equations

$$\begin{bmatrix} x_1y_1 & x_1 & y_1 & 1 \\ x_2y_2 & x_2 & y_2 & 1 \\ x_3y_3 & x_3 & y_3 & 1 \\ x_4y_4 & x_4 & y_4 & 1 \end{bmatrix} \begin{bmatrix} a \\ b \\ c \\ d \end{bmatrix} = \begin{bmatrix} 1 \\ 0 \\ 0 \\ 0 \end{bmatrix}. \quad (8)$$

The 1 inside the solution vector on the right-hand-side determines which basis function coefficients will be obtained. For example, the right-hand-side vector  $[0, 0, 1, 0]^T$  will return the basis function coefficients for the third integration point at  $(x_3, y_3)$ .

## 2.2 Meshes with Curved Surfaces

The complicated shapes of each mesh zone create a challenge by having to solve the discretized equations for each unique mesh zone. We avoid having to solve a unique set of equations for each mesh zone by transforming the mesh zone into the reference element. Each mesh zone will have a unique transformation but an identical set of basis functions to obtain the solution on the reference element.

We set up the system of equations (Section 2.1) on each individual mesh zone after we transform it to the reference element. After performing the following integrations, we map the solution back to the physical element. The bi-quadratic mapping from the reference element to the physical element, shown in Figure 2, has the following functional form

$$\begin{bmatrix} x(\rho, \kappa) \\ y(\rho, \kappa) \end{bmatrix} = \sum_{i=1}^{J_k} \sum_{j=1}^{J_k} \begin{bmatrix} x_{ij} \\ y_{ij} \end{bmatrix} N_i(\rho)N_j(\kappa) \quad (9)$$

where

$$N_l(\xi) = \begin{cases} (2\xi - 1)(\xi - 1), & l = 1 \\ 4\xi(1 - \xi), & l = 2 \\ \xi(2\xi - 1), & l = 3 \end{cases} \quad (10)$$

are the quadratic basis functions that have support points at typical locations shown in the left image of Figure 2. The  $(x_{ij}, y_{ij})$  coordinates are the locations of the support points in the physical element and are generally known. For example, the node  $(x_{12}, y_{12})$  is the location on the physical zone that is mapped from  $(\rho, \kappa) = (0, 0.5)$  on the reference element.

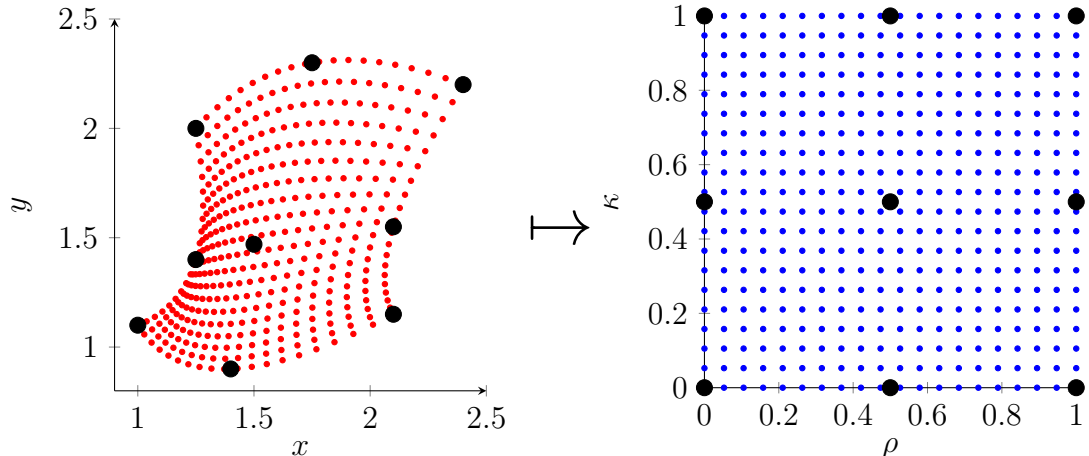


Figure 2: Example of mapping the reference element to a physical element.

The determinant of the Jacobian of the transformation,

$$\det(J) = \begin{vmatrix} \frac{\partial x}{\partial \rho} & \frac{\partial y}{\partial \rho} \\ \frac{\partial x}{\partial \kappa} & \frac{\partial y}{\partial \kappa} \end{vmatrix}, \quad (11)$$

is used to perform the mapping from the physical space to  $\rho$ - $\kappa$  space.

## 2.3 Solution Method

We employ the Modular Finite Elements Library (MFEM)<sup>6</sup> to perform integrations to assemble the system of equations for each element. These elements are then assembled into a global matrix that acts on each spatial degree of freedom simultaneously.

The meshes described in Section 2.2 add complications to the numerical methods used to solve the transport equation. In particular, cycles can be present during the spatial sweep of the mesh [61, 62]. It is common to solve for a single mesh zone using incident angular flux information and propagate that angular flux from mesh zone to mesh zone, sweeping through the grid. However, if any particular mesh zone has both incident and outgoing angular fluxes to another mesh zone, they depend upon each other in a cyclic manner. “Breaking the cycle” in some fashion is necessary to perform the numerical computation. Instead of sweeping through the grid, we utilize MFEM to generate the solution matrix for all of the mesh zones for the entire problem. This is computationally intensive, but it bypasses the need to consider any cycles that may occur.

After generating the system of equations, we use UMFPack, a direct solver that performs a LU decomposition [63, 64] to solve for all of the spatial degrees of freedom for direction  $\Omega_m$ . We solve the global system of equations for the scalar flux,  $\phi$ , using source iteration (Equation 5) with convergence criterion

$$\|\phi^{(\ell)} - \phi^{(\ell-1)}\|_{\infty} < \varepsilon_{\text{conv}}(1 - \rho) \|\phi^{(\ell)}\|_{\infty}, \quad (12)$$

where  $\varepsilon_{\text{conv}}$  is some small tolerance and  $\rho$  is the estimated spectral radius,

$$\rho \approx \frac{\|\phi^{(\ell)} - \phi^{(\ell-1)}\|}{\|\phi^{(\ell-1)} - \phi^{(\ell-2)}\|}. \quad (13)$$

---

<sup>6</sup>[mfem.org](http://mfem.org)

### 3 Diffusion Synthetic Acceleration

Materials in inertial confinement fusion and astrophysics applications can be exceptionally optically thick and diffusive. A transport solver should be capable of performing accurate and efficient calculations on such problems. We present here an extension of Woods et al. [26] that demonstrates a rapidly-convergent iterative solver for the transport equation spatially discretized with the high-order (HO) discontinuous finite element method (DFEM).

For these optically thick and diffusive media, the SI method (Equations 5) can converge arbitrarily slowly resulting in impractical computational times. The diffusion equation can resolve solutions for these problems but is only accurate far from highly absorbing regions, material discontinuities, and void regions, including problem boundaries. The transport equation can resolve a solution in all of these regions. So, in order to achieve a transport quality solution, we must accelerate the source iteration scheme.

Several acceleration schemes are presented in Section 1.4. Here, we discuss the modified interior penalty (MIP) diffusion synthetic acceleration (DSA) equations introduced by Wang and Ragusa [22]. It is necessary that an acceleration scheme is effective using HO DFEM. The partially consistent MIP DSA equations stem from the symmetric interior penalty (IP) derivation of the diffusion equation. The IP method is not stable for optically thick mesh zones so it was combined with the diffusion conforming form (DCF), a spatially discretized diffusion equation derived from the spatially discretized  $S_N$  equations that is not stable for intermediate or low optical thicknesses. The MIP equations adapt a “switch” between the IP method for optically thin regions and the DCF method for optically thick regions. Wang and Ragusa’s Fourier analysis demonstrated the effectiveness of this DSA scheme and was

corroborated by their numerical results. Previous work implemented this method, further corroborating the literature, and additionally demonstrated similar behavior on meshes with curved surfaces [1].

Although Wang and Ragusa proposed true vacuum boundary conditions for the MIP DSA equation, their finite element discretization implemented homogeneous Dirichlet boundary conditions on the problem boundaries. The zero incident current is the true vacuum boundary condition for the diffusion equation [52]. It differs from the homogeneous Dirichlet boundary condition in that it allows the DSA solution to be nonzero on the boundary, thereby allowing a nonzero correction to the scalar flux. The present work derives and implements homogeneous Robin boundary conditions on the problem boundaries. We present the initial results demonstrating the behavior of the spectral radii for the newly implemented boundary condition.

We consider the effects of several parameters to the spectral radius, which is the measure of the convergence rate during the source iteration. Previous literature has reported on some of the sensitivities that impact the spectral radius of DSA schemes: aspect ratios [52, 53], angular quadrature [52, 53], polynomial order [1, 22], and scattering ratios [1, 22, 48]. Presently, we focus on the sensitivity of the spectral radius to the finite element order and the constant  $C$  that arises in the stabilization parameter, for varying cell thicknesses.

The general DSA algorithm is

$$\boldsymbol{\Omega} \cdot \nabla \psi_m^{(\ell+1/2)} + \sigma_t \psi_m^{(\ell+1/2)} = \frac{1}{4\pi} (\sigma_s \phi^{(\ell)} + S_0) \quad (5a)$$

$$\phi^{(\ell+1/2)} = \sum_m w_m \psi_m^{(\ell+1/2)} \quad (5b)$$

$$-\nabla \cdot D \nabla \varphi^{(\ell+1/2)} + \sigma_a \varphi^{(\ell+1/2)} = \sigma_s (\phi^{(\ell+1/2)} - \phi^{(\ell)}) \quad (14a)$$

$$\phi^{(\ell+1)} = \phi^{(\ell+1/2)} + \varphi^{(\ell+1/2)} \quad (14b)$$

where  $\phi^{(\ell+1/2)}$  is the radiation transport scalar flux solution at iteration  $(\ell+1/2)$  prior to the DSA solve. Specifically, we solve for Equation 5a for each of the angular fluxes,  $\psi_m^{(\ell+1/2)}$  at a half-step. Then, we perform a weighted summation of the angular fluxes to obtain the scalar flux at the half step,  $\phi^{(\ell+1/2)}$ . For comparison, the unaccelerated source iteration method can then be written  $\phi^{(\ell+1)} = \phi^{(\ell+1/2)}$ . The DSA method then solves the DSA equation (Equation 14a), a diffusion equation with a modified source. Finally, the summation of the solution to the DSA equation and the scalar flux at the half step becomes the scalar flux solution at the end of the iteration. This iterative process continues until the convergence criteria

$$\|\phi^{(\ell+1)} - \phi^{(\ell)}\|_{\infty} < \varepsilon_{\text{conv}} (1 - \rho) \|\phi^{\ell+1}\|_{\infty}, \quad (15)$$

is met, where  $\varepsilon_{\text{conv}}$  is a small number. The solution to Equation 14a is the context of this section.

The remainder of this section is organized as follows. In Section 3.1, we introduce and discuss the MIP DSA equations and perform a sensitivity study on the spectral radius. In Section 3.2, we derive and integrate the Robin boundary condition into the MIP DSA equations where we also perform sensitivity studies using the Robin boundary condition implementation. Finally, we make concluding remarks in Section 3.3.

### 3.1 Modified Interior Penalty DSA

The discretization of the DSA equation (Eq. 14a) is of particular importance. A new spatial discretization method was introduced by Wang and Ragusa [22] called the modified interior penalty (MIP) diffusion synthetic acceleration (DSA) method. They demonstrated it's effectiveness using high-order finite elements (up to 4<sup>th</sup>-order),

hence the applicability in the present context.

The bilinear form of the MIP DSA equations is

$$\begin{aligned} b_{\text{MIP,D}}(\varphi, v) = & (\sigma_a \varphi, v)_{\mathcal{D}} + (D \nabla \varphi, \nabla v)_{\mathcal{D}} \\ & + (\kappa_e [\![\varphi]\!], [v])_{\partial \mathcal{D}^i} + ([\![\varphi]\!], \{D \partial_n v\})_{\partial \mathcal{D}^i} + (\{D \partial_n \varphi\}, [v])_{\partial \mathcal{D}^i} \\ & + (\kappa_e \varphi, v)_{\partial \mathcal{D}^d} - \frac{1}{2} (\varphi, D \partial_n v)_{\partial \mathcal{D}^d} - \frac{1}{2} (D \partial_n \varphi, v)_{\partial \mathcal{D}^d}, \end{aligned} \quad (16a)$$

and the linear form is

$$l_{\text{MIP}}(v) = (Q_0, v)_{\mathcal{D}} \quad (16b)$$

where

$$[\![\varphi]\!] = \varphi^+ - \varphi^-, \quad (17)$$

$$\{\{\varphi\}\} = (\varphi^+ + \varphi^-)/2, \quad (18)$$

$$Q_0 = \sigma_s (\phi^{(l+1/2)} - \phi^{(l)}), \quad (19)$$

and the inner product notation

$$(\varphi, v)_{\mathcal{D}} = \int_{\mathcal{D}} \varphi v \, d\mathbf{x}. \quad (20)$$

is used. The discretization of the diffusion term in the DSA equation requires an integration by parts. The resultant surface term is then divided into mesh interior surfaces denoted by  $\partial \mathcal{D}^i$  and problem domain surfaces,  $\partial \mathcal{D}^d$ . The second and third lines of Equation 16a are the mesh interior and problem domain surface terms, respectively. These are weakly enforced homogeneous Dirichlet conditions, as denoted by  $b_{\text{MIP,D}}$ .

The penalty term in the bilinear form (Eq. 16a) is

$$\kappa_e = \max \left( \kappa_e^{\text{IP}}, \frac{1}{4} \right), \quad (21)$$

where the IP stabilization parameter is

$$\kappa_e^{IP} = \begin{cases} \frac{c(p^+)}{2} \frac{D^+}{h_\perp^+} + \frac{c(p^-)}{2} \frac{D^-}{h_\perp^-}, & \text{on interior surfaces, i.e., } \partial\mathcal{D}_i \\ c(p) \frac{D}{h_\perp}, & \text{on boundary surfaces, i.e., } \partial\mathcal{D}_d \end{cases}, \quad (22)$$

where

$$c(p) = Cp(p+1). \quad (23)$$

The value  $h_\perp^\pm$  is the perpendicular cell size on either side of the cell surface,  $p$  is the finite element order,  $C$  is an arbitrary constant that is investigated in this research. Equation 21 contains a “switch” between the IP and DCF penalty coefficients,  $\kappa_e^{IP}$  and  $1/4$ , respectively. Equations 22 and 23 determine when the switch occurs and are largely dependent upon problem constraints.

### 3.1.1 Spectral Radius Sensitivity to Constant $C$

Previous researchers used values for  $C$  arbitrarily. Wang and Ragusa [22] used  $C = 2$  and Turcksin and Ragusa [53] used  $C = 4$ . Here, we perform a study to assess the sensitivity of the spectral radius to changes in the constant  $C$  (see Eq. 23) for various cell thicknesses, and finite element orders.

These test problems are the same as the ones used by Wang and Ragusa [22] for comparison. They are homogeneous with vacuum boundaries, have a scattering ratio  $c = 0.9999$ , and an isotropic volumetric source  $S_0 = 1 \text{ cm}^{-3} \text{ s}^{-1}$ . The mesh is a 10 cm by 10 cm quadrilateral grid uniformly divided into 100 zones, and we use  $S_8$  level symmetric angular quadrature. The total opacity  $\sigma_t$  is chosen at run-time for the appropriate optical thickness. For cell thicknesses less than 1 mfp,  $\sigma_t$  is set to  $1 \text{ cm}^{-1}$  and the mesh is incrementally refined to make each zone less optically thick.

Figure 3 shows the spectral radius of various finite element orders on an orthogonal mesh for  $C = 2$ . We observe peaks approaching  $\rho = 0.9$ , where the method performs

the “switch”. The IP method works well in the optically thin region (smaller cell sizes) and the DCF method works well in the intermediate and optically thick regions (larger cell sizes). This result is similar to numerical results of Wang and Ragusa [22]. There is little sensitivity of finite element order in the very optically thin and optically thick regions. However, the intermediate optical thickness range has a strong dependence on the choice of the finite element order. In this range, the spectral radius is generally smaller for lower finite element orders.

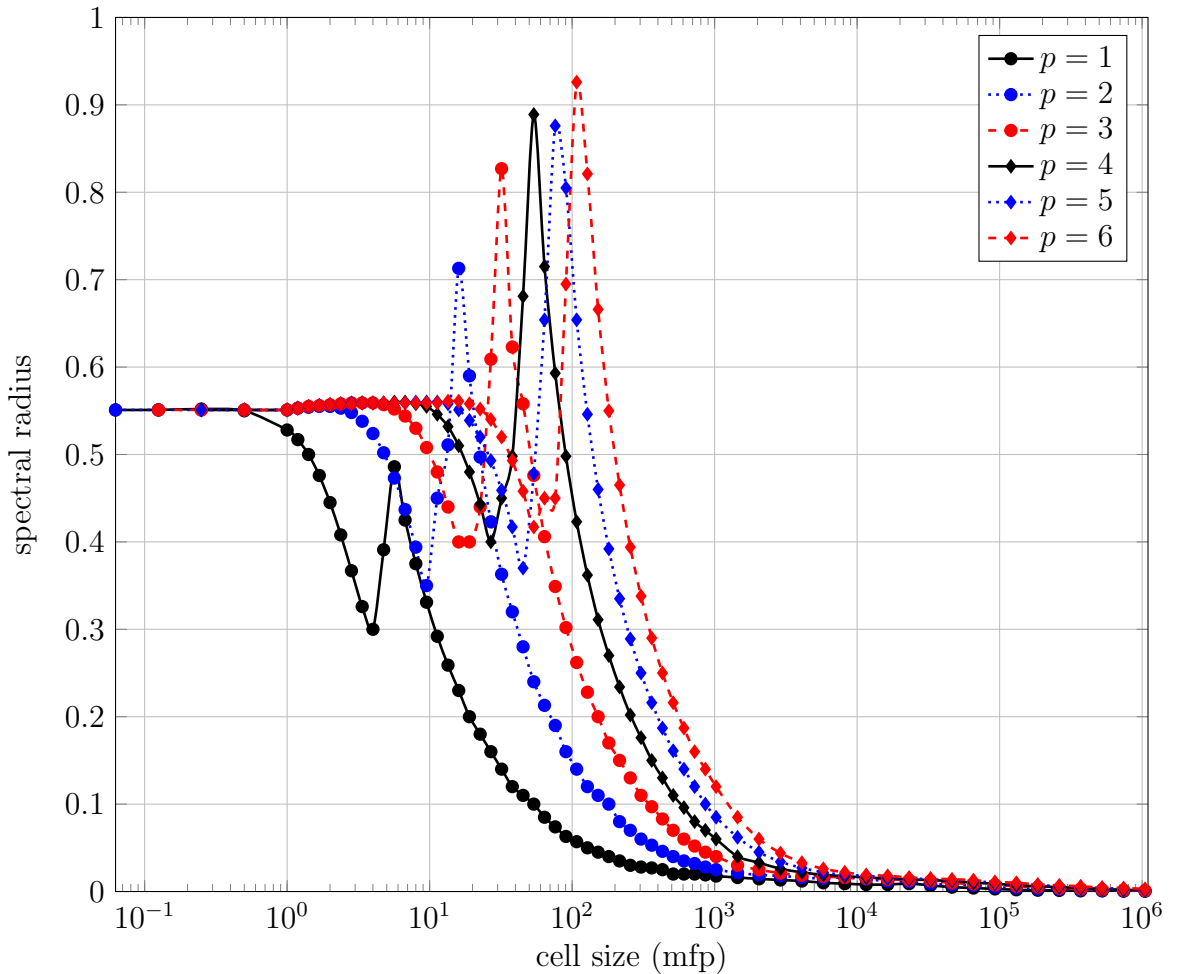


Figure 3: Spectral radius data for varying  $p$  with  $C = 2$  on an orthogonal mesh with homogeneous Dirichlet boundary conditions in the DSA solve; plot reproduced from Woods et al. [1].

Figure 4 shows the spectral radius of various finite element orders on an orthogonal mesh for  $C = 4$ . We observe that the peaks from Figure 3 are significantly diminished. The value of  $C$  moved the “switch” toward the optically thick region, thereby not forcing the DCF method to operate in the optically thin regime. The larger value of  $C$  also impacts the IP method spectral radius, resulting in a slight rise (of nearly 0.1 for higher finite element orders) before the switch to the DCF method. Again, there is little sensitivity of finite element order in the very optically thin and optically thick regions. Still, the intermediate optical thickness range has a strong dependence on the choice of the finite element order. In this range, the spectral radius is generally smaller for lower finite element orders.

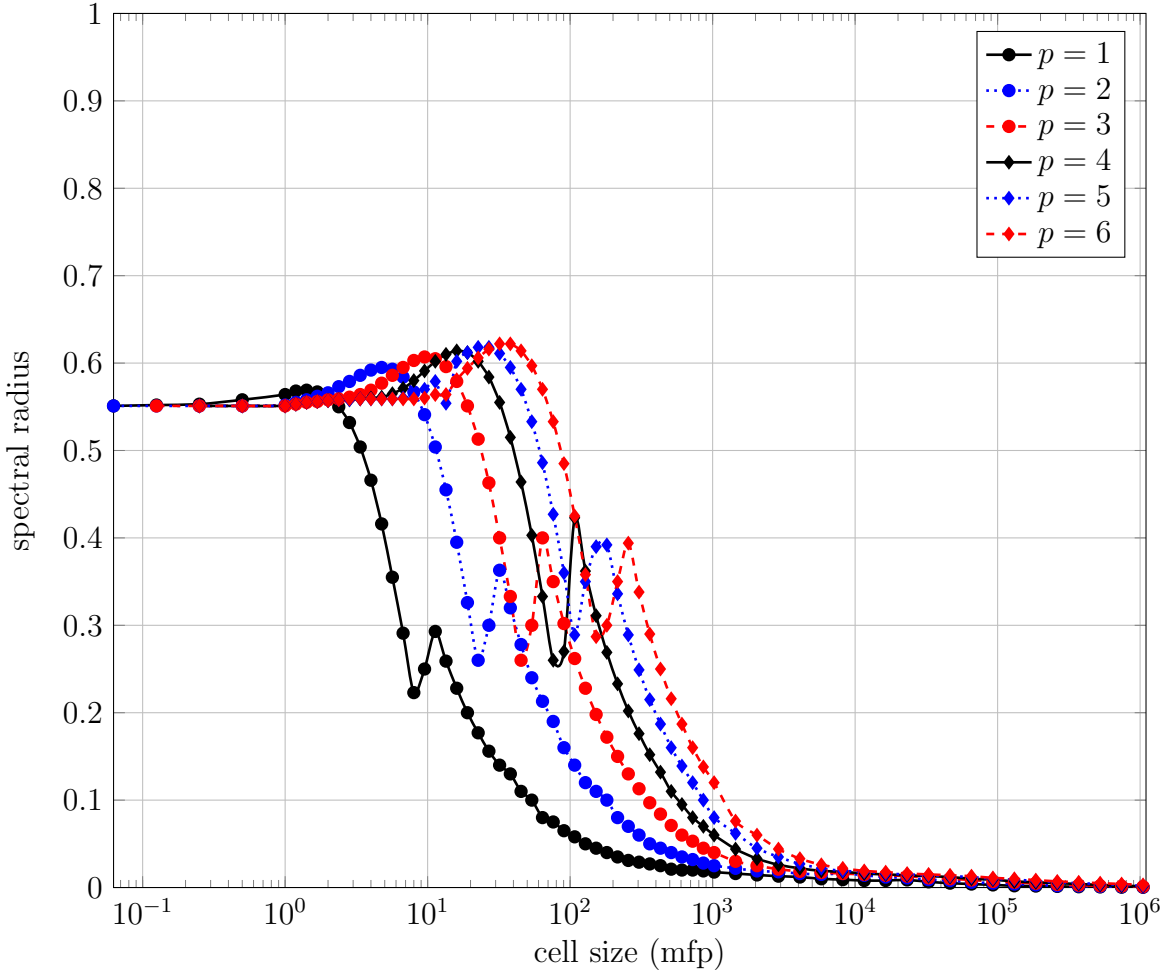


Figure 4: Spectral radius data for varying  $p$  with  $C = 4$  on an orthogonal mesh with homogeneous Dirichlet boundary conditions in the DSA solve; plot reproduced from Woods et al. [1].

Figure 5 shows the spectral radius of various finite element orders on an orthogonal mesh for  $C = 6$ . We observe that the peaks from Figure 3 remain significantly diminished like with  $C = 4$ . The value of  $C$  moved the “switch” further toward the optically thick region, thereby requiring the DCF method to operate even less in the optically thin regime. The larger value of  $C$  impacts the IP method spectral radius again, resulting in a slight rise of over 0.1 (for higher finite element orders) before the switch to the DCF method. Again, there is little sensitivity of finite element order

in the very optically thin and optically thick regions. Still, the intermediate optical thickness range has a strong dependence on the choice of the finite element order. In this range, the spectral radius is generally smaller for lower finite element orders.

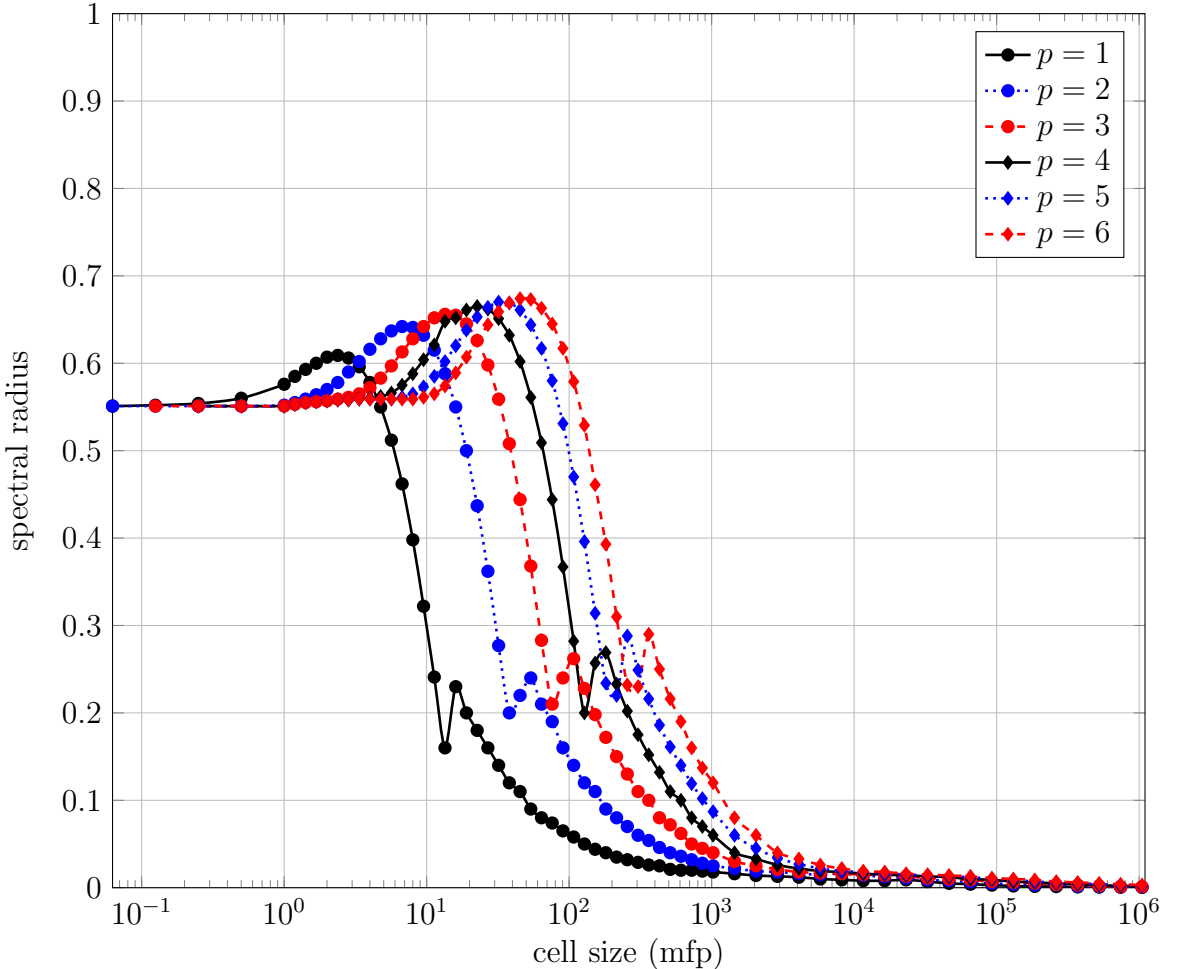


Figure 5: Spectral radius data for varying  $p$  with  $C = 6$  on an orthogonal mesh with homogeneous Dirichlet boundary conditions in the DSA solve; plot reproduced from Woods et al. [1].

In all cases  $C = \{2, 4, 6\}$ , the spectral radius was less than one, indicating these methods are unconditionally converging. We observed that larger values of  $C$  reduce the spectral radius in the intermediate range by mitigating the observable peaks.

However, the larger  $C$  values increased the spectral radius toward the optically thin region by introducing a “hump”. Assuming that the optical thickness, diffusion coefficient  $D^\pm$ , the mesh size  $h^\pm$ , and finite element order  $p^\pm$  are all problem dependent, only the value of  $C$  remains user defined. Knowing the problem specifications *a priori* may inform a particular choice of  $C$ .

### 3.1.2 Sensitivity of the Spectral Radius to the Scattering Ratio $c$

The problems here have the same cross sections and source as above but 1 cm by 1 cm grid uniformly divided into 100 zones. [An orthogonal grid would have 0.1 cm by 0.1 cm zoning.] Figure 6 shows the spectral radii for varying the scattering ratios using 4<sup>th</sup>-order finite elements and  $C = 4$  on an orthogonal mesh. Figure 7 shows the same results on a 3<sup>rd</sup>-order mesh. Increasing the scattering ratio increased the spectral radius, approaching an apparent limit. Adding curvature to the mesh surfaces also increased the spectral radius. Although the spectral radius is higher, the jump when the “switch” occurs is not as significant on the 3<sup>rd</sup>-order mesh as it is with the orthogonal grid.

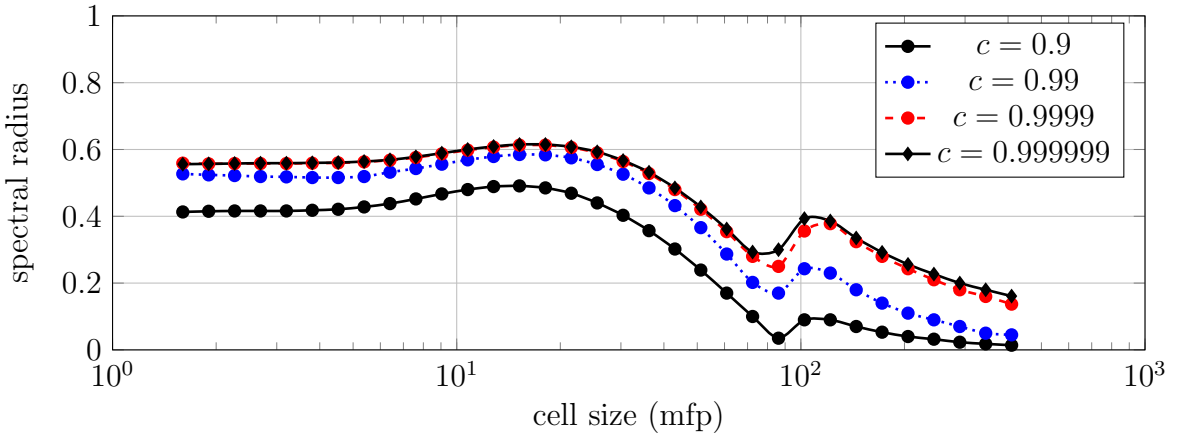


Figure 6: Spectral radius data for various scattering ratios  $c$  using 4<sup>th</sup>-order finite elements, constant  $C = 4$ , and orthogonal mesh.

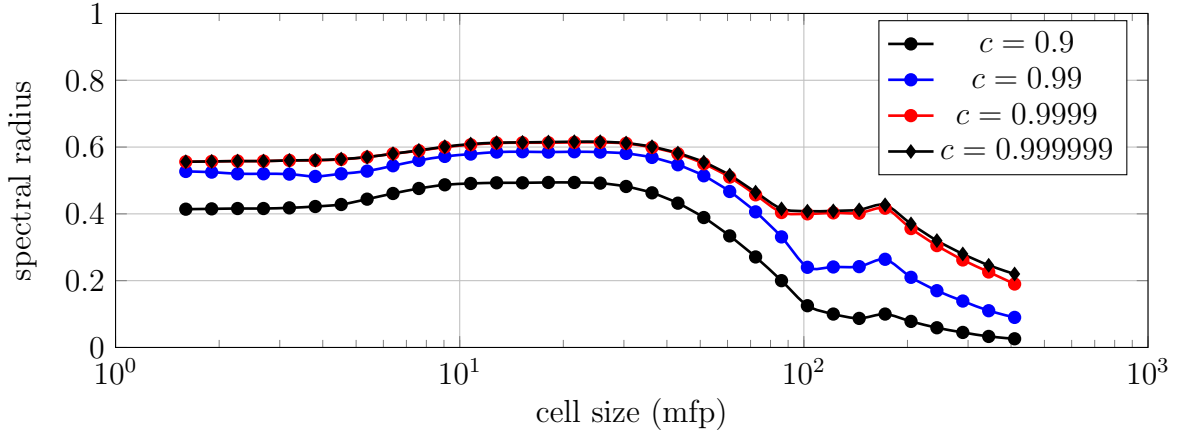


Figure 7: Spectral radius data for various scattering ratios  $c$  using 4<sup>th</sup>-order finite elements, constant  $C = 4$ , and 3<sup>rd</sup>-order mesh.

### 3.1.3 Infinite Medium MIP DSA Results

It is possible that the previous finite domain problems did not excite all of the error modes. Here, we test a uniform grid with periodic boundaries on all four sides of the problem. We performed some of the same calculations as in the previous subsection. Figures 8 - 10 show the results.

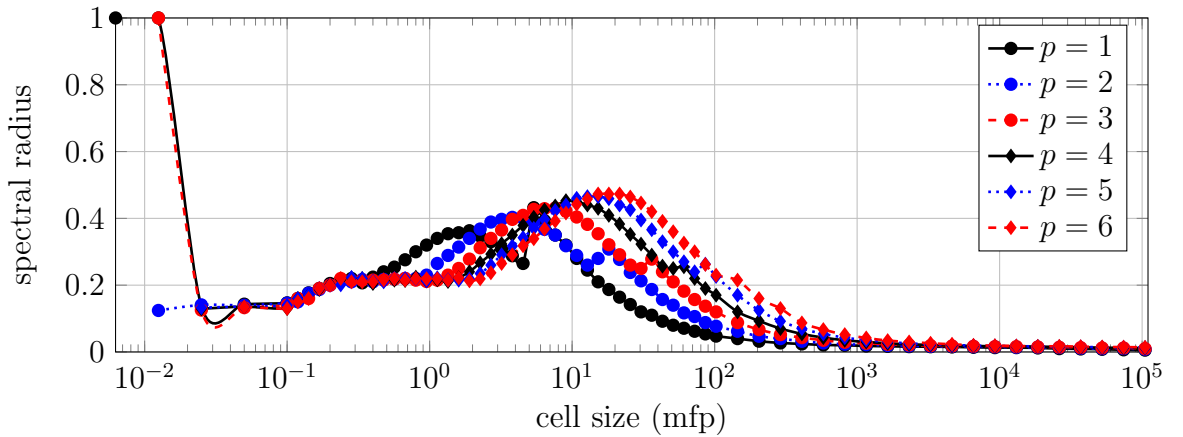


Figure 8: Spectral radius data for varying  $p$  with  $C = 2$  on a periodic orthogonal mesh.

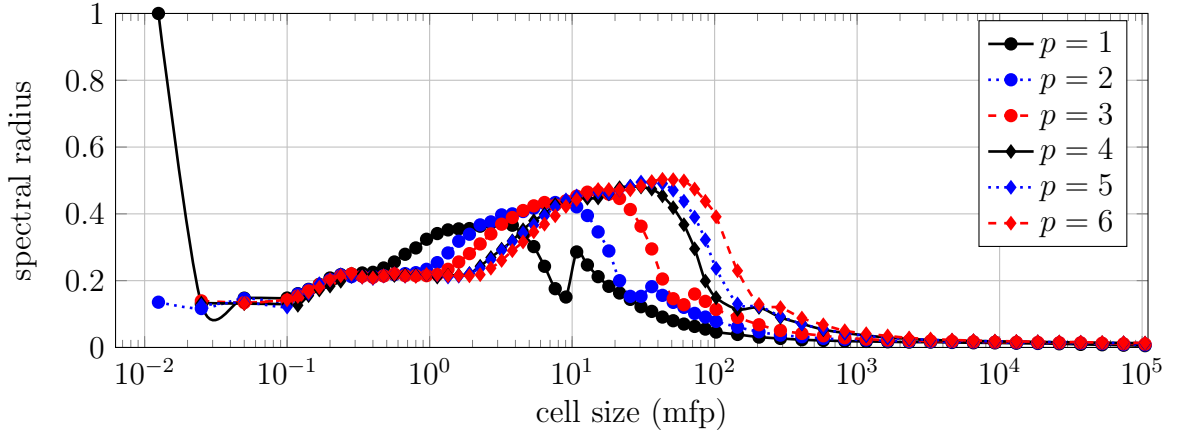


Figure 9: Spectral radius data for varying  $p$  with  $C = 4$  on a periodic orthogonal mesh.

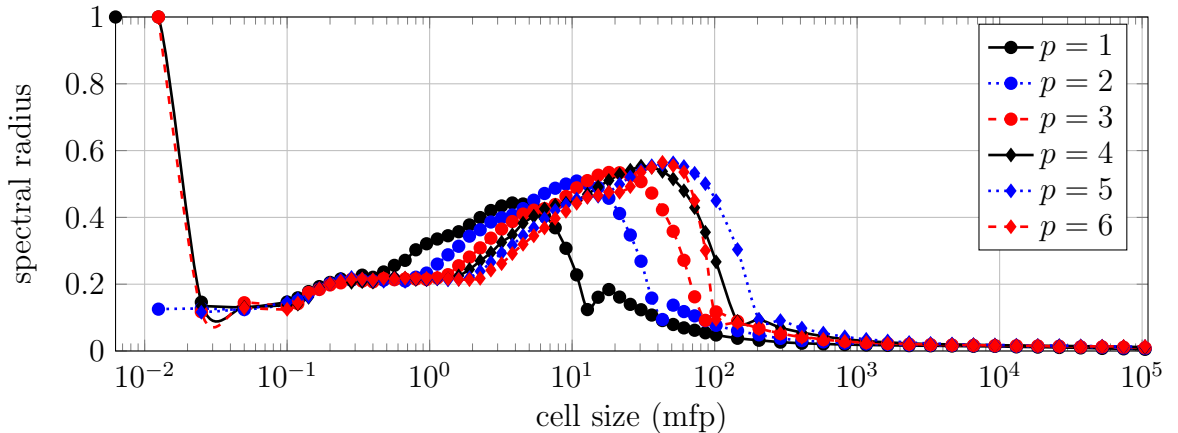


Figure 10: Spectral radius data for varying  $p$  with  $C = 6$  on a periodic orthogonal mesh.

We see the spectral radii in all plots has similar behavior as in the finite domain plots. However, the magnitudes are lower in general and the peaks are almost nonexistent at the “switch”. Notably,  $p = 1$  has the largest peak. The Fourier analysis performed by Wang and Ragusa [22] spans  $10^{-3}$  to  $10^3$  mfps with smooth behavior at either of the ends. Numerically, we observe the smooth behavior for thicker cells but

the optically thin cells do not behave as well. In some instances, the spectral radius is erratic and does not converge. These erratic spectral radii are given the value of 1 in Figures 8 - 10. Without DSA, these thin problems converge very quickly. The observed instability occurs outside the range of the results published by Wang and Ragusa. At this time, we are uncertain whether these results are real or an artifact of numerical precision, but we plan to investigate in the future.

### 3.2 MIP DSA with Robin Boundary Conditions

Kanschat [55] shows that Equation 16a employ Nitsche's method for "a fully conforming method of treating Dirichlet boundary values." The boundary terms ( $\partial\mathcal{D}^d$ ) in this form are homogeneous Dirichlet boundary conditions. The DSA correction for the scalar flux at the problem boundaries is fixed to zero, so the scalar flux is only updated by the transport solution. That is, the DSA correction only accelerates the interior solution. Consequently, the scalar fluxes on the problem boundary are only subjected to the transport equation solution source iterations.

Instead, a DSA update equation should incorporate Robin boundary conditions (zero incident partial current) on the boundaries,

$$\mathbf{J}_- = 0 = \frac{1}{4}\phi + \frac{1}{2}D\boldsymbol{\nabla}\phi \cdot \hat{n}, \quad (24)$$

$$-\frac{1}{2}\phi = D\boldsymbol{\nabla}\phi \cdot \hat{n}, \quad (25)$$

thereby allowing a correction of the boundary scalar fluxes. This boundary condition requires modification of Equation 16a. We begin by integrating the diffusion term by parts and separating the surface term into the mesh interior and problem domain boundaries:

$$-(\boldsymbol{\nabla} \cdot D\boldsymbol{\nabla}\varphi, v)_\mathcal{D} = (D\boldsymbol{\nabla}\varphi, \boldsymbol{\nabla}v)_\mathcal{D} - (D\boldsymbol{\nabla}\varphi \cdot \hat{n}, v)_{\partial\mathcal{D}^i} - (D\boldsymbol{\nabla}\varphi \cdot \hat{n}, v)_{\partial\mathcal{D}^d}. \quad (26)$$

We substitute the analytic vacuum boundary condition,

$$0 = \frac{1}{4}\varphi + \frac{1}{2}D\partial_n\varphi, \quad (27)$$

into the problem boundary term,

$$-(D\nabla\varphi \cdot \hat{n}, v)_{\partial\mathcal{D}^d} = \frac{1}{2}(\varphi, v)_{\partial\mathcal{D}^d}. \quad (28)$$

The vacuum boundary condition MIP DSA equation becomes,

$$\begin{aligned} b_{MIP,V}(\varphi, v) &= (\sigma_a \varphi, v)_{\mathcal{D}} + (D\nabla\varphi, \nabla v)_{\mathcal{D}} \\ &+ (\kappa_e [\![\varphi]\!], [\![v]\!])_{\partial\mathcal{D}^i} + ([\![\varphi]\!], \{\{D\partial_nv\}\})_{\partial\mathcal{D}^i} + (\{\{D\partial_nv\}\}, [\![v]\!])_{\partial\mathcal{D}^i} \\ &+ \frac{1}{2}(\varphi, v)_{\partial\mathcal{D}^d}, \end{aligned} \quad (29)$$

and the linear form remains Equation 16b. The only difference between Equations 16a and 29 are the problem boundary terms.

### 3.2.1 Accuracy

An analytic one-dimensional diffusion equation solution with zero incident current boundary conditions was used to benchmark the solution to the diffusion equation using the proposed Robin boundary condition methods. The original MIP DSA method (Equation 16a) was also solved for comparison. The analytic solution to the 1-D diffusion equation with homogeneous Robin boundary conditions is

$$\phi(x) = c_1 e^{x/L} + c_2 e^{-x/L} + \frac{S_0}{\sigma_a}, \quad (30a)$$

$$\begin{aligned} c_1 &= \frac{1}{4} \frac{S_0}{\sigma_a} \left[ \left( \frac{1}{4} + \frac{1}{2} \frac{D}{L} \right) e^{1/L} - \left( \frac{1}{4} - \frac{1}{2} \frac{D}{L} \right) \right] \\ &\quad \cdot \left[ \left( \frac{1}{4} - \frac{1}{2} \frac{D}{L} \right)^2 - \left( \frac{1}{4} + \frac{1}{2} \frac{D}{L} \right)^2 e^{2/L} \right]^{-1}, \end{aligned} \quad (30b)$$

$$c_2 = \left[ -c_1 \left( \frac{1}{4} + \frac{1}{2} \frac{D}{L} \right) e^{1/L} - \frac{1}{4} \frac{S_0}{\sigma_a} \right] e^{1/L} \left( \frac{1}{4} - \frac{1}{2} \frac{D}{L} \right)^{-1}. \quad (30c)$$

Table 9 shows the errors between the DGFEM solution and the analytic diffusion equation for various cell sizes. For all cell sizes, the Robin boundary condition method achieves errors on the order of  $10^{-10}$  or better. This helps confirm the correct implementation of the vacuum boundary conditions on the DSA equation. We also notice that as  $\varepsilon \rightarrow 0$ , we have  $D = \varepsilon/(3\sigma_t) \rightarrow 0$ , and

$$\left[ (\kappa_e \varphi, v)_{\partial\mathcal{D}^d} - \frac{1}{2} (\varphi, D\partial_n v)_{\partial\mathcal{D}^d} - \frac{1}{2} (D\partial_n \varphi, v)_{\partial\mathcal{D}^d} \right] \rightarrow (\kappa_e \varphi, v)_{\partial\mathcal{D}^d}. \quad (31)$$

Further, we have  $\kappa_e^{IP} \rightarrow 0$  and thus,  $\kappa_e \rightarrow 1/4$  by Equation 21. So, as the material becomes increasingly optically thick, the homogeneous Dirichlet boundary condition converges to

$$\frac{1}{4} (\varphi, v)_{\partial\mathcal{D}^d}, \quad (32)$$

the homogeneous Robin boundary condition implementation.

Table 2:  $L_2$  norm of the errors between the diffusion equation using the given boundary condition method and the reference solution (1-D analytic solution) using 3<sup>rd</sup>-order elements,  $C = 4$ , on an orthogonal mesh with 2304 zones.

$\varepsilon$	Robin BC	Dirichlet BC
10	$4.05 \times 10^{-11}$	0.722
1	$2.03 \times 10^{-10}$	0.363
0.1	$3.39 \times 10^{-10}$	0.0607
0.01	$3.63 \times 10^{-10}$	0.00650
$1 \times 10^{-3}$	$3.66 \times 10^{-10}$	$6.55 \times 10^{-4}$
$1 \times 10^{-4}$	$3.66 \times 10^{-10}$	$6.56 \times 10^{-5}$
$1 \times 10^{-5}$	$3.67 \times 10^{-10}$	$6.54 \times 10^{-6}$
$1 \times 10^{-6}$	$4.08 \times 10^{-10}$	$3.91 \times 10^{-7}$

### 3.2.2 Sensitivity Study of the Spectral Radius

Figure 11 shows the spectral radius of various finite element orders on an orthogonal mesh for  $C = 2$  using the homogeneous Robin boundary condition. We observe that the peaks from Figure 3 no longer appear. Thus, it is challenging to determine when the “switch” between the IP and DCF methods occurs. Contrasting the homogeneous Dirichlet boundary condition method, there is very little sensitivity of finite element order in the intermediate optical thickness region. However, we observe slight dependencies of the spectral radius to the finite element order in the optically thin and optically thick regions. Also, contrasting the Dirichlet boundary conditions, the spectral radii in the optically thick region are substantially higher with the Robin boundary conditions.

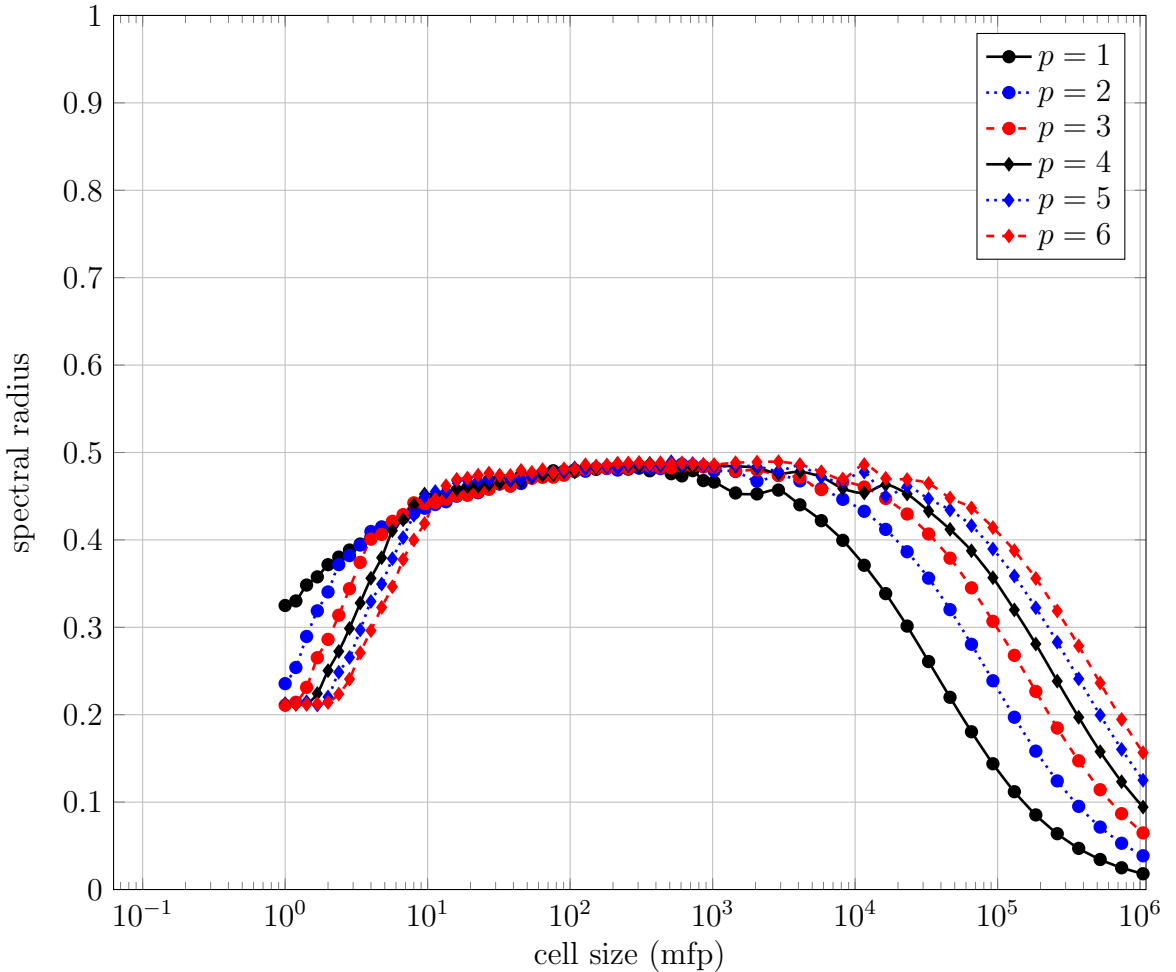


Figure 11: Spectral radius data for varying  $p$  with  $C = 2$  on an orthogonal mesh using the vacuum boundary MIP DSA method.

Figure 12 shows the spectral radius of various finite element orders on an orthogonal mesh for  $C = 4$  using the homogeneous Robin boundary condition. Again, we observe that the peaks from Figure 3 no longer appear. Contrasting the homogeneous Dirichlet boundary condition method, there is very little sensitivity of finite element order in the intermediate optical thickness region. However, we observe slight dependencies of the spectral radius to the finite element order in the optically thin and optically thick regions. Also, contrasting the Dirichlet boundary conditions, the spectral radii in the optically thick region are substantially higher with the Robin

boundary conditions. The results in Figure 12 are remarkably similar to Figure 11, indicating that the spectral radius is less sensitive to the interior surface terms than the problem boundary conditions.

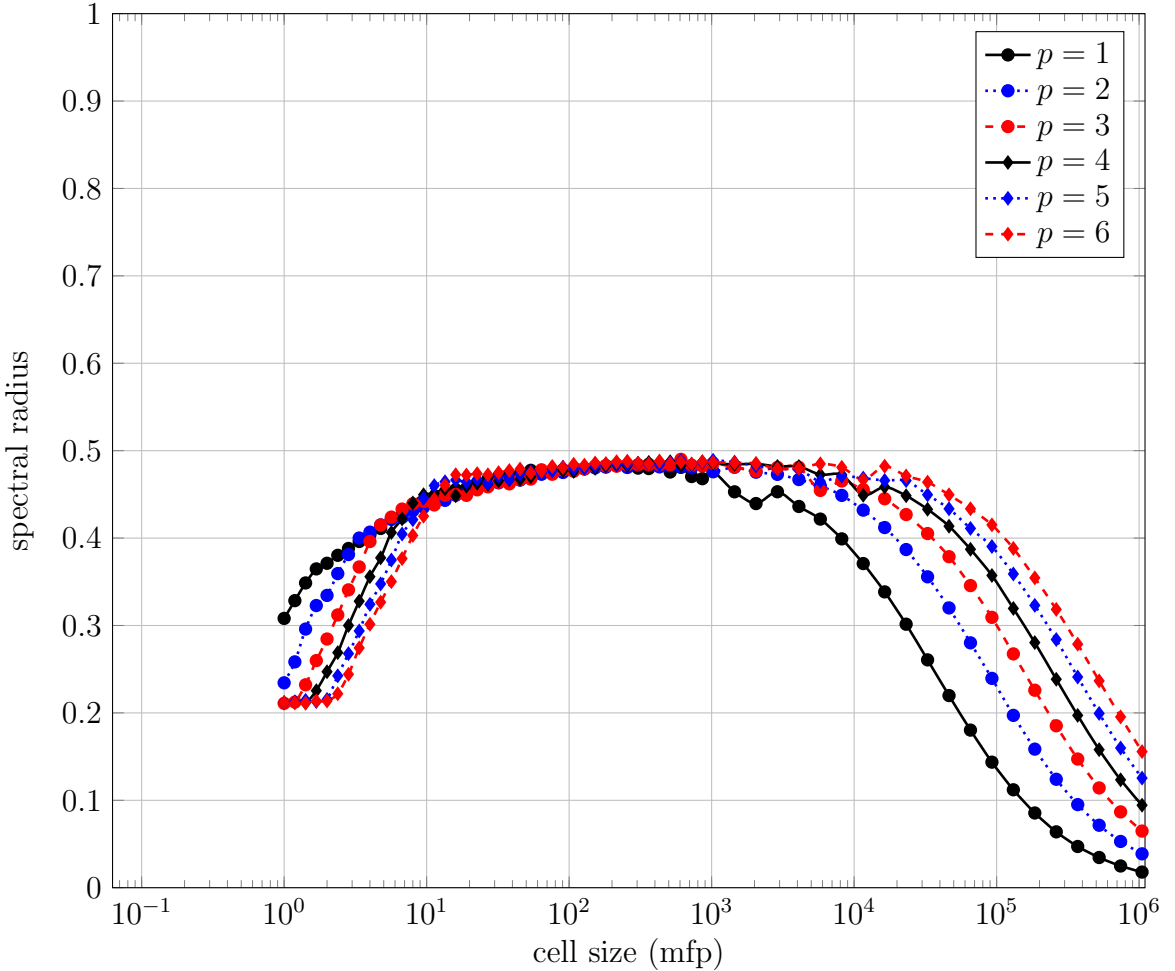


Figure 12: Spectral radius data for varying  $p$  with  $C = 4$  on an orthogonal mesh using the zero incident current DSA method.

Figure 13 shows the spectral radius of various finite element orders on an orthogonal mesh for  $C = 6$  using the homogeneous Robin boundary condition. Again, we observe that the peaks from Figure 3 no longer appear. However, similar to Figure 5,

there is a rise in the spectral radius (a “hump”) in nearly the same cell size range. The remainder of the spectral radii profiles are very similar to those of Figures 11 and 12. Since there is no spectral radius improvement in any other cell regimes, this choice for  $C$  is undesirable. Again, we observe the spectral radii in the optically thick region are substantially higher with the Robin boundary conditions than with using homogeneous Dirichlet boundary conditions.

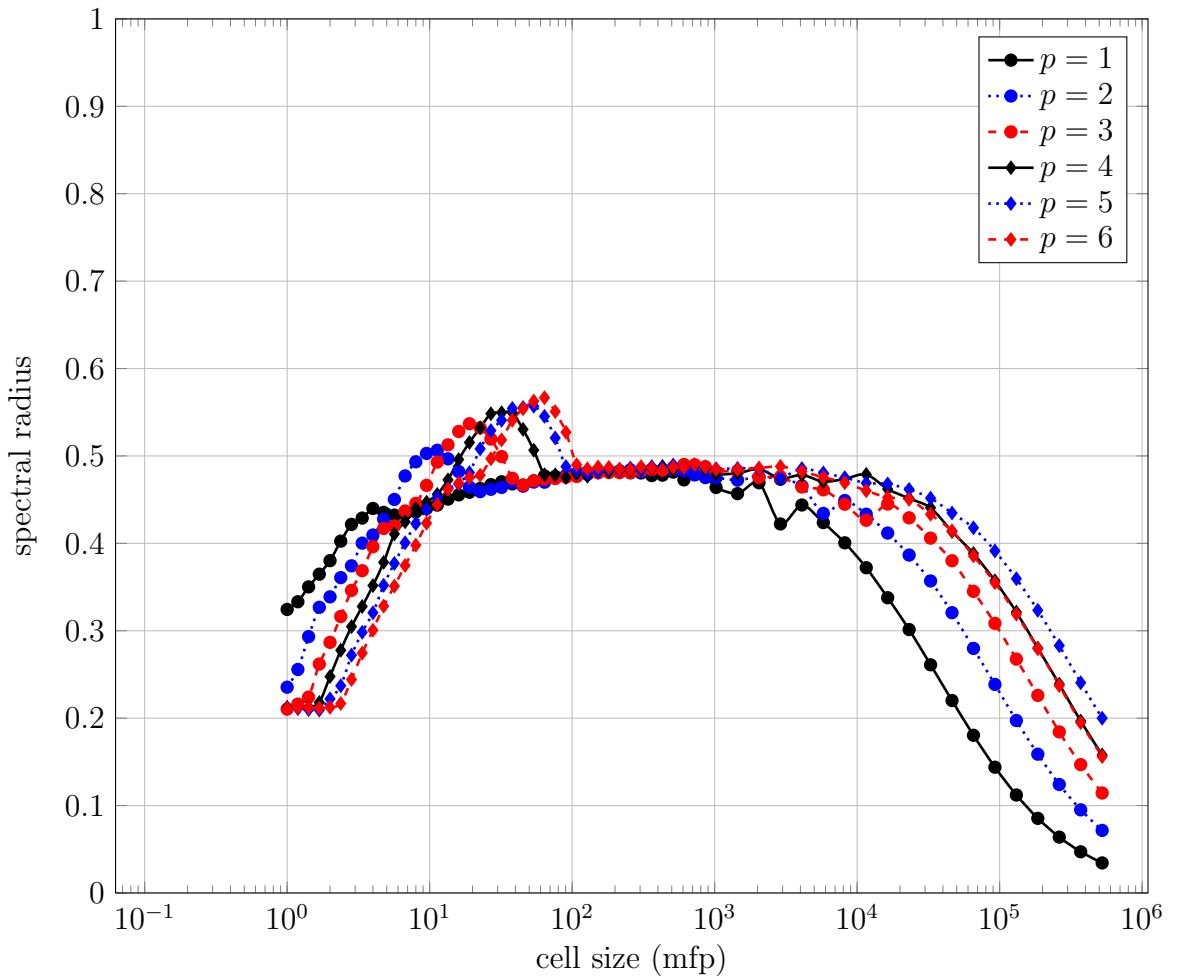


Figure 13: Spectral radius data for varying  $p$  with  $C = 6$  on an orthogonal mesh using the zero incident current DSA method.

### 3.3 Conclusions

We characterized the spectral radius for several combinations of the constant  $C$  and the finite element order  $p$  for variable cell sizes. While we see SI acceleration in all cases, there is not a set of parameters that promote smaller spectral radii in all regimes, but problem constraints may motivate the parameter choice. Each variable,  $C$  and  $p$ , increased the spectral radius to some degree. The spectral radius using the Robin boundary condition method is substantially less sensitive to the constant  $C$  than with Dirichlet boundary conditions. The Robin boundary condition method is very smooth and consistently below  $\rho = 0.6$  through the range of cell sizes. However, the Robin boundary condition method has substantially larger spectral radii in the optically thick regime.

In the future, we will perform a Fourier analysis of the implemented vacuum boundary condition method. We will also consider a wide range of problems including heterogeneous media. To avoid a substantial degradation in effectiveness, this requires a relatively modern technique of preconditioning a Krylov method with the DSA operator [65]. Wang and Ragusa [22] observed this degradation of effectiveness but MIP DSA has yet to be used as a preconditioner to a Krlyov method.

## 4 R-Z Geometry

Solving the transport equation in different coordinate systems may provide simpler ways of modeling a particular geometry or symmetry. In this section, we derive the *R-Z* transport equation to be solved. It assumes there is no variation in the azimuthal direction (of a cylinder), so problems in *R-Z* geometry look very similar to problems in *X-Y* geometry. The streaming operator in cylindrical geometry is [2]

$$\boldsymbol{\Omega} \cdot \nabla \psi = \frac{\mu}{r} \frac{\partial}{\partial r}(r\psi) + \frac{\eta}{r} \frac{\partial \psi}{\partial \zeta} + \xi \frac{\partial \psi}{\partial z} - \frac{1}{r} \frac{\partial}{\partial \omega}(\eta\psi), \quad (33)$$

where  $\boldsymbol{\Omega}$  is the direction of travel unit vector,  $\psi$  is the angular flux, and

$$\mu \equiv \boldsymbol{\Omega} \cdot \hat{e}_r = \sqrt{1 - \xi^2} \cos \omega = \sin(\theta) \cos(\omega), \quad (34)$$

$$\eta \equiv \boldsymbol{\Omega} \cdot \hat{e}_\theta = \sqrt{1 - \xi^2} \sin \omega = \sin(\theta) \sin(\omega), \quad (35)$$

$$\xi \equiv \boldsymbol{\Omega} \cdot \hat{e}_z = \cos(\theta). \quad (36)$$

The variables  $\mu$ ,  $\eta$ ,  $\xi$ ,  $\omega$ , and  $\theta$  are shown in the cylindrical coordinate system in Figure 14. We assume there is no solution variation in the azimuthal direction, i.e.

$$\frac{\partial \psi}{\partial \zeta} \equiv 0, \quad (37)$$

which simplifies the streaming term to

$$\boldsymbol{\Omega} \cdot \nabla \psi = \frac{\mu}{r} \frac{\partial}{\partial r}(r\psi) + \xi \frac{\partial \psi}{\partial z} - \frac{1}{r} \frac{\partial}{\partial \omega}(\eta\psi). \quad (38)$$

The transport equation in *R-Z* geometry is then

$$\begin{aligned} \frac{\mu}{r} \frac{\partial}{\partial r} r\psi(r, z, \boldsymbol{\Omega}) + \xi \frac{\partial}{\partial z} \psi(r, z, \boldsymbol{\Omega}) - \frac{1}{r} \frac{\partial}{\partial \omega} \eta\psi(r, z, \boldsymbol{\Omega}) + \sigma_t(r, z) \psi(r, z, \boldsymbol{\Omega}) \\ = \frac{1}{4\pi} \int_{4\pi} \sigma_s(r, z) I(r, z, \boldsymbol{\Omega}') d\Omega' + S_0(r, z, \boldsymbol{\Omega}) \end{aligned} \quad (39)$$

where  $\sigma_t$  is the total cross section,  $\sigma_s$  is the scattering cross section, and  $S_0$  is an isotropic source as before. The streaming term describes the motion of the parti-

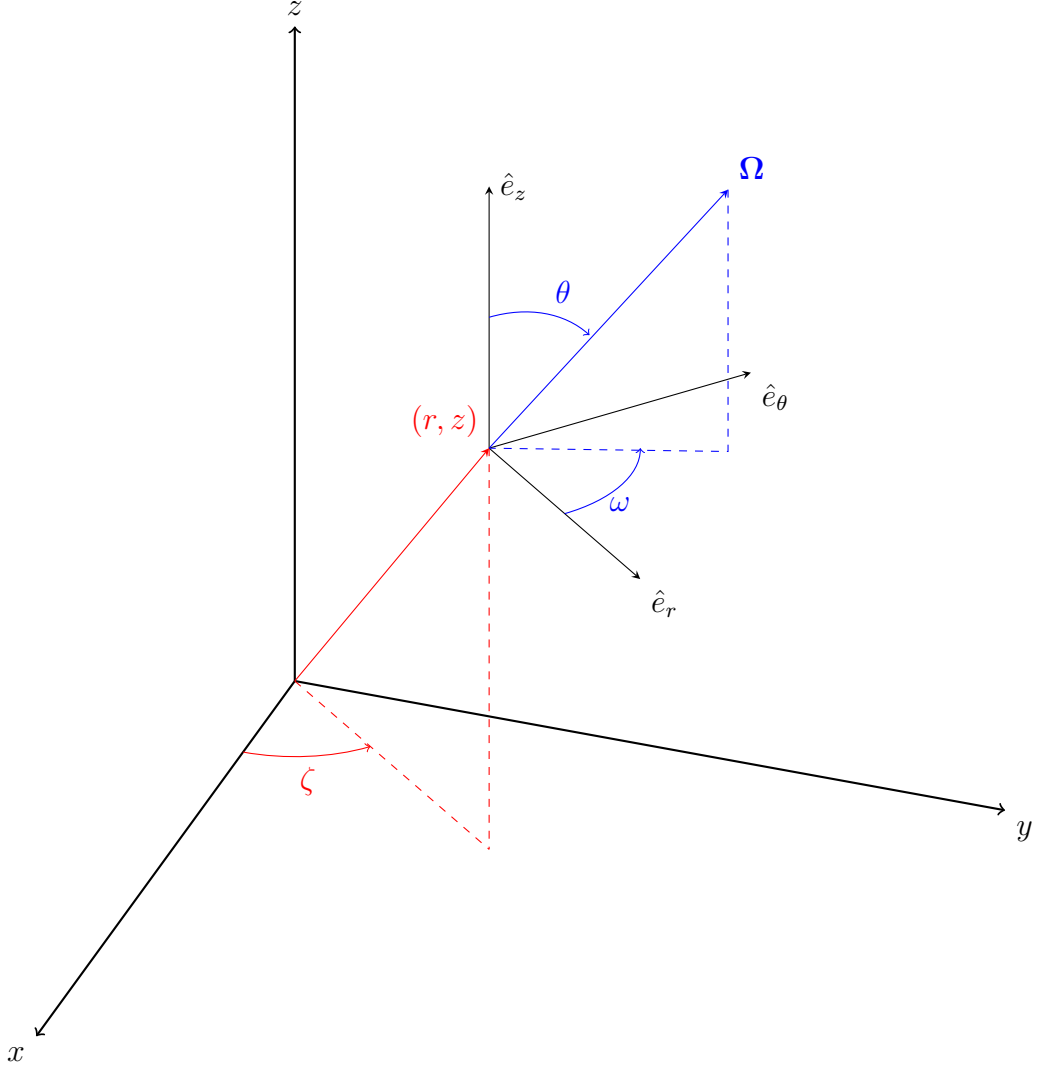


Figure 14: Cylindrical space-angle coordinate system showing the position  $(r, z)$  and direction of travel  $\Omega$ .

cle density into or out of a volume. Since the streaming term now has an angular derivative (two angular derivatives in 3-D), the spatial streaming now depends on the direction of travel. The  $\hat{e}_r$  axis in Figure 14 is always in the same direction as the  $r$ -axis. Considering a particle traveling in a straight direction  $\Omega$ , as the particle changes position, the coordinate axis defining  $\Omega$  changes. This couples the spatial and angular axes when defining the phase space of a particle. First, we must discretize

the direction of particle travel.

The remainder of this section is outlined as follows. In Section 4.1, we discretize the  $R$ - $Z$  transport equation using the discrete ordinates method. In Section 4.2, we perform the discretization of the spatial domain using HO DFEM. In Section 4.3, we present spatial convergence rates along with other elementary results. In Section 4.4, we perform an analysis of preserving spherical symmetry. In Section 4.5, we stress the methodology with an optically thick and diffusive problem. In Section 4.6, we further stress the methodology and solve a highly heterogeneous problem. Finally, in Section 4.7, we provide concluding remarks.

## 4.1 Angular Discretization

Discretizing Equation 39 with a level-symmetric angular quadrature results in

$$\begin{aligned} \frac{\mu_{n,m}}{r} \frac{\partial}{\partial r} r \psi_{n,m}(r, z) + \xi_n \frac{\partial}{\partial z} \psi_{n,m}(r, z) - \frac{1}{r} \frac{\partial}{\partial \omega} \eta_{n,m} \psi_{n,m}(r, z) + \sigma_t(r, z) \psi_{n,m}(r, z) \\ = \frac{1}{4\pi} \int_{4\pi} \sigma_s(r, z) \phi(r, z, \Omega') d\Omega' + S_0(r, z, \Omega) \end{aligned} \quad (40)$$

for direction  $\Omega_{n,m}$ , where index  $n$  describes a level of quadrature with constant  $\xi$  and the  $m$  index denotes the quadrature point on that level. The  $(n, m)$  indexing is shown in Figure 15.

One of the major challenges is handling the angular derivative term. Lewis and Miller [2] describes an approximation for the partial derivative of the intensity with respect to  $\omega$ :

$$-\frac{1}{r} \frac{\partial}{\partial \omega} \eta_{m,n} \psi_{n,m}(r, z) = \frac{\alpha_{m+1/2}^n \psi_{n,m+1/2}(r, z) - \alpha_{m-1/2}^n \psi_{n,m-1/2}(r, z)}{rw_{n,m}} \quad (41)$$

where  $\alpha_{m+1/2}^n$  and  $\alpha_{m-1/2}^n$  are angular differencing coefficients, and  $w_{n,m}$  is the angular

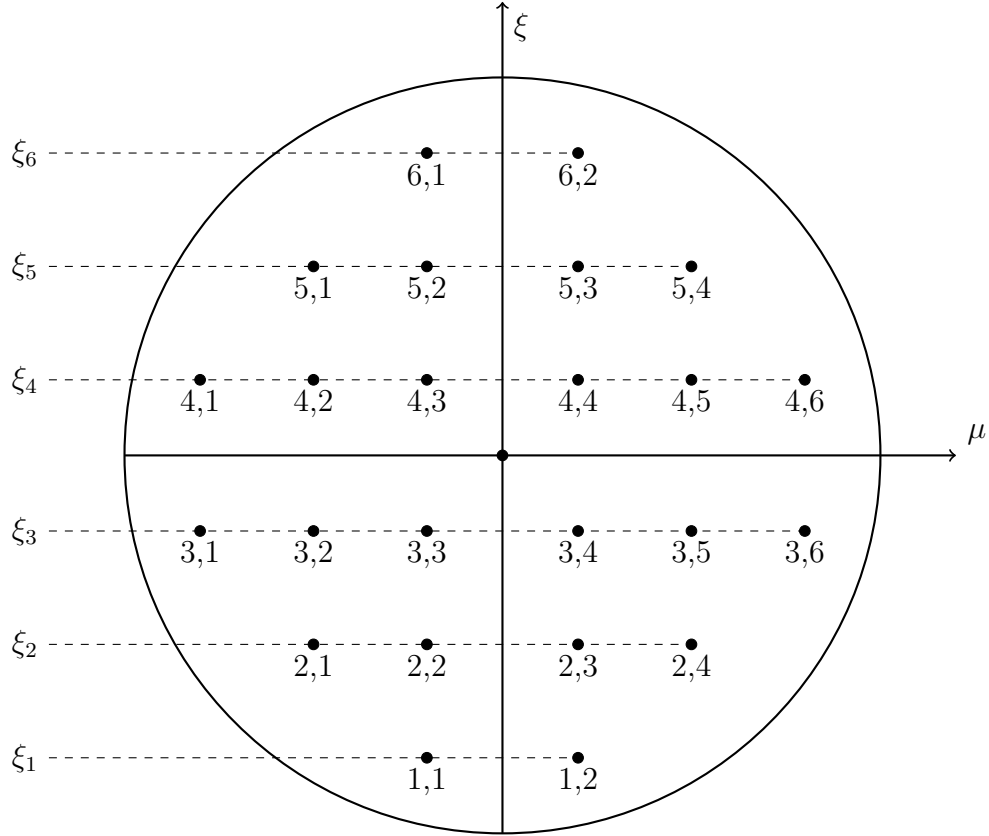


Figure 15: Angular discretization showing  $(\xi, \mu)$  pairs; adapted from [2]

quadrature weight. We substitute this into Equation 50,

$$\begin{aligned}
 & \frac{\mu_{n,m}}{r} \frac{\partial}{\partial r} r \psi_{n,m}(r, z) + \xi_n \frac{\partial}{\partial z} \psi_{n,m}(r, z) \\
 & + \frac{\alpha_{m+1/2}^n \psi_{n,m+1/2}(r, z) - \alpha_{m-1/2}^n \psi_{n,m-1/2}(r, z)}{rw_{n,m}} + \sigma_t(r, z) \psi_{n,m}(r, z) \\
 & = \frac{1}{4\pi} \int_{4\pi} \sigma_s(r, z) \psi(r, z, \Omega') d\Omega' + \frac{1}{4\pi} S_0(r, z) \quad (42)
 \end{aligned}$$

Here, we pause to notice that there are similarities and differences between a Cartesian discretization. The absorption term, axial derivative term, and right-hand-side are the same in both coordinate systems. The differences arise in the radial and angular derivative terms.

After multiplying through by the radius  $r$ , the radial derivative term has a factor

of  $r$  inside the derivative. The angular derivative term is also new and does not resemble a mass matrix so MFEM will require additional modification.

Requiring Equation 42 to satisfy the uniform infinite medium solution results in the condition,

$$\alpha_{m+1/2}^n = \alpha_{m-1/2}^n - \mu_{n,m} w_{n,m} \quad (43)$$

If  $\alpha_{1/2}^n$  is known, then the remaining coefficients are uniquely determined. To find  $\alpha_{1/2}^n$ , we require that Equation 42 satisfy the conservation equation (Eq. 39). Given a quadrature set with an even number of  $\mu_{n,m}$  values, setting  $\alpha_{1/2}^n = 0$  results in  $\alpha_{M_n+1/2}^n = 0$  per Equation 43 and the conservation equation is satisfied.

A relationship between  $\psi_{n,m}$ ,  $\psi_{n,m+1/2}$ , and  $\psi_{n,m-1/2}$  must be established. A weighted diamond difference scheme has been established by Morel and Montry [66],

$$\psi_{n,m}(r, z) = \tau_{n,m} \psi_{n,m+1/2} + (1 - \tau_{n,m}) \psi_{n,m-1/2} \quad (44)$$

where  $\tau_{n,m}$  linearly interpolates  $\mu$ :

$$\tau_{n,m} = \frac{\mu_{n,m} - \mu_{n,m-1/2}}{\mu_{n,m+1/2} - \mu_{n,m-1/2}} \quad (45)$$

with

$$\mu_{n,m+1/2} = \sqrt{1 - \xi_n^2} \cos(\varphi_{n,m+1/2}) \quad (46)$$

$$\varphi_{n,m+1/2} = \varphi_{n,m-1/2} + \pi \frac{w_{n,m}}{w_n} \quad (47)$$

$$w_n = \sum_{m=1}^{M_n} w_{n,m} \quad (48)$$

We take Equation 42, multiply through by  $r$  and perform a product rule on the

radial derivative term,

$$\begin{aligned} \mu_{n,m} \left[ \psi_{n,m}(r, z) + r \frac{\partial}{\partial r} \psi_{n,m}(r, z) \right] + r \xi_n \frac{\partial}{\partial z} \psi_{n,m}(r, z) \\ + \frac{\alpha_{m+1/2}^n \psi_{m+1/2,n}(r, z) - \alpha_{m-1/2}^n \psi_{m-1/2,n}(r, z)}{w_{n,m}} + r \sigma_t(r, z) \psi_{n,m}(r, z) \\ = \frac{r}{4\pi} \int_{4\pi} \sigma_s(r, z) \psi(r, z, \Omega') d\Omega' + \frac{r}{4\pi} S_0(r, z). \quad (49) \end{aligned}$$

We solve Equation 44 for  $\psi_{n,m+1/2}$ , perform a substitution, and move the known quantities to the right-hand-side,

$$\begin{aligned} \mu_{n,m} r \frac{\partial}{\partial r} \psi_{n,m}(r, z) + r \xi_n \frac{\partial}{\partial z} \psi_{n,m}(r, z) + \mu_{n,m} \psi_{n,m}(r, z) \\ + \frac{\alpha_{m+1/2}^n}{\tau_{n,m} w_{n,m}} \psi_{n,m}(r, z) + r \sigma_t(r, z) \psi_{n,m}(r, z) \\ = \frac{r}{4\pi} \int_{4\pi} \sigma_s(r, z) \psi(r, z, \Omega') d\Omega' + \frac{r}{4\pi} S_0(r, z) \\ + \left( \frac{1 - \tau_{n,m}}{\tau_{n,m}} \frac{\alpha_{m+1/2}^n}{w_{n,m}} + \frac{\alpha_{m-1/2}^n}{w_{n,m}} \right) \psi_{n,m-1/2}(r, z). \quad (50) \end{aligned}$$

Given a level-symmetric quadrature set, all of the  $\alpha_{n,m\pm 1/2}^n$  and  $\tau_{n,m}$  values can be computed. We solve the starting direction equation to obtain  $\psi_{n,1/2}$ . That is, we solve the  $X$ - $Y$  system for directions  $\Omega_{n,1/2}$ ,

$$\Omega_{n,1/2} \cdot \nabla \psi_{n,1/2} + \sigma_t \psi_{n,1/2} = \frac{1}{4\pi} \sigma_s \phi + \frac{1}{4\pi} S_0 \quad (51)$$

#### 4.1.1 Reflecting Boundary at $r = 0$

The angular flux at  $r = 0$  is a reflecting boundary — there is rotational symmetry around the  $z$ -axis. This arises naturally in the analytic transport equation. Beginning with Equation 39, we multiply through by  $r$ , perform a product rule on the  $r$ -derivative term and set  $r = 0$ . On the  $z$ -axis, the transport equation becomes

$$\mu \psi - \frac{\partial}{\partial \omega} (\eta \psi) = 0. \quad (52)$$

Then, performing a product rule on the angular derivative term results in,

$$\mu\psi - \psi \frac{\partial\eta}{\partial\omega} - \eta \frac{\partial\psi}{\partial\omega} = 0. \quad (53)$$

Since

$$\frac{\partial\eta}{\partial\omega} \equiv \mu, \quad (54)$$

we can simplify this to

$$\eta \frac{\partial\psi}{\partial\omega} = \eta \frac{\partial\psi}{\partial\mu} \frac{\partial\mu}{\partial\omega} = \eta^2 \frac{\partial\psi}{\partial\mu} = 0. \quad (55)$$

$$(56)$$

Finally, we write

$$\frac{\partial\psi}{\partial\omega} = 0, \quad (57)$$

and

$$\frac{\partial\psi}{\partial\mu} = 0. \quad (58)$$

That is, the angular flux does not depend on  $\omega$  (nor  $\mu$ ) along the  $z$ -axis. Analytically, the transport equation has a naturally occurring reflecting boundary at  $r = 0$ . This condition is also satisfied by the Morel and Montry discretization scheme. Beginning with Equation 42, we multiply through by  $r$ , perform a product rule on the  $r$ -derivative term, and set  $r = 0$ , resulting in

$$\mu_{n,m}\psi_{n,m} + \frac{\alpha_{m+1/2}^n \psi_{n,m+1/2} - \alpha_{m-1/2}^n \psi_{n,m-1/2}}{w_{n,m}} = 0. \quad (59)$$

We utilize the weighted diamond differencing relationship (Equation 44) to eliminate  $\psi_{n,m+1/2}$  and rearrange:

$$(\mu_{n,m} w_{n,m} \tau_{n,m} + \alpha_{m+1/2}^n) \psi_{n,m} = [(1 - \tau_{n,m}) \alpha_{m+1/2}^n + \alpha_{m-1/2}^n \tau_{n,m}] \psi_{n,m-1/2}. \quad (60)$$

We also utilize Equation 43 and rearrange:

$$(\mu_{n,m}w_{n,m}\tau_{n,m} + \alpha_{m+1/2}^n)\psi_{n,m} = (\alpha_{m+1/2}^n + \mu_{n,m}w_{n,m}\tau_{n,m})\psi_{n,m-1/2}. \quad (61)$$

Finally, this simplifies to

$$\psi_{n,m} = \psi_{n,m-1/2}, \quad (62)$$

which satisfies Equation 58.

## 4.2 Spatial Discretization

Here, we discretize the spatial domain using the discontinuous finite element method (DFEM). The methodology is similar to the Cartesian geometry. First, we subdivide a problem domain using a spatial mesh. Then, we multiply Equation 50 by a test function and integrate over the volume of a single mesh zone,

$$\begin{aligned} & (r\boldsymbol{\Omega}_{n,m} \cdot \nabla \psi_{n,m}, v_i)_{\mathcal{D}} + (\mu_{n,m}\psi_{n,m}, v_i)_{\mathcal{D}} \\ & + \left( \frac{\alpha_{m+1/2}^n}{\tau_{n,m}w_{n,m}}\psi_{n,m}, v_i \right)_{\mathcal{D}} + (r\sigma_t\psi_{n,m}, v_i)_{\mathcal{D}} \\ & = \left( \frac{r}{4\pi} \int_{4\pi} \sigma_s \psi d\Omega', v_i \right)_{\mathcal{D}} + \left( \frac{r}{4\pi} S_0, v_i \right)_{\mathcal{D}} \\ & + \left( \left( \frac{1 - \tau_{n,m}}{\tau_{n,m}} \frac{\alpha_{m+1/2}^n}{w_{n,m}} + \frac{\alpha_{m-1/2}^n}{w_{n,m}} \right) \psi_{n,m-1/2}, v_i \right)_{\mathcal{D}}, \end{aligned} \quad (63)$$

where the inner product notation,

$$(a, b)_{\mathcal{D}} \equiv \int_{\mathcal{D}} ab, \quad (64)$$

is used. We perform an integration by parts,

$$\begin{aligned}
& (r \boldsymbol{\Omega}_{n,m} \cdot \hat{n} \psi_{n,m}, v_i)_{\partial\mathcal{D}} - (r \psi_{n,m}, \boldsymbol{\Omega}_{n,m} \cdot \nabla v_i)_{\mathcal{D}} + (\mu_{n,m} \psi_{n,m}, v_i)_{\mathcal{D}} \\
& + \left( \frac{\alpha_{m+1/2}^n}{\tau_{n,m} w_{n,m}} \psi_{n,m}, v_i \right)_{\mathcal{D}} + (r \sigma_t \psi_{n,m}, v_i)_{\mathcal{D}} \\
& = \left( \frac{r}{4\pi} \int_{4\pi} \sigma_s \psi d\Omega', v_i \right)_{\mathcal{D}} + \left( \frac{r}{4\pi} S_0, v_i \right)_{\mathcal{D}} \\
& + \left( \left( \frac{1 - \tau_{n,m}}{\tau_{n,m}} \frac{\alpha_{m+1/2}^n}{w_{n,m}} + \frac{\alpha_{m-1/2}^n}{w_{n,m}} \right) \psi_{n,m-1/2}, v_i \right)_{\mathcal{D}}, \quad (65)
\end{aligned}$$

to obtain the angular and spatially discretized  $R$ - $Z$  transport equation.

We perform numerical integrations to incorporate the mesh transformation from the physical element to the reference element by employing the determinant of the Jacobian defined by Equation 11. The general volume integrations become

$$\int_{\mathcal{D}_k} a(r, z) b(r, z) dr dz = \int_0^1 d\kappa \int_0^1 d\rho a(\rho, \kappa) b(\rho, \kappa) \det(J(\rho_i, \kappa_j)) \quad (66a)$$

$$\approx \sum_{i,j}^{\zeta} w_i w_j a(\rho_i, \kappa_j) b(\rho_i, \kappa_j) \det(J(\rho_i, \kappa_j)), \quad (66b)$$

where  $\rho_i$  and  $\kappa_j$  are Gaussian integration points with associated quadrature weights  $w_i$  and  $w_j$ , and  $\zeta$  is large enough to exactly integrate the polynomials. The default integration order we used is  $\zeta = 2p + d g - 1$ , where  $p$  is the finite element order,  $d$  is the number of spatial dimensions, and  $g$  is the order of the mesh.

The numerical integration of the surface term is more complicated. The sign of  $\boldsymbol{\Omega} \cdot \hat{n}(r, z)$  is evaluated at each spatial quadrature point along some surface  $\partial\mathcal{D}_k$ . Therefore, on a non-planar surface, the sign may switch between positive and negative denoting an outgoing or incident angular flux at the location of the quadrature point. Since we perform a Gaussian integration along each surface, we are approximating a continuous function that has a discontinuous first-derivative with a polynomial shape.

We apply the upwind approximation to the surface term

$$\begin{aligned}
& \sum_{\partial\mathcal{D}_k^e} (r\boldsymbol{\Omega}_{n,m} \cdot \hat{n}\psi_{n,m}^\uparrow, v_{ki})_{\partial\mathcal{D}_k} - (r\psi_{n,m}, \boldsymbol{\Omega}_{n,m} \cdot \nabla v_i)_{\mathcal{D}_k} + (\mu_{n,m}\psi_{n,m}, v_i)_{\mathcal{D}_k} \\
& \quad + \left( \frac{\alpha_{m+1/2}^n}{\tau_{n,m}w_{n,m}}\psi_{n,m}, v_i \right)_{\mathcal{D}_k} + (r\sigma_t\psi_{n,m}, v_i)_{\mathcal{D}_k} \\
& = \left( \frac{r}{4\pi} \int_{4\pi} \sigma_s \psi d\Omega', v_i \right)_{\mathcal{D}_k} + \left( \frac{r}{4\pi} S_0, v_i \right)_{\mathcal{D}_k} \\
& \quad + \left( \left( \frac{1-\tau_{n,m}}{\tau_{n,m}} \frac{\alpha_{m+1/2}^n}{w_{n,m}} + \frac{\alpha_{m-1/2}^n}{w_{n,m}} \right) \psi_{n,m-1/2}, v_i \right)_{\mathcal{D}_k}, \quad (67)
\end{aligned}$$

where

$$\begin{aligned}
& \sum_{\partial\mathcal{D}_k} (r\boldsymbol{\Omega}_{n,m} \cdot \hat{n}(r, z)\psi_{n,m}^\uparrow, v_{ki})_{\partial\mathcal{D}_k} \\
& = \sum_{\partial\mathcal{D}_k^e} (r\boldsymbol{\Omega}_{n,m} \cdot \hat{n}(r, z)\psi_{n,m}^\uparrow, v_{ki})_{\partial\mathcal{D}_k^e} + \sum_{\partial\mathcal{D}_k^b} (r\boldsymbol{\Omega}_{n,m} \cdot \hat{n}(r, z)\psi_{n,m}^\uparrow, v_{ki})_{\partial\mathcal{D}_k^b}. \quad (68)
\end{aligned}$$

That is, we perform the upwinding approximation on the interior and the boundary surfaces. These upwinding surface integrals are numerically integrated by the following definitions:

$$\begin{aligned}
& \sum_{\partial\mathcal{D}_k^e} (r\boldsymbol{\Omega}_{n,m} \cdot \hat{n}(r, z)\psi_{n,m}^\uparrow, v_{ki})_{\partial\mathcal{D}_k^e} \\
& = \sum_{\partial\mathcal{D}_k^e} (r\boldsymbol{\Omega}_{n,m} \cdot \hat{n}(r, z)\mathcal{I}_{n,m}^+, v_{ki})_{\partial\mathcal{D}_k^e} + \sum_{\partial\mathcal{D}_k^e} (r\boldsymbol{\Omega}_{n,m} \cdot \hat{n}(r, z)\mathcal{I}_{n,m}^-, v_{ki})_{\partial\mathcal{D}_k^e}, \quad (69)
\end{aligned}$$

These upwinding surface integrals are numerically integrated by the following definitions:

$$\begin{aligned}
(r\boldsymbol{\Omega}_{n,m} \cdot \hat{n}(r, z)\mathcal{I}_{n,m}^+, v_{ki})_{\partial\mathcal{D}_k^e} & \approx \sum_g^\zeta w_g r\boldsymbol{\Omega}_{n,m} \cdot \hat{n}(r_g, z_g) v_{ki} P^+(r_g, z_g, \boldsymbol{\Omega}_{n,m}) \\
& \approx \sum_g^\zeta w_g r_g \boldsymbol{\Omega}_{n,m} \cdot \hat{n}(\rho_g, \kappa_g) v_{ki} P^+(\rho_g, \kappa_g, \boldsymbol{\Omega}_{n,m}) \det(J(\rho_g, \kappa_g)), \quad (70)
\end{aligned}$$

and

$$\begin{aligned}
(r \cdot \boldsymbol{\Omega}_{n,m} \cdot \hat{n}(r, z) \mathcal{I}_{n,m}^-, v_{ki})_{\partial\mathcal{D}_k^e} &\approx \sum_g^\zeta w_g r \cdot \boldsymbol{\Omega}_{n,m} \cdot \hat{n}(r_g, z_g) v_{ki} P^-(r_g, z_g, \boldsymbol{\Omega}_{n,m}) \\
&\approx \sum_g^\zeta w_g r_g \cdot \boldsymbol{\Omega}_{n,m} \cdot \hat{n}(\rho_g, \kappa_g) v_{ki} P^-(\rho_g, \kappa_g, \boldsymbol{\Omega}_{n,m}) \det(J(\rho_{i,g}, \kappa_g)), \quad (71)
\end{aligned}$$

where

$$P^+(r_g, z_g, \boldsymbol{\Omega}_{n,m}) = \begin{cases} \psi_{n,m}^+, & \text{if } \boldsymbol{\Omega}_{n,m} \cdot \hat{n}(r_g, z_g) < 0 \\ 0, & \text{if } \boldsymbol{\Omega}_{n,m} \cdot \hat{n}(r_g, z_g) > 0 \end{cases}, \quad (72)$$

and

$$P^-(r_g, z_g, \boldsymbol{\Omega}_{n,m}) = \begin{cases} 0, & \text{if } \boldsymbol{\Omega}_{n,m} \cdot \hat{n}(r_g, z_g) < 0 \\ \psi_{n,m}^-, & \text{if } \boldsymbol{\Omega}_{n,m} \cdot \hat{n}(r_g, z_g) > 0 \end{cases}, \quad (73)$$

where  $\psi_{n,m}^-$  is just inside cell  $k$  and  $\psi_{n,m}^+$  is just outside (i.e. in the neighboring cell that shares surface  $\partial\mathcal{D}_k^e$ ). Therefore, at each spatial quadrature point  $(r_g, z_g)$  on surface  $\partial\mathcal{D}_k^e$ , the direction of  $\boldsymbol{\Omega}_{n,m} \cdot \hat{n}(r_g, z_g)$  determines if that location is incident or outgoing. The upwind value is used if it exists or the value is set to zero. Figure 16 illustrates a surface that has both incident and outgoing angular fluxes. The blue portion represents an incident flux because  $\boldsymbol{\Omega} \cdot \hat{n}_a < 0$ . The  $P^+$  numerical integration is performed along the entire surface but only the integration points on the blue portion are nonzero. The red portion represents an outgoing flux because  $\boldsymbol{\Omega} \cdot \hat{n}_c > 0$ . The  $P^-$  numerical integration is performed along the entire surface but only the integration points on the red portion are nonzero. The default integration order we used is  $\zeta = 2p + d \cdot g - 1$  along the surface  $\partial\mathcal{D}_k^e$ , where  $d$  is the dimension of the spatial domain and  $g$  is the order of the mesh zone.

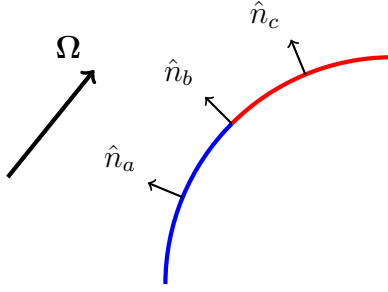


Figure 16: Example of incident and outgoing surface.

### 4.3 Spatial Convergence Study

In this section, we perform spatial convergence studies. Section 4.3.1 considers a uniform infinite medium problem. In Section 4.3.2, we use a manufactured solution with an angular dependence. Finally, in Section 4.3.3 we consider a spatial convergence study to demonstrate  $O(p + 1)$  spatial convergence rates on a smooth solution.

#### 4.3.1 Uniform Infinite Medium

We first solved a uniform infinite medium problem with  $\sigma_t = 1.0$ ,  $\sigma_s = 0.3$ , and  $S_0 = 0.7$  for 1<sup>st</sup>-order FEM on a 2<sup>nd</sup>-order mesh using  $S_4$  level-symmetric angular quadrature. The solution, shown in Figure 17, demonstrates we get the exact flat solution of  $\phi = 1.0$ .

#### 4.3.2 Angular Dependence Study

In this section, we use the method of manufactured solutions (MMS) to perform a spatial convergence study. We obtain spatial convergence rates that describe the reduction of the error as a function of spatial mesh refinement. We consider two manufactured solutions. First, a smooth manufactured solution as a function of space and angle. Then, a smooth manufactured solution just as a function of space.

First, we defined the smooth manufactured solution as a function of space and

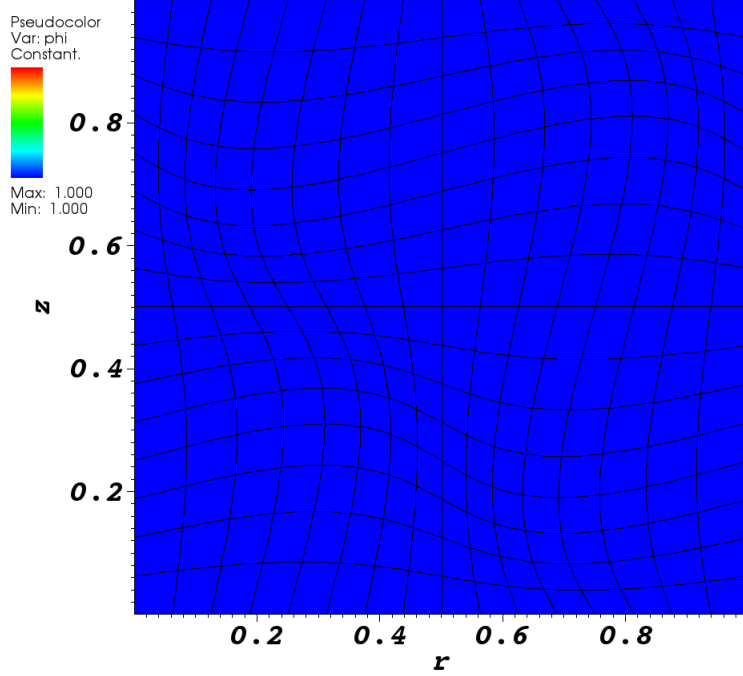


Figure 17: Uniform infinite medium solution.

angle

$$\psi = (1 - \mu^2)(1 - \xi^2) \sin\left(\frac{\pi}{2}r\right) \cos(\pi z). \quad (74)$$

We solve this with 2<sup>nd</sup>-order FEM, orthogonal quadrilateral mesh,  $\sigma_t = 1.0$ ,  $\sigma_s = 0.3$ ,  $S_0 = 0.7$ ,  $S_4$  level-symmetric angular quadrature. The solution is shown in Figure 18 and the L<sup>2</sup>-error was 0.132.

Removing the angular dependence in the manufactured solution,

$$\psi = \sin\left(\frac{\pi}{2}r\right) \cos(\pi z), \quad (75)$$

increased the accuracy of the DGFEM approximation. Shown in Figure 19, the L<sup>2</sup>-error was reduced to  $4.59 \times 10^{-5}$ . This clearly demonstrates the dependence of the spatial error upon the angular discretization.

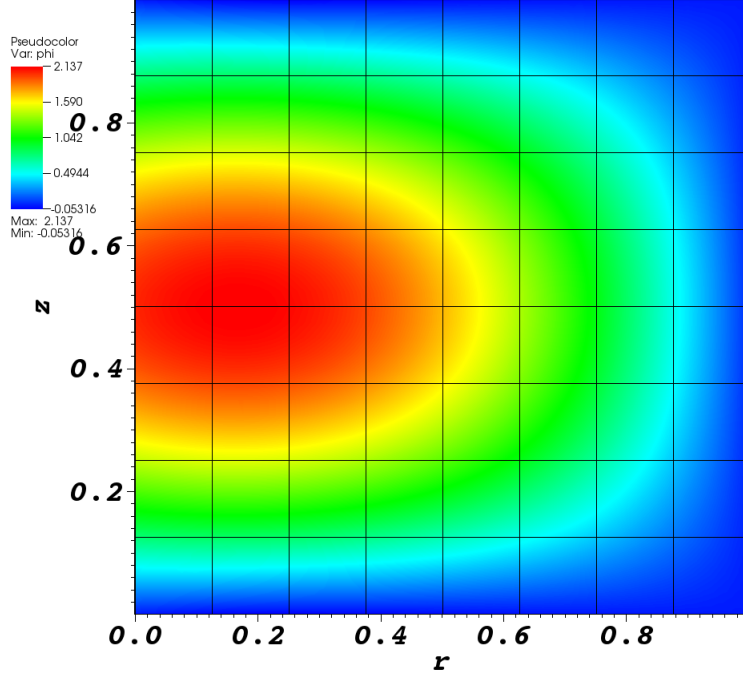


Figure 18: MMS solution for Equation 74.

#### 4.3.3 Spatial Convergence Study

We perform two spatial convergence studies here. First, we use a smooth manufactured solution to demonstrate optimal convergence rates to compare with the literature. Then, we solve a MMS problem that is only a function of space but contains discontinuities in the first-derivative to demonstrate a regularity constrained convergence rate.

Bailey et al. [21] performed this first spatial convergence study and showed 2<sup>nd</sup>-order convergence using piece-wise linear DFEM (PWLD) and bilinear DFEM (BLD) using the manufactured solution

$$\psi_{\text{MMS}}(r, z) = (\sin(\pi r) + 1 - r) \sin(\pi z), \quad (76)$$

for  $\sigma_t = 3 \text{ cm}^{-1}$  and  $\sigma_s = 0.9999\sigma_t$ . We solved this same problem using  $p =$

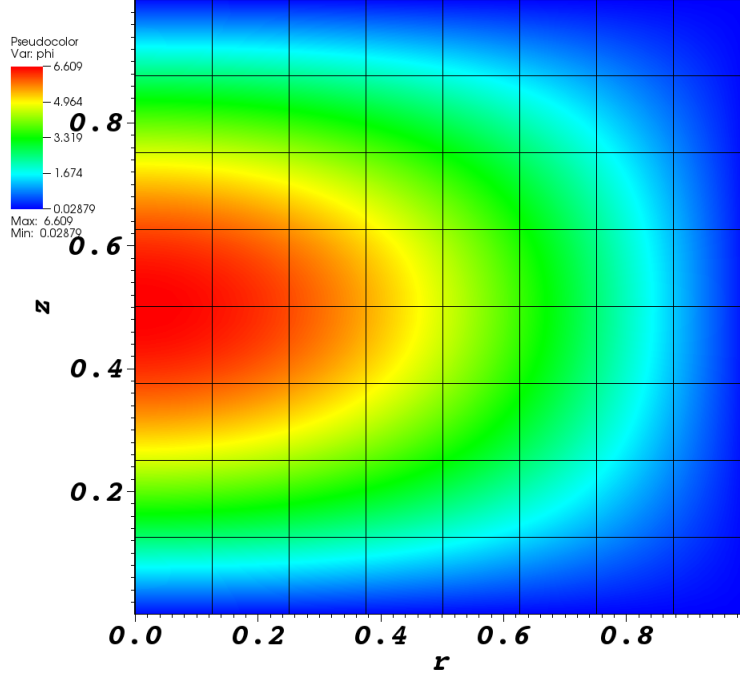


Figure 19: MMS solution for Equation 75.

$\{1, 2, 4, 6, 8\}$  on an orthogonal and 2<sup>nd</sup>-order curved mesh using  $S_8$  level-symmetric angular quadrature. We set the incident angular flux to  $\psi_{\text{MMS}}$  of Equation 76. Figure 20 shows the  $p = 2$  solution on a 2<sup>nd</sup>-order mesh.

The spatial convergence study performed by Bailey et al. demonstrated 2<sup>nd</sup>-order converge for their 1<sup>st</sup>-order methods. Figures 21a and 21b demonstrate  $O(p + 1)$  convergence on an orthogonal mesh and 2<sup>nd</sup>-order mesh, respectively. Reference lines are also provided for comparison.

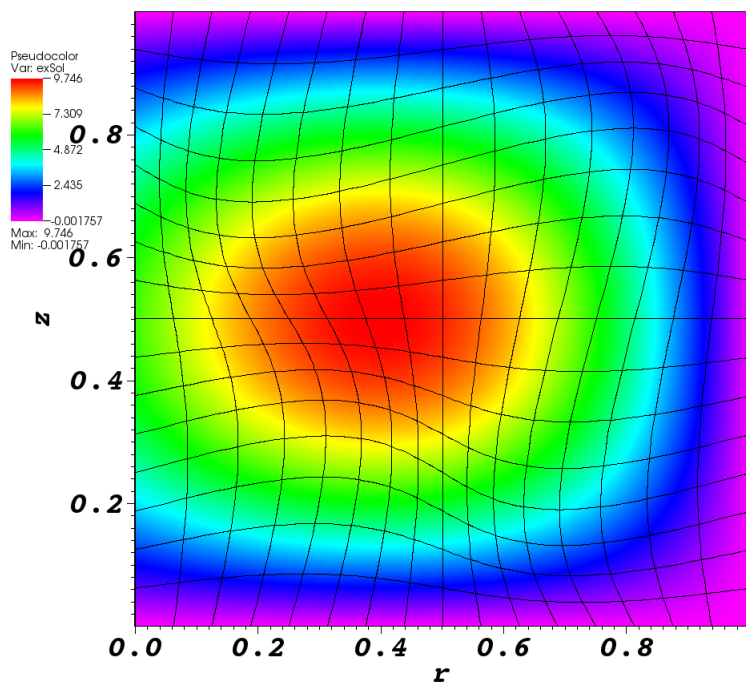


Figure 20: MMS solution to Equation 76.

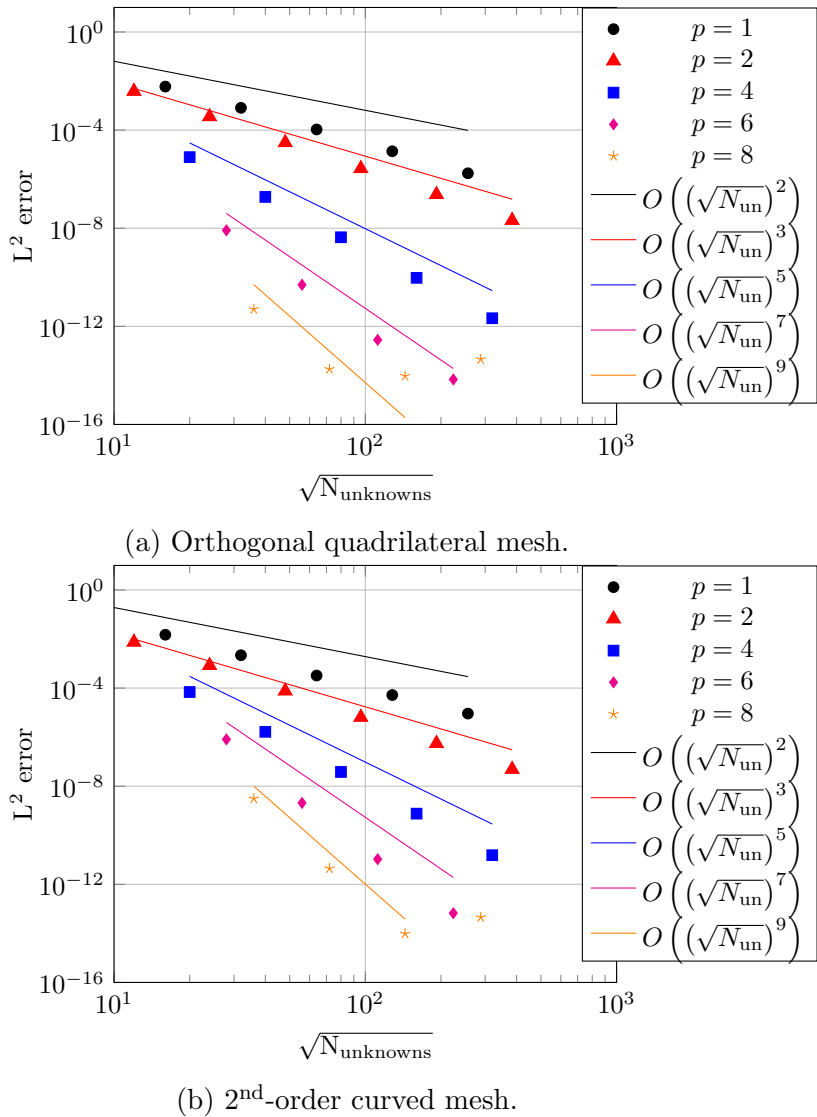


Figure 21:  $L^2$ -norm of the errors from the manufactured solution and reference lines, where  $N_{\text{unknowns}} = N_{\text{cells}}(p + 1)^2$ .

We subsequently looked at the manufactured solution

$$\psi_{\text{MMS}} = \begin{cases} 1.0 + 4.0r, & 0 \leq r < 0.33 \\ 3.31 - 3.0r, & 0.33 \leq r < 0.66, \\ 2.32 - 1.5r, & r \leq 1.0 \end{cases}, \quad (77)$$

that is continuous in  $\psi(r, z)$ , but discontinuous in  $\partial_r \psi$ . The solution, shown in Figure 22, was solved using 1<sup>st</sup>- and 2<sup>nd</sup>-order finite elements (i.e.,  $p = 1$  and  $p = 2$ , respectively),  $S_{12}$  level-symmetric angular quadrature, on a 2<sup>nd</sup>-order mesh. We refined the mesh sequentially and plotted the errors as a function of the square root of the number of unknowns in the spatial domain in Figure 23. We observe there is a degradation in the spatial convergence rate compared to the smooth (infinitely differentiable) manufactured solution. The analysis by Asadzadeh [67] predicts the spatial convergence rate to be  $O(1/2)$  for solutions that satisfy

$$|\psi_m|_1 = \left( \sum_{|\alpha|=1} \|D^\alpha \psi_m\|_{L^2(\mathcal{D})}^2 \right)^{1/2}, \quad (78)$$

and  $O(3/2)$  for solutions that satisfy

$$|\psi_m|_2 = \left( \sum_{|\alpha|=2} \|D^\alpha \psi_m\|_{L^2(\mathcal{D})}^2 \right)^{1/2}, \quad (79)$$

That is, the 1<sup>st</sup>- and 2<sup>nd</sup>-derivatives are square integrable, respectively. We observe the  $O(3/2)$  spatial convergence rate for this problem with discontinuous derivatives.

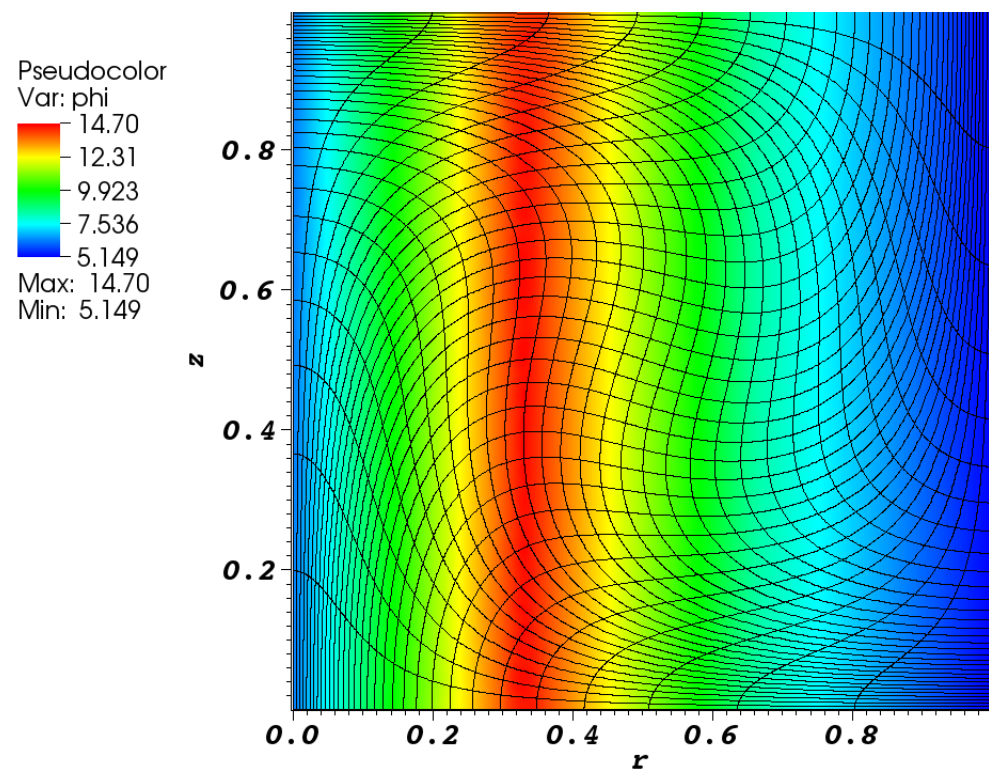


Figure 22: MMS solution to Equation 77.

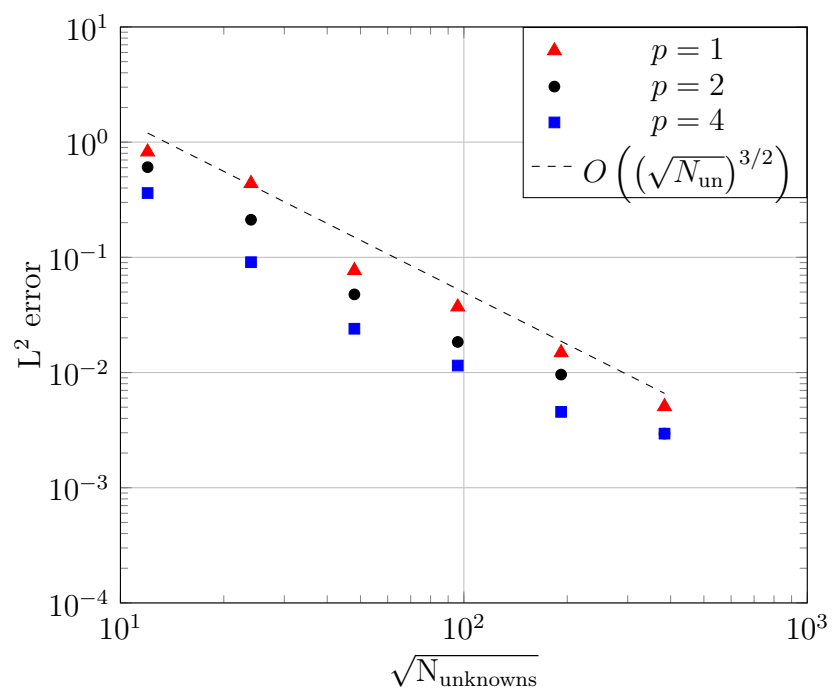


Figure 23:  $L^2$ -norm of the errors from the manufactured solution and reference lines, where  $N_{\text{unknowns}} = N_{\text{cells}}(p + 1)^2$ .

## 4.4 Axisymmetry Preservation

Numerically solving the radiation transport equation for a spherically shaped problem using spherical geometry is a very reasonable idea. However, it is also necessary to solve a spherical problem using cylindrical geometry. One particular application of the transport equation is coupling it to the hydrodynamics equations to solve radiation-hydrodynamics problems. Numerical modeling hydrodynamics problems in cylindrical geometry is common [35] so we too must demonstrate the ability to model spherical problems using cylindrical geometry. We want  $R$ - $Z$  geometry to solve and preserve 1-dimensional spherical solutions. We use MMS to solve a 1-D spherical problem using the  $R$ - $Z$  geometry spatial discretization.

We evaluate the relative asymmetry by calculating the averages of all nodes at each  $\rho$  value and

$$\phi_{\text{sym}}(\rho, \theta) = \frac{\phi_{\text{code}}(\rho, \theta) - \phi_{\text{avg}}(\rho)}{\phi_{\text{avg}}(\rho)}, \quad (80)$$

where

$$\phi_{\text{avg}}(\rho) = \frac{1}{N_{\text{nodes}}(\rho)} \sum_{i=1}^{N_{\text{nodes}}(\rho)} \phi(\rho, \theta_i) \quad (81)$$

is the average scalar flux at all nodes at the same spherical radius  $\rho = \sqrt{r^2 + z^2}$ .

The three traditional coordinate systems are Cartesian, cylindrical, and spherical. It is straight forward to describe a spatial position using any one of them. However, challenges arise when spatially discretizing. Specifically, angular derivatives arise inside the streaming term in cylindrical and spherical geometries. In modeling a spherical problem, it would seem best to use a spherical coordinate system to describe the spatial domain. However, there are more angular derivatives that must now be handled with a numerical scheme. Cylindrical geometry may be used in lieu of spherical coordinates to describe a spherical problem and is performed this way in

some hydrodynamics calculations [35]. In this section, we demonstrate the use of *R-Z* geometry to preserve a 1-D spherical solution.

Previously, two papers demonstrated spherical modeling of the radiation field using *R-Z* geometry. Brunner et al. [58] performed this analysis for the diffusion equation with an incident boundary condition on the outside of the moderately scattering homogeneous sphere with zero source. Their results were mixed whether each discretization method preserved accuracy of their analytical solution and preserved the axisymmetry. Chanland and Sama [59] performed an analysis with the time-dependent transport equation with an initial source at the center of a void. They concluded that the  $S_N$  method produces ray-effects in the void and their unique angular discretization qualitatively preserved axisymmetry. While there are applications for considering radiation propagation through a voided region, this current work focuses on material problems.

We use the method of manufactured solutions (MMS) with the manufactured solution

$$\psi_{\text{MMS}}(r, z) = \rho = \sqrt{r^2 + z^2}. \quad (82)$$

This solution is linear in the 1-D spherical coordinate  $\rho$ . We solve this for  $p = \{1, 2, 4, 8\}$ , using  $S_N$  level symmetric angular quadrature with  $N = \{4, 6, 8, 10, 12\}$ , on a 1<sup>st</sup>- and 2<sup>nd</sup>-order mesh. The problem has physical parameters  $\sigma_t = 5.0$  and  $\sigma_a = 2.0$ . We solve each of these problems on a LO mesh and a HO (2<sup>nd</sup>-order) mesh. Sections 4.4.1 and 4.4.2 show and discuss the results on the low-order and high-order meshes, respectively.

We obtain the analytical source  $S_0$  that gives the exact manufactured solution by

inserting Equation 82 into the  $R$ - $Z$  transport equation

$$\mu \frac{\partial \rho}{\partial r} + \frac{\mu}{r} \rho + \xi \frac{\partial \rho}{\partial z} - \frac{\mu}{r} \rho - \frac{\eta}{r} \frac{\partial \rho}{\partial \omega} + \sigma_t \rho = \sigma_s \rho + \frac{1}{2\pi} S_0, \quad (83)$$

$$\mu \frac{\partial \rho}{\partial r} + \xi \frac{\partial \rho}{\partial z} - \frac{\eta}{r} \frac{\partial \rho}{\partial \omega} + \sigma_t \rho = \sigma_s \rho + \frac{1}{2\pi} S_0 \quad (84)$$

where

$$\phi_{MMS} = \int_{2\pi} \psi_{MMS} d\Omega \quad (85)$$

$$= 2\pi\rho. \quad (86)$$

Given,

$$\frac{\partial \rho}{\partial r} = \frac{r}{\sqrt{r^2 + z^2}}, \quad (87)$$

$$\frac{\partial \rho}{\partial z} = \frac{z}{\sqrt{r^2 + z^2}}, \quad (88)$$

and

$$\frac{\partial \rho}{\partial \omega} = 0, \quad (89)$$

we obtain the analytical source for the manufactured solution

$$S_0 = 2\pi \left( \frac{\mu r}{\sqrt{r^2 + z^2}} + \frac{\xi z}{\sqrt{r^2 + z^2}} - \sigma_s \sqrt{r^2 + z^2} \right). \quad (90)$$

The remainder of this section is outlined as follows. In Section 4.4.1, we consider results on a 1<sup>st</sup>-order (low-order) mesh. In Section 4.4.2, we perform the same computations on a 2<sup>nd</sup>-order (high-order) mesh. Finally, in Section 4.4.3, we summarize and discuss the results of this section.

#### 4.4.1 Low-Order Mesh

In this section, we observe the sensitivity of the scalar flux spherical asymmetry to changing the discrete ordinates order, finite element order, and spatial refinement on a low-order mesh. Specifically, a low-order mesh is one that has linear surfaces.

The vertices of the low-order meshes used in this section are located in concentric rings of equal  $\rho = \sqrt{r^2 + z^2}$ . The results in this section are organized as follows: comparing the discrete ordinates order for each of  $p = \{1, 2, 4, 8\}$ , comparing each of  $p = \{1, 2, 4, 8\}$  for  $S_8$  level symmetric angular quadrature, and mesh refinement studies for each of  $p = \{1, 4\}$ .

Figure 24 shows the  $\phi_{\text{sym}}$  values calculated using Equation 80 for 1<sup>st</sup>-order finite elements on a 1<sup>st</sup>-order mesh with 120 zones for several angular quadrature discretizations. The asymmetry is plotted on a log scale. The scale colors assist in demonstrating the qualitative locations of the asymmetries. The yellow region is the least symmetric, red regions have increased symmetry, and blue regions have the most symmetry. The  $\phi_{\text{sym}}$  solution is plotted using the same finite element shape functions as the scalar flux. There is no perceptible gain in symmetry by increasing the angular discretization order. We confirm this by plotting the asymmetry values as a function of the spherical radius (i.e.,  $\rho = \sqrt{r^2 + z^2}$ ) in Figure 25. The spherical radial asymmetry solutions are indistinguishable between discrete ordinate orders. The location of the largest asymmetries are near the polar axis (i.e.,  $r = 0$ ). Moreover, Figure 26 demonstrates there is no gain in accuracy by increasing the  $S_N$  order.

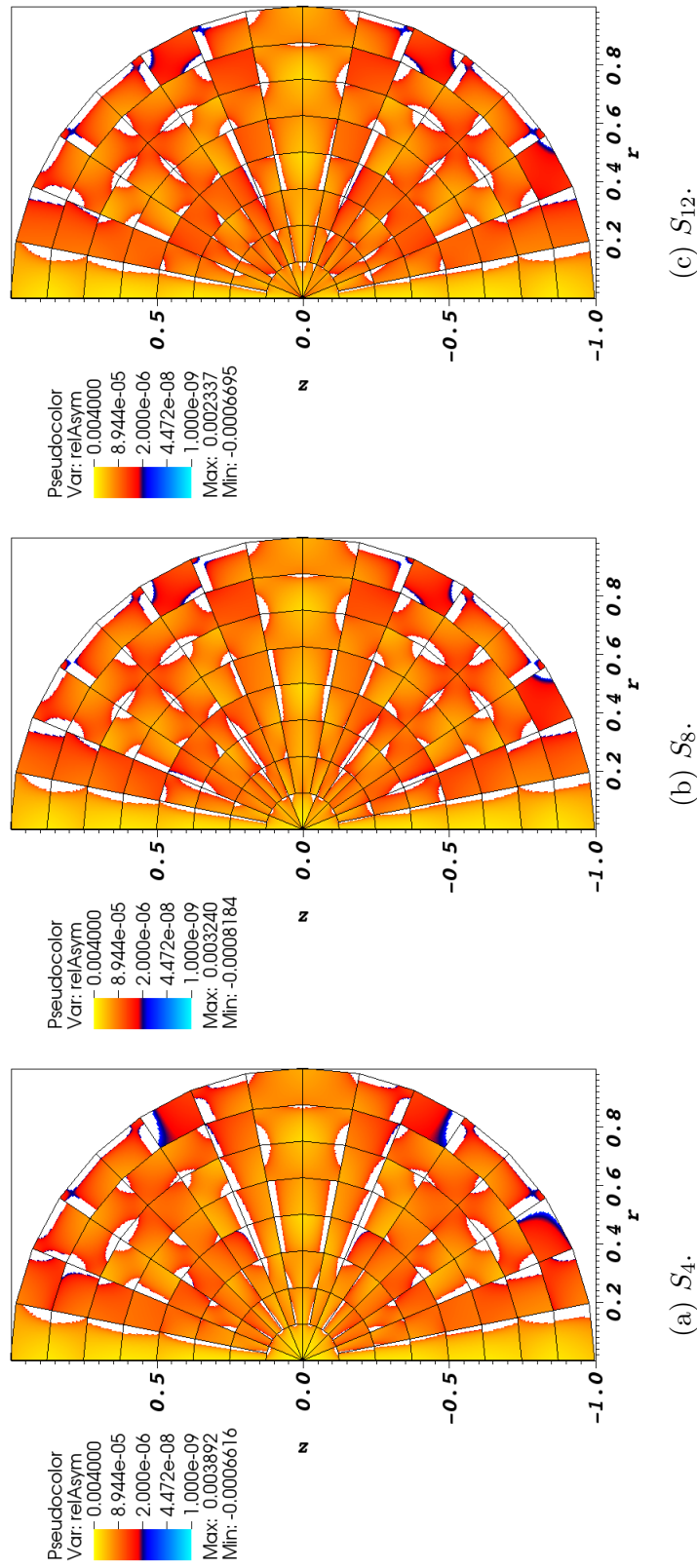


Figure 24: Relative asymmetry for 1<sup>st</sup>-order finite elements on a 1<sup>st</sup>-order mesh for given order of level-symmetric angular quadrature.

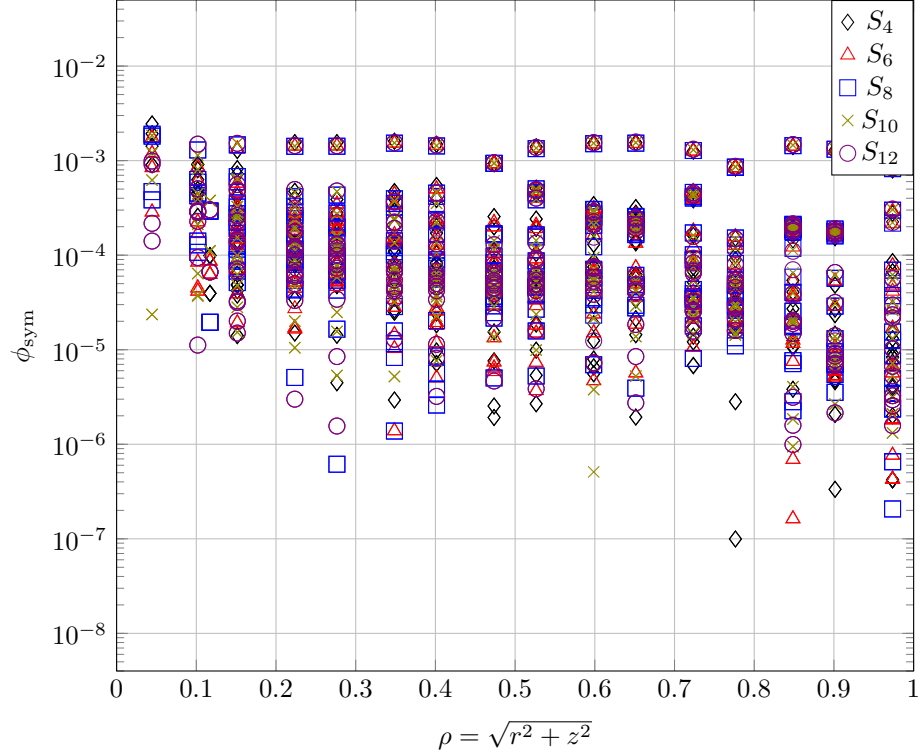


Figure 25: Measure of the asymmetry for each finite element node for the given level-symmetric angular quadrature order for 1<sup>st</sup>-order DFEM and 1<sup>st</sup>-order mesh with 120 zones (see Figure 24).

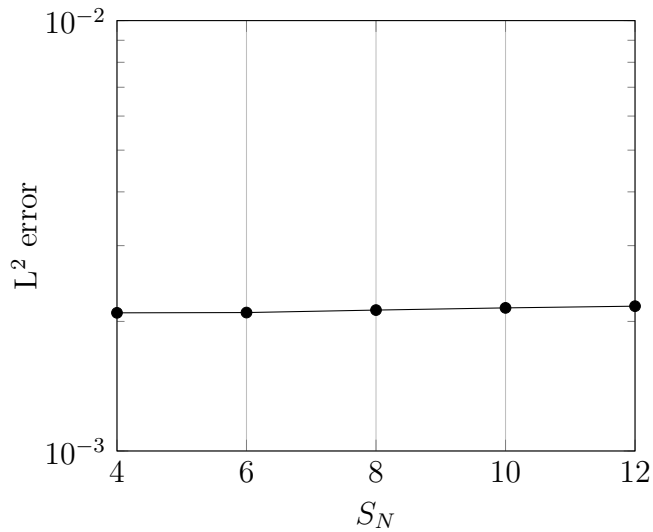


Figure 26: Accuracy of solutions for given angular quadrature using  $p = 1$  on a 1<sup>st</sup>-order mesh with 120 zones.

Figure 27 shows the  $\phi_{\text{sym}}$  values calculated using Equation 80 for 2<sup>nd</sup>-order finite elements on a 1<sup>st</sup>-order mesh with 120 zones for several angular quadrature discretizations. The asymmetry is plotted on a log scale. The scale colors assist in demonstrating the qualitative locations of the asymmetries. The yellow region is the least symmetric, red regions have increased symmetry, and blue regions have the most symmetry. The  $\phi_{\text{sym}}$  solution is plotted using the same finite element shape functions as the scalar flux. There is a little perceptible gain in symmetry (indicated by more blue area) on the periphery by increasing the angular discretization order. However, plotting the asymmetry values as a function of the spherical radius (i.e.,  $\rho = \sqrt{r^2 + z^2}$ ) in Figure 28 shows that there may not actually be any symmetry gains — the spherical radial asymmetry solutions are indistinguishable between discrete ordinate orders. The asymmetries are predominantly located near the origin (i.e.,  $\rho = \sqrt{r^2 + z^2} = 0$ ). Moreover, Figure 29 demonstrates there is no gain in accuracy by increasing the  $S_N$  order.

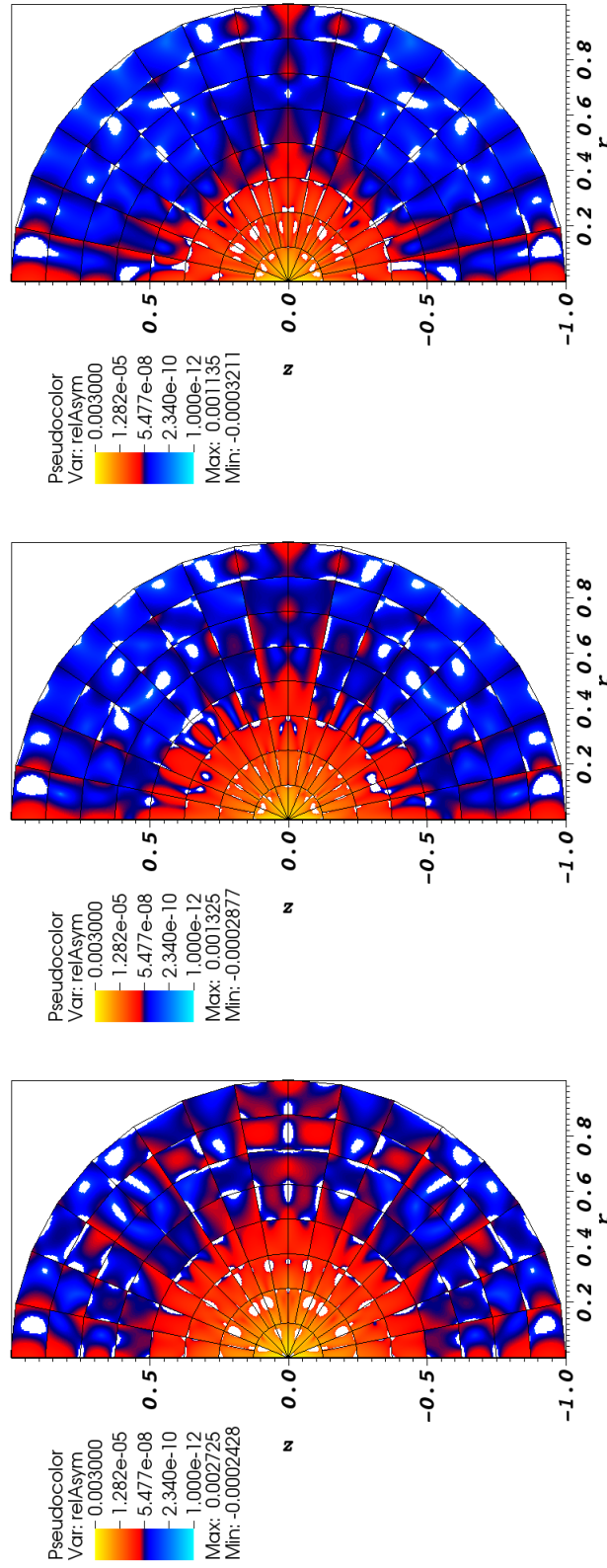


Figure 27: Relative asymmetry for 2<sup>nd</sup>-order finite elements on a 1<sup>st</sup>-order mesh for given order of level-symmetric angular quadrature.

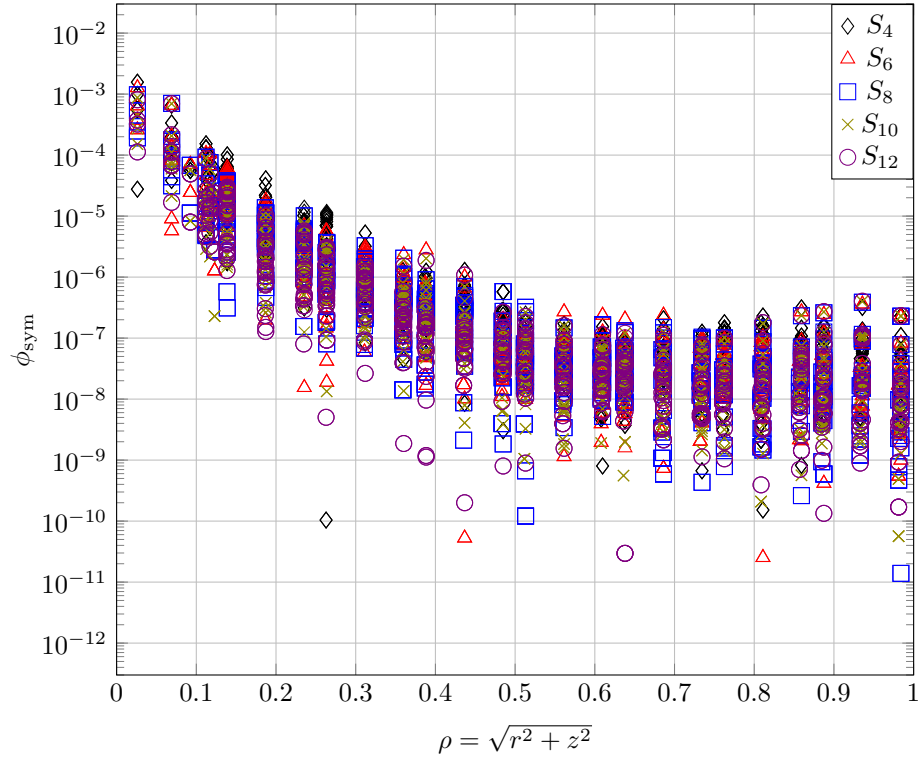


Figure 28: Measure of the asymmetry for each finite element node for the given level-symmetric angular quadrature order for 2<sup>nd</sup>-order DFEM and 1<sup>st</sup>-order mesh with 120 zones (see Figure 27).

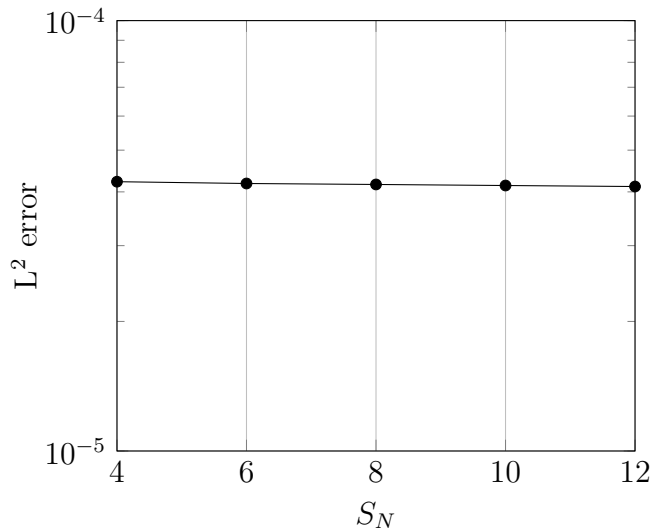


Figure 29: Accuracy of solutions for given angular quadrature using  $p = 2$  on a 1<sup>st</sup>-order mesh with 120 zones.

Figure 30 shows the  $\phi_{\text{sym}}$  values calculated using Equation 80 for 4<sup>th</sup>-order finite elements on a 1<sup>st</sup>-order mesh with 120 zones for several angular quadrature discretizations. The asymmetry is plotted on a log scale. The scale colors assist in demonstrating the qualitative locations of the asymmetries. The yellow region is the least symmetric, red regions have increased symmetry, and blue regions have the most symmetry. The  $\phi_{\text{sym}}$  solution is plotted using the same finite element shape functions as the scalar flux. There is no perceptible gain in symmetry by increasing the angular discretization order. This is confirmed by plotting the asymmetry values as a function of the spherical radius (i.e.,  $\rho = \sqrt{r^2 + z^2}$ ) in Figure 31. Unlike Figure 27, the asymmetry of the scalar flux appears to be a function of the spherical radius,  $\rho$ . Moreover, Figure 32 demonstrates there is no gain in accuracy by increasing the  $S_N$  order except for  $S_8$ , which is likely an error in transposing the data.

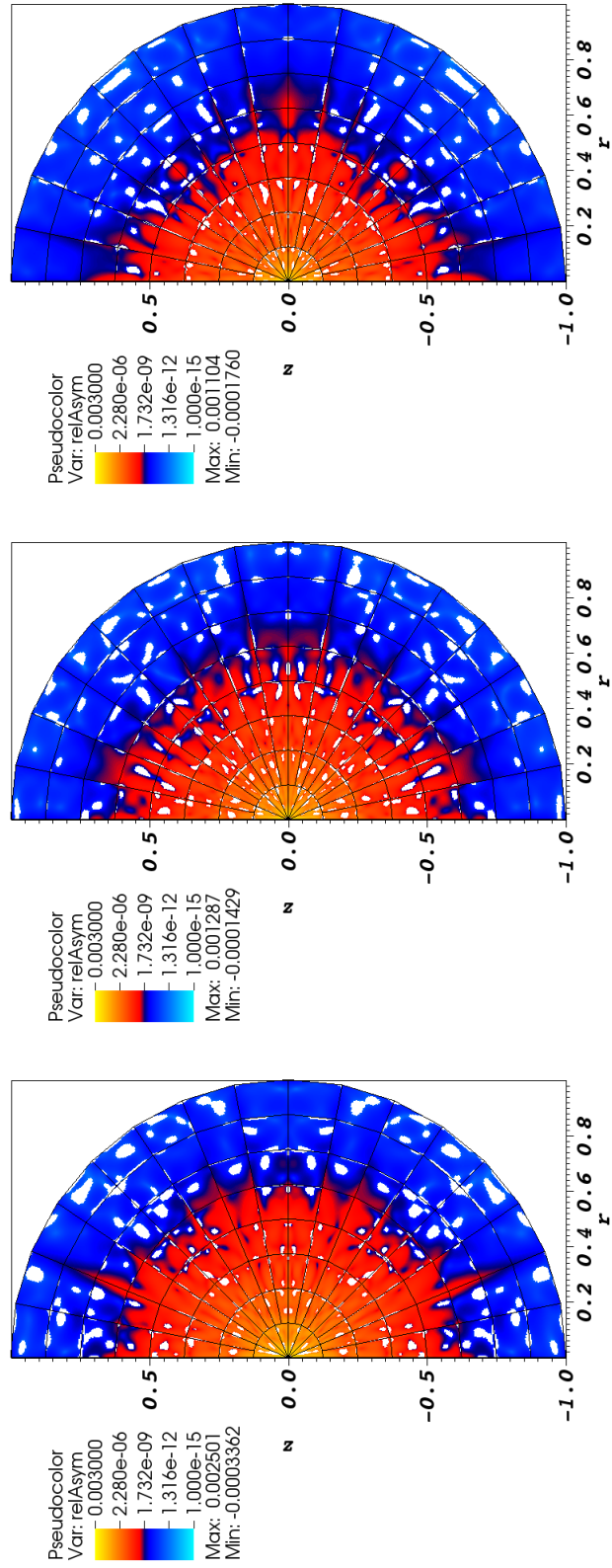


Figure 30: Relative asymmetry for 4<sup>st</sup>-order finite elements on a 1<sup>st</sup>-order mesh for given order of level-symmetric angular quadrature.

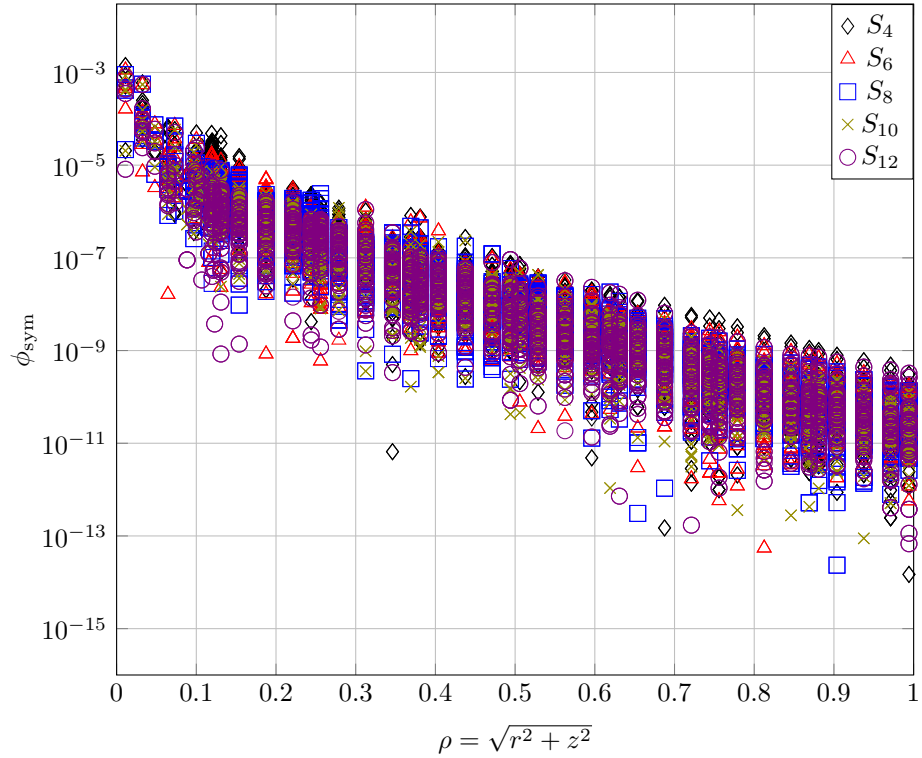


Figure 31: Measure of the asymmetry for each finite element node for the given level-symmetric angular quadrature order for 4<sup>th</sup>-order DFEM and 1<sup>st</sup>-order mesh with 120 zones (see Figure 30).

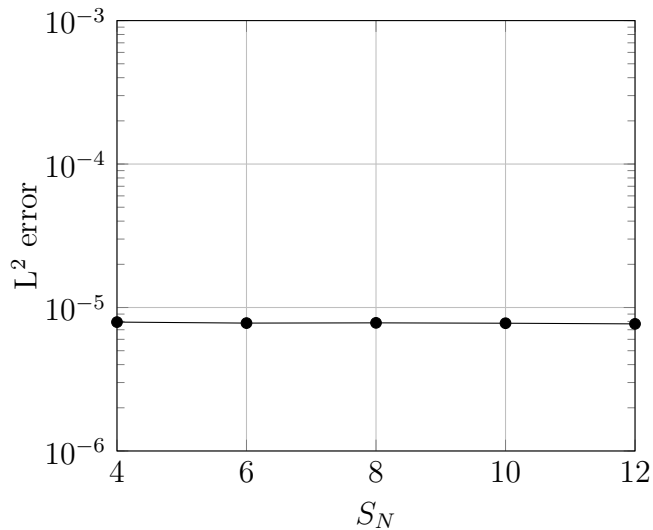


Figure 32: Accuracy of solutions for given angular quadrature using  $p = 4$  on a 1<sup>st</sup>-order mesh with 120 zones.

Figure 33 shows the  $\phi_{\text{sym}}$  values calculated using Equation 80 for 8<sup>th</sup>-order finite elements on a 1<sup>st</sup>-order mesh with 120 zones for several angular quadrature discretizations. The asymmetry is plotted on a log scale. The scale colors assist in demonstrating the qualitative locations of the asymmetries. The yellow region is the least symmetric, red regions have increased symmetry, and blue regions have the most symmetry. The  $\phi_{\text{sym}}$  solution is plotted using the same finite element shape functions as the scalar flux. There is no perceptible gain in symmetry by increasing the angular discretization order. However, Figure 34 shows there is a slight increase in symmetry from  $S_4$  for  $\rho \geq 0.7$ . Similar to Figure 30, the asymmetry of the scalar flux appears to be a function of the spherical radius,  $\rho$ . Moreover, Figure 35 demonstrates there is an increase in accuracy by increasing the finite element order.

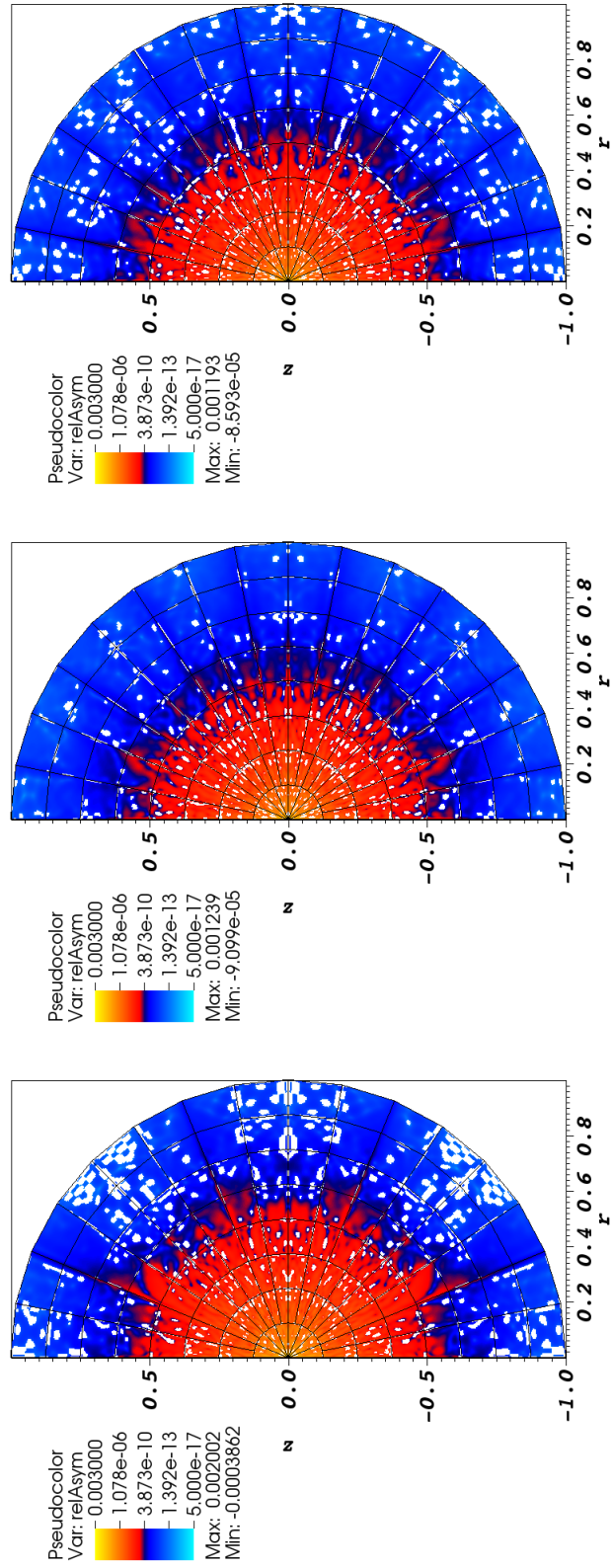


Figure 33: Relative asymmetry for 8<sup>st</sup>-order finite elements on a 1<sup>st</sup>-order mesh for given order of level-symmetric angular quadrature.

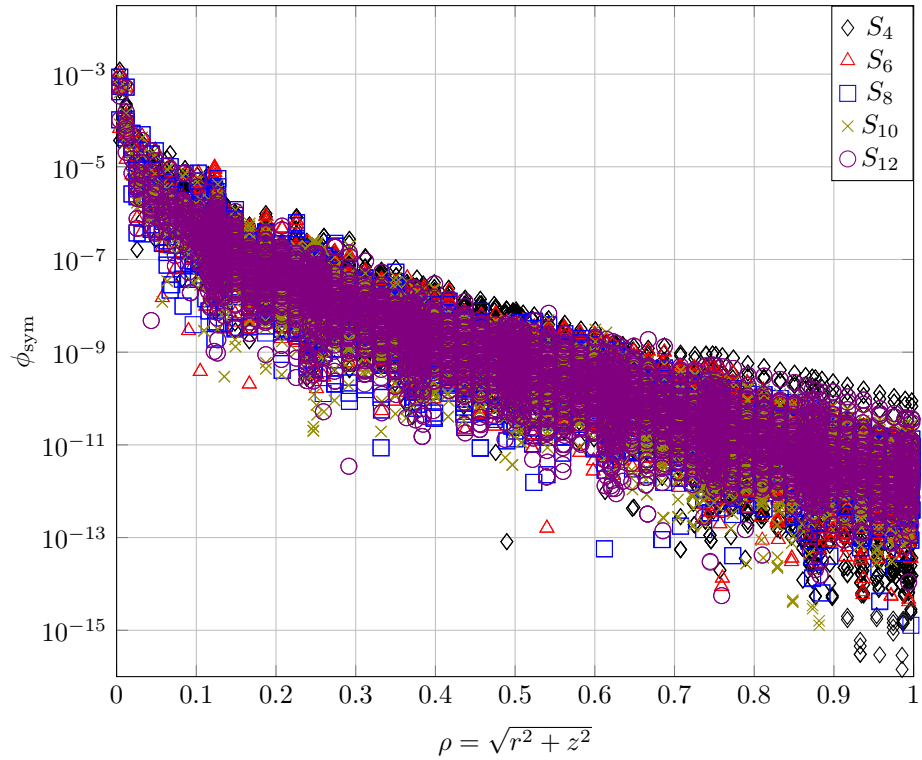


Figure 34: Measure of the asymmetry for each finite element node for the given level-symmetric angular quadrature order for 8<sup>th</sup>-order DFEM and 1<sup>st</sup>-order mesh with 120 zones (see Figure 33).

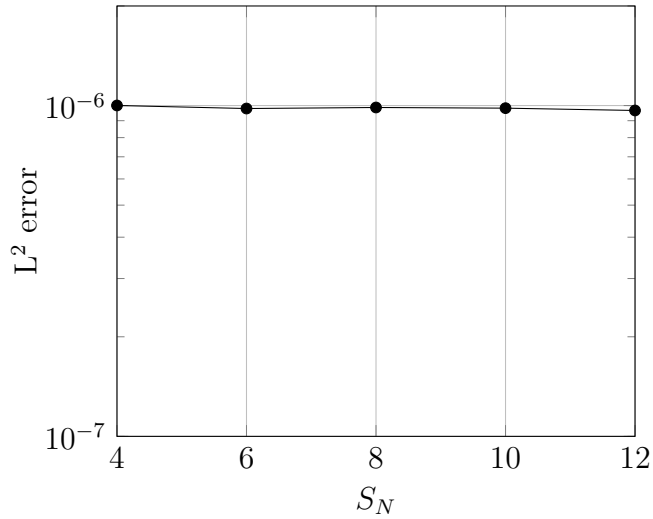


Figure 35: Accuracy of solutions for given angular quadrature using  $p = 8$  on a 1<sup>st</sup>-order mesh with 120 zones.

Figure 36 shows the  $\phi_{\text{sym}}$  values calculated using Equation 80 for  $p = \{1, 2, 4\}$  finite elements on a 2<sup>nd</sup>-order mesh with 120 zones with  $S_8$  level-symmetric angular quadrature repeated from Figures 24, 27, and 30 and plotted on the same scale. Increasing the finite element order provides significant gains in symmetry shown by the reduction in yellow regions and increase in blue regions. We corroborate these results by plotting the asymmetry values as a function of the spherical radius (i.e.,  $\rho = \sqrt{r^2 + z^2}$ ) in Figure 37. It is evident that increasing the finite element order provides gains in spherical symmetry. Moreover, Figure 38 demonstrates there is an increase in accuracy by increasing the finite element order except for 8<sup>th</sup>-order finite elements.

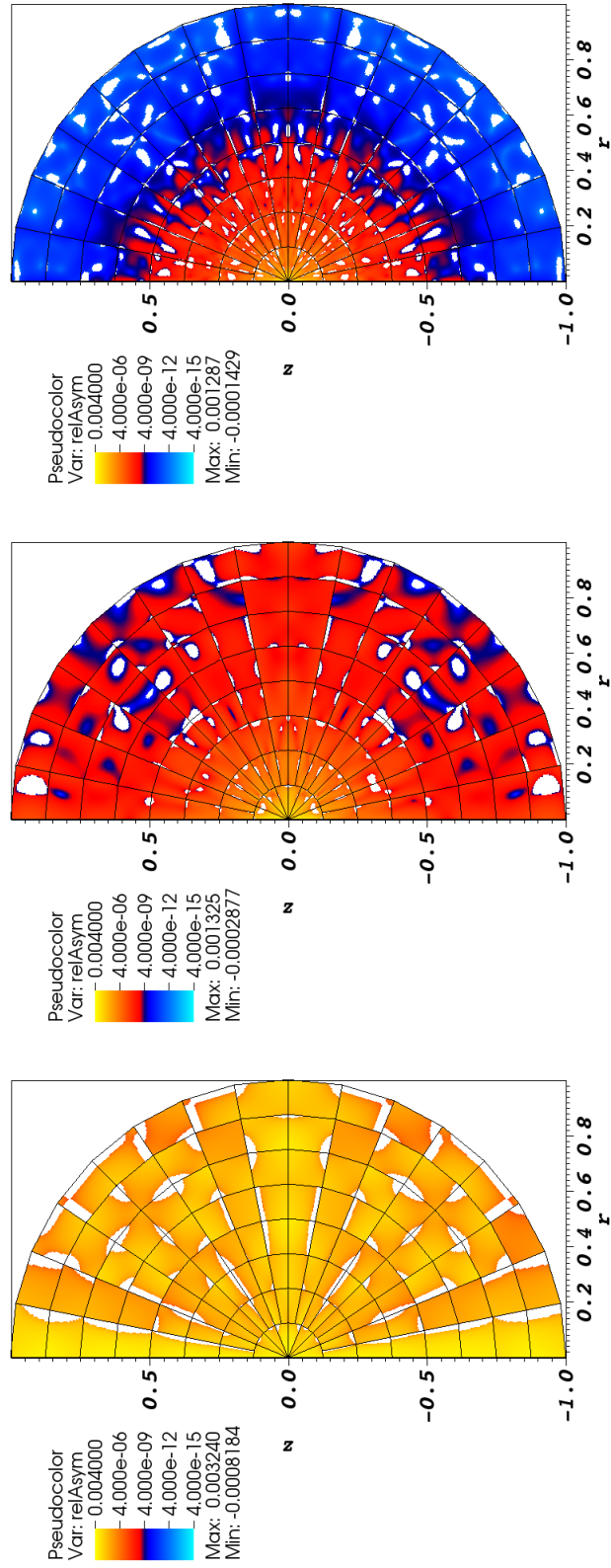


Figure 36: Relative asymmetry for  $p = \{1, 2, 4\}$  finite elements on a 1<sup>st</sup>-order mesh with 120 zones for  $S_8$  level-symmetric angular quadrature.

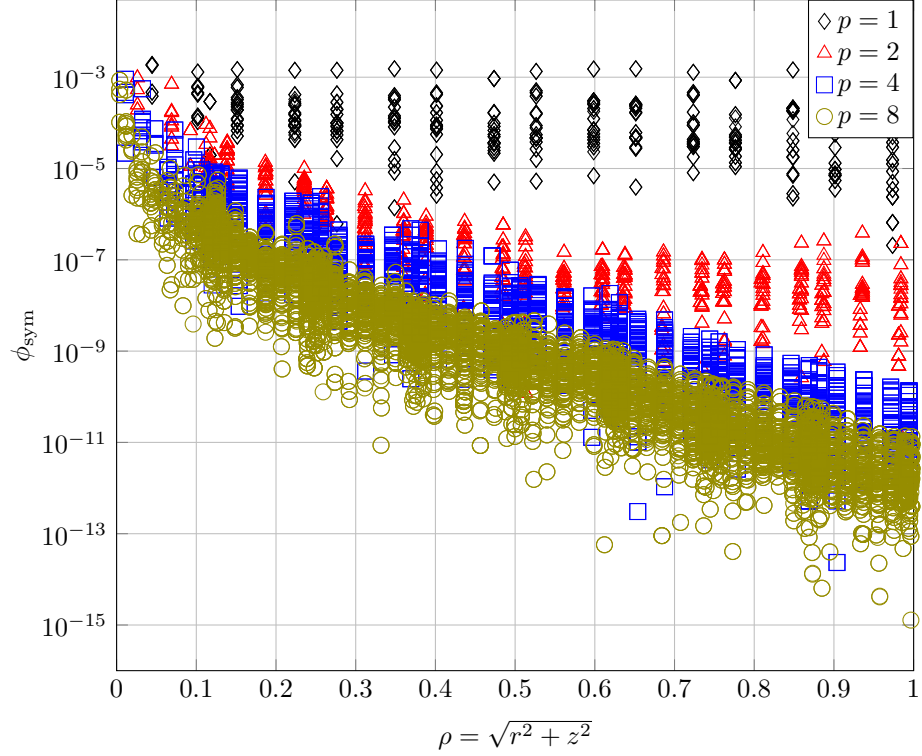


Figure 37: Measure of the asymmetry for each finite element node for the given finite element order using  $S_8$  level-symmetric angular quadrature on a 1<sup>st</sup>-order mesh with 120 zones (see Figure 36).

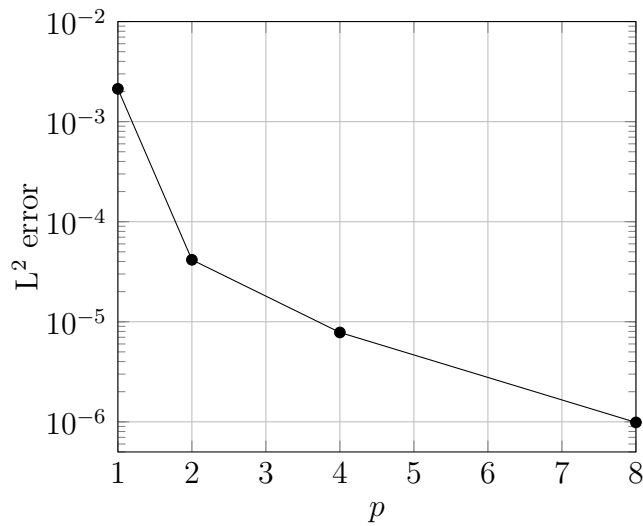


Figure 38: Accuracy of solutions for given finite element order using  $S_8$  level-symmetric angular quadrature on a 1<sup>st</sup>-order mesh with 120 zones.

We also investigated the symmetry preservation by performing sequential mesh refinements for  $p = 1$  with  $S_8$  level-symmetric angular quadrature. Figures 39 and 40 show the first several mesh refinement steps. The asymmetry is plotted on a log scale. The scale colors assist in demonstrating the qualitative locations of the asymmetries. The yellow region is the least symmetric, red regions have increased symmetry, and blue regions have the most symmetry. The  $\phi_{\text{sym}}$  solution is plotted using the same finite element shape functions as the scalar flux. There is some gain (a few orders of magnitude) in symmetry by refining the 1<sup>st</sup>-order mesh. We observe large regions of  $\phi_{\text{sym}}$  changing from yellow to red through the mesh refinement. Plotting the symmetry values as a function of the spherical radius (i.e.,  $\rho = \sqrt{r^2 + z^2}$ ) in Figure 41 shows that there is some symmetry gain by refining the mesh. The largest asymmetry magnitude of the scalar flux is near the polar axis (i.e.  $r = 0$ ) as previously seen in Figure 24. Moreover, Figure 42 demonstrates there is an increase in accuracy by refining the spatial mesh.

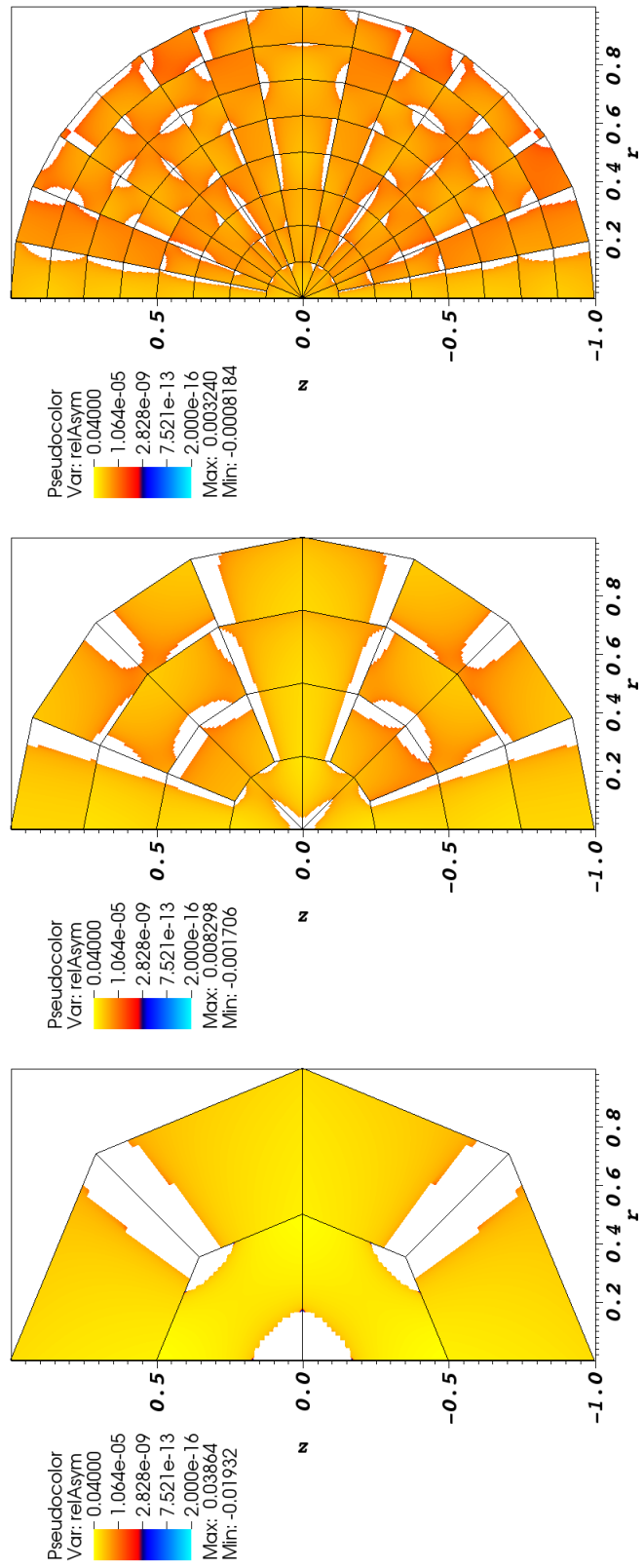


Figure 39: Relative asymmetry for  $p = 1$  finite elements on a 1<sup>st</sup>-order mesh for  $S_8$  level-symmetric angular quadrature for  $N_{\text{zones}} = \{6, 28, 120\}$ .

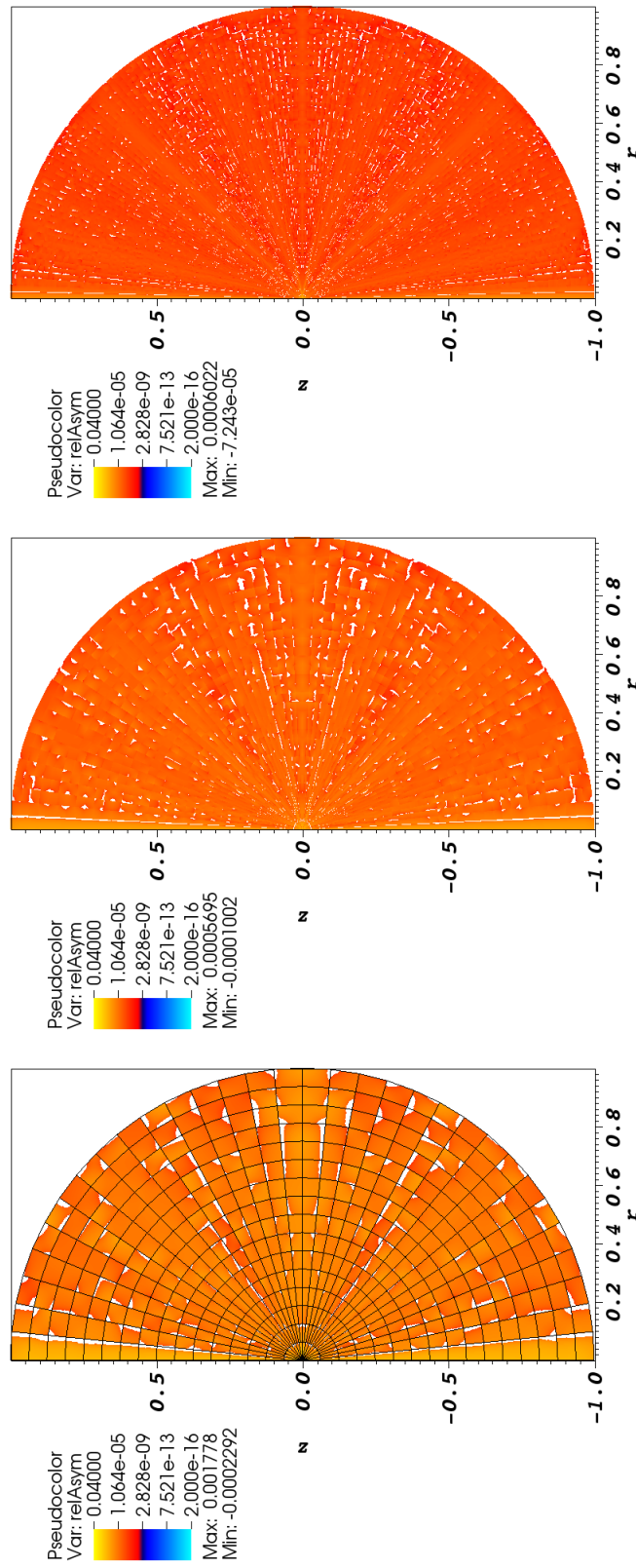


Figure 40: Relative asymmetry for  $p = 1$  finite elements on a 1<sup>st</sup>-order mesh for  $S_8$  level-symmetric angular quadrature for  $N_{\text{zones}} = \{496, 2016, 8128\}$ ; mesh overlay may be removed for clarity.

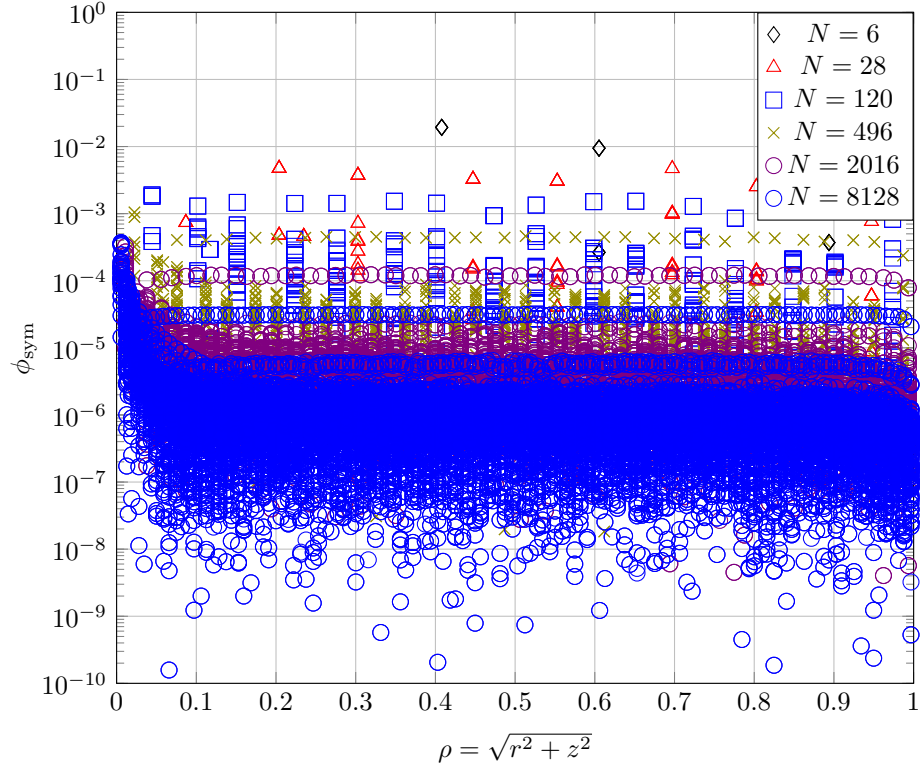


Figure 41: Measure of the asymmetry for each finite element node for 1<sup>th</sup>-order finite elements using  $S_8$  level-symmetric angular quadrature on a 1<sup>st</sup>-order mesh with various number of zones (see Figures 39-40).

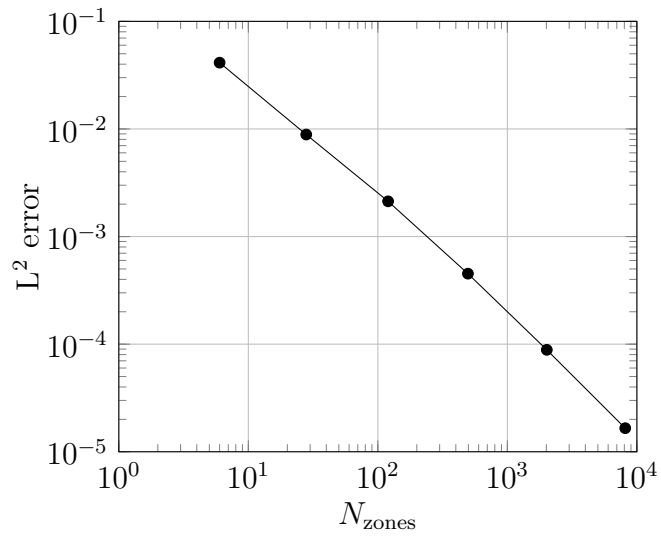


Figure 42: Accuracy of solutions for given mesh refinement for  $p = 1$  using  $S_8$  level-symmetric angular quadrature on a 1<sup>st</sup>-order mesh.

We also investigated the symmetry preservation by performing sequential mesh refinements for  $p = 4$  with  $S_8$  level-symmetric angular quadrature. Figures 43 and 44 show the first several mesh refinement steps. The asymmetry is plotted on a log scale. The scale colors assist in demonstrating the qualitative locations of the asymmetries. The yellow region is the least symmetric, red regions have increased symmetry, and blue regions have the most symmetry. The  $\phi_{\text{sym}}$  solution is plotted using the same finite element shape functions as the scalar flux. There is tremendous gain (many orders of magnitude) in symmetry by refining the 1<sup>st</sup>-order mesh. We observe large regions of  $\phi_{\text{sym}}$  changing from yellow to red to blue throughout the mesh refinement. Plotting the symmetry values as a function of the spherical radius (i.e.,  $\rho = \sqrt{r^2 + z^2}$ ) in Figure 45 confirms the substantial symmetry gain by refining the mesh. The largest asymmetry magnitude of the scalar flux remains near the origin (i.e.  $\rho = \sqrt{r^2 + z^2} = 0$ ) as previously seen, but also remains prevalent in the discrete ordinates directions as though there were ray effects. Moreover, Figure 46 demonstrates there is an increase in accuracy by refining the spatial mesh.

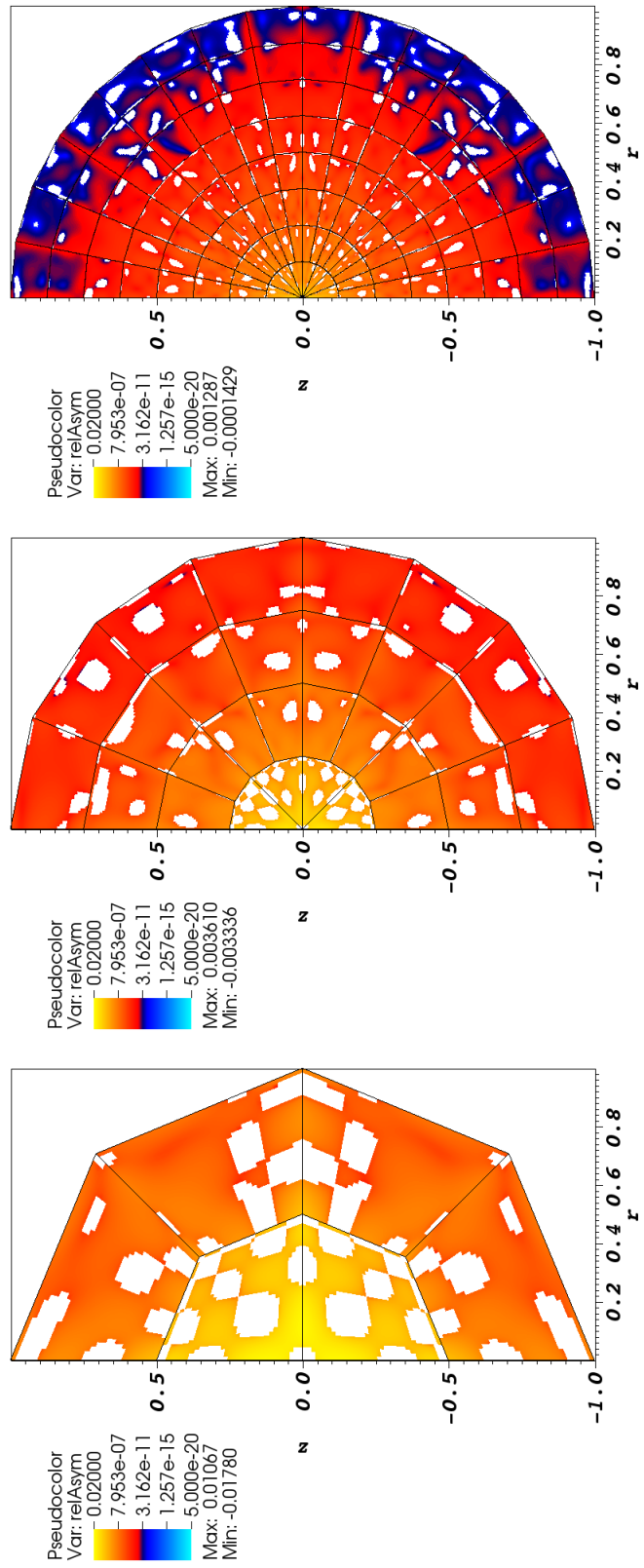
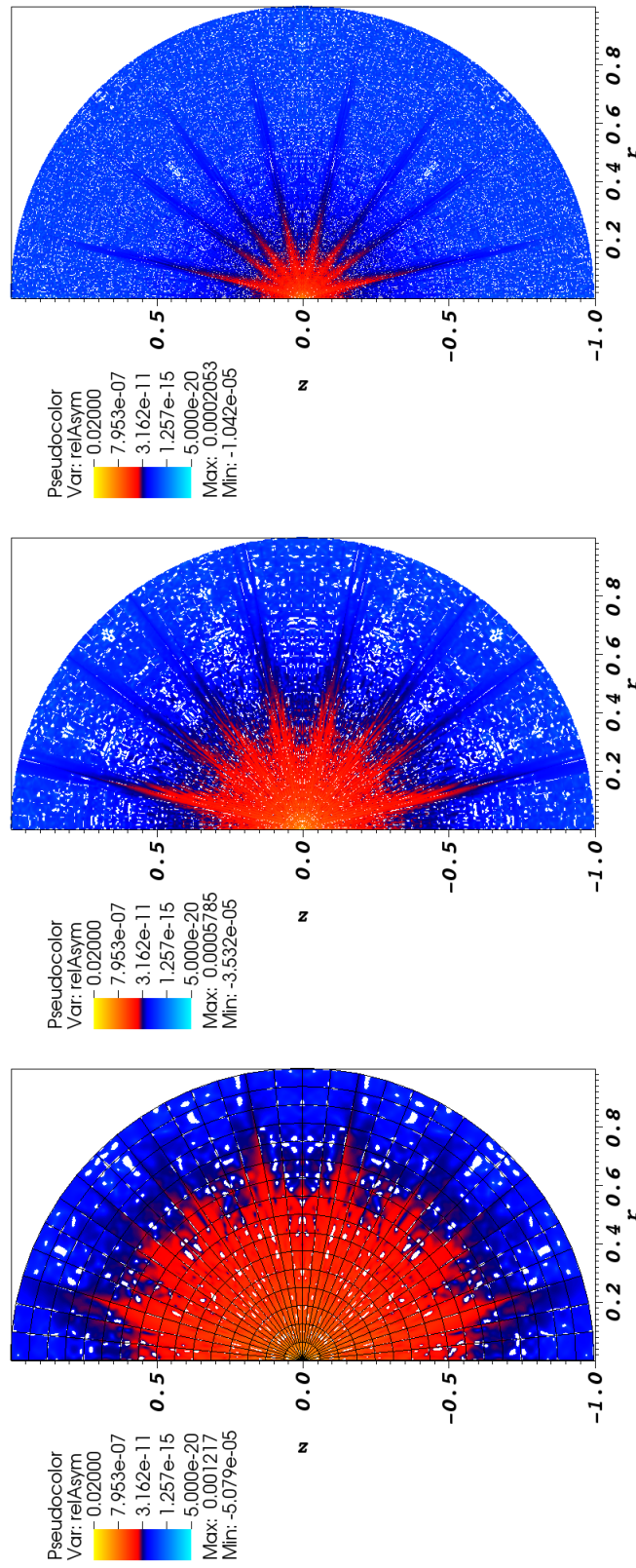


Figure 43: Relative asymmetry for  $p = 4$  finite elements on a 1<sup>st</sup>-order mesh for  $S_8$  level-symmetric angular quadrature for  $N_{\text{zones}} = \{6, 28, 120\}$ .



(a)  $N_{\text{zones}} = 496$ .  
 (b)  $N_{\text{zones}} = 2016$ .  
 (c)  $N_{\text{zones}} = 8128$ .

Figure 44: Relative asymmetry for  $p = 4$  finite elements on a 1<sup>st</sup>-order mesh for  $S_8$  level-symmetric angular quadrature for  $N_{\text{zones}} = \{496, 2016, 8128\}$ ; mesh overlay may be removed for clarity.

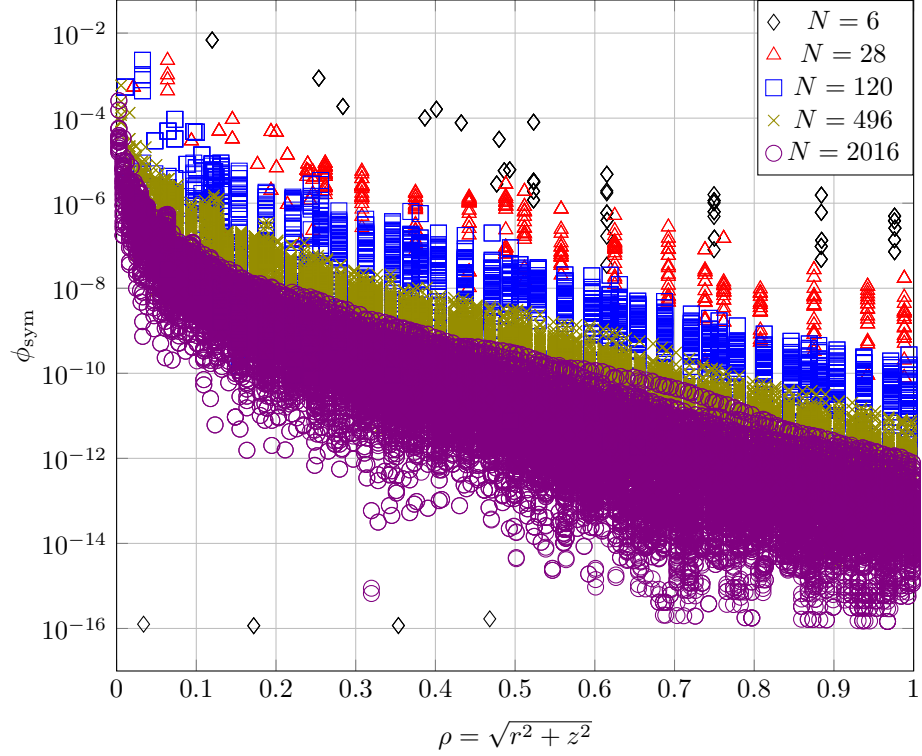


Figure 45: Measure of the asymmetry for each finite element node for 4<sup>th</sup>-order finite elements using  $S_8$  level-symmetric angular quadrature on a 1<sup>st</sup>-order mesh with various number of zones (see Figures 43-44).

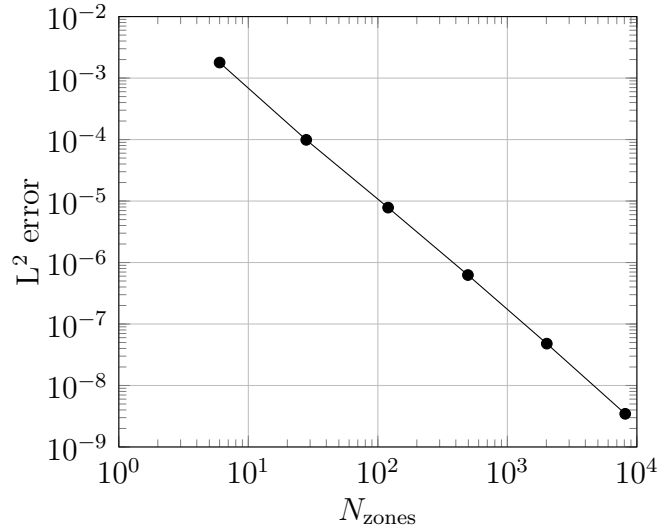


Figure 46: Accuracy of solutions for given mesh refinement for  $p = 4$  using  $S_8$  level-symmetric angular quadrature on a 1<sup>st</sup>-order mesh.

#### 4.4.2 High-Order Mesh

Now, we perform the same asymmetry analysis using a high-order mesh. In this section, we observe the sensitivity of the scalar flux spherical asymmetry to changing the discrete ordinates order, finite element order, and spatial refinement on a high-order mesh. A high-order mesh is one that has curved polynomial surfaces. Specifically, we use 2<sup>nd</sup>-order meshes here. The vertices of the 2<sup>nd</sup>-order meshes used in this section are located in concentric rings of equal  $\rho = \sqrt{r^2 + z^2}$ , including the midpoint vertices. The results in this section are organized as follows: comparing the discrete ordinates order for each of  $p = \{1, 2, 4\}$ , comparing each of  $p = \{1, 2, 4\}$  for  $S_8$  level symmetric angular quadrature, mesh refinement studies for each of  $p = \{1, 4\}$ , and comparing the discrete ordinates refinement on the most refined spatial mesh.

Figure 47 shows the  $\phi_{\text{sym}}$  values calculated using Equation 80 for 1<sup>st</sup>-order finite elements on a 2<sup>nd</sup>-order mesh with 120 zones for several angular quadrature discretizations. The asymmetry is plotted on a log scale. The scale colors assist in demonstrating the qualitative locations of the asymmetries. The yellow region is the least symmetric, red regions have increased symmetry, and blue regions have the most symmetry. The  $\phi_{\text{sym}}$  solution is plotted using the same finite element shape functions as the scalar flux. There is no perceptible gain in symmetry by increasing the angular discretization order. We confirm this by plotting the asymmetry values as a function of the spherical radius (i.e.,  $\rho = \sqrt{r^2 + z^2}$ ) in Figure 48. The spherical radial asymmetry solutions are indistinguishable between discrete ordinate orders. Moreover, Figure 49 demonstrates there is no increase in accuracy by increasing the  $S_N$  order.

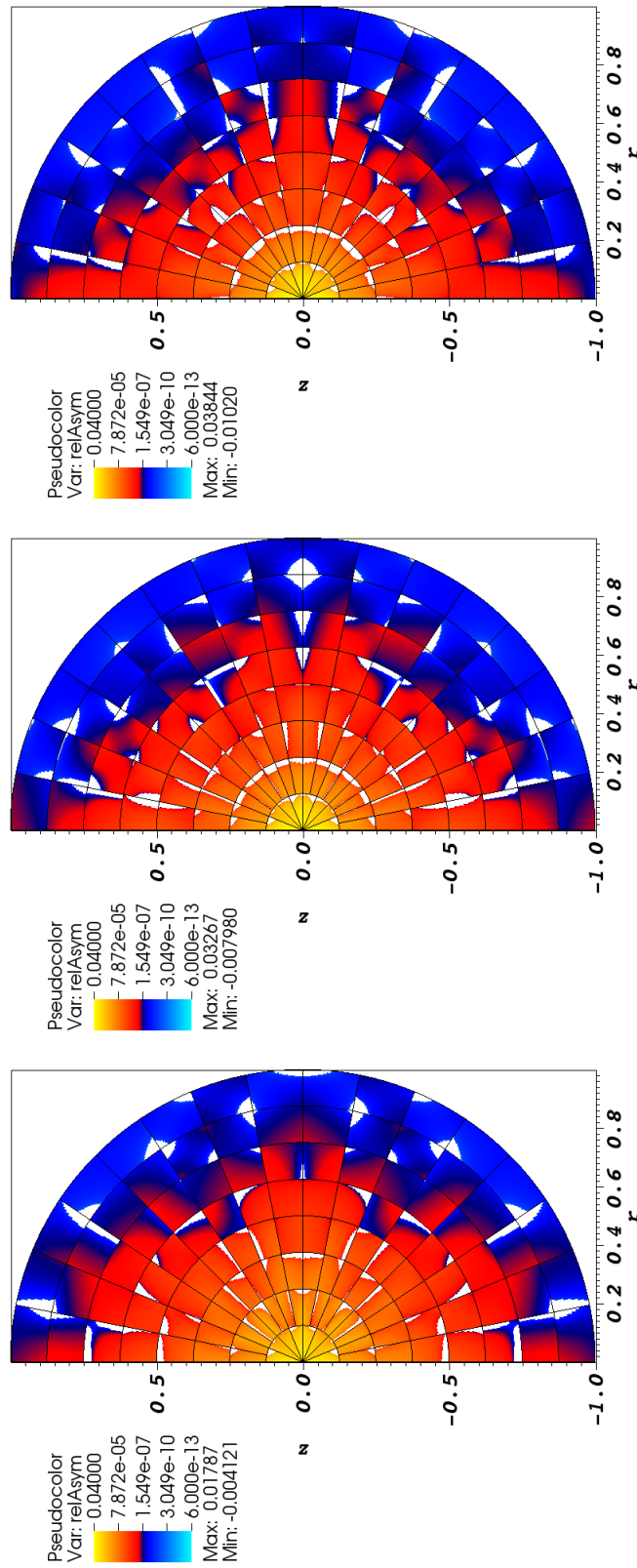


Figure 47: Relative asymmetry for 1<sup>st</sup>-order finite elements on a 2<sup>nd</sup>-order mesh for given order of level-symmetric angular quadrature.

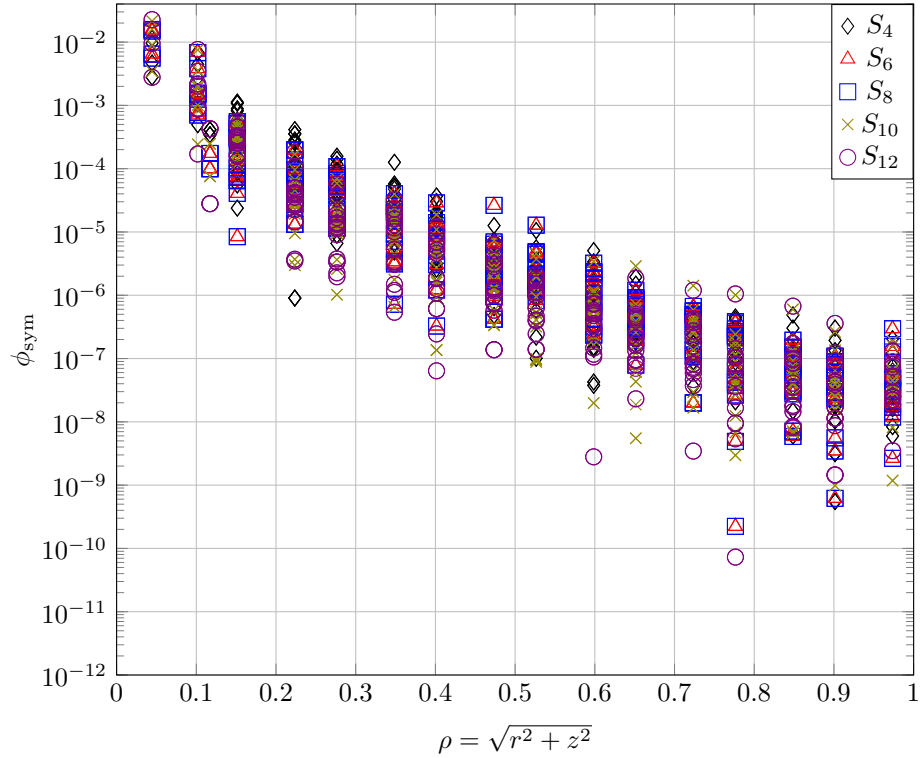


Figure 48: Measure of the asymmetry for each finite element node for the given level-symmetric angular quadrature order for 1<sup>st</sup>-order DFEM and 2<sup>nd</sup>-order mesh with 120 zones (see Figure 47).

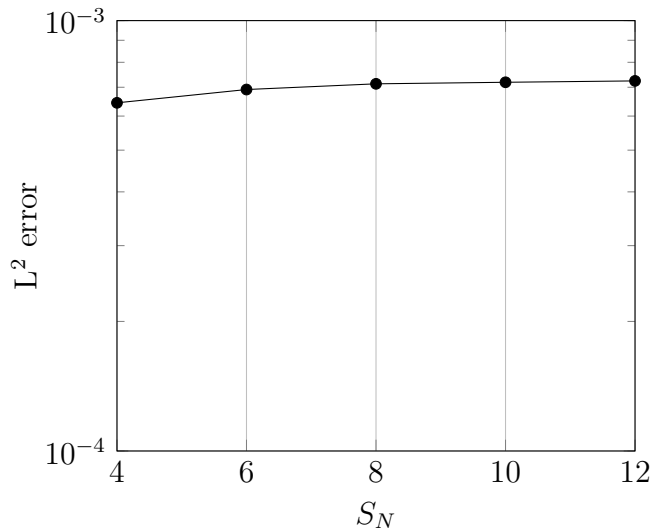


Figure 49: Accuracy of solutions for given angular quadrature using  $p = 1$  on a 2<sup>nd</sup>-order mesh with 120 zones.

Figure 50 shows the  $\phi_{\text{sym}}$  values calculated using Equation 80 for 2<sup>nd</sup>-order finite elements on a 2<sup>nd</sup>-order mesh with 120 zones for several angular quadrature discretizations. The asymmetry is plotted on a log scale. The scale colors assist in demonstrating the qualitative locations of the asymmetries. The yellow region is the least symmetric, red regions have increased symmetry, and blue regions have the most symmetry. The  $\phi_{\text{sym}}$  solution is plotted using the same finite element shape functions as the scalar flux. There is very little perceptible gain in symmetry near the equator (i.e.,  $z = 0$ ) by increasing the angular discretization order. However, plotting the asymmetry values as a function of the spherical radius (i.e.,  $\rho = \sqrt{r^2 + z^2}$ ) in Figure 51 shows that there may not actually be any symmetry gains — the spherical radial asymmetry solutions are indistinguishable between discrete ordinate orders. The asymmetries are predominantly located near the polar axis (i.e.,  $r = 0$ ). Moreover, Figure 52 demonstrates there is no increase in accuracy by increasing the  $S_N$  order.

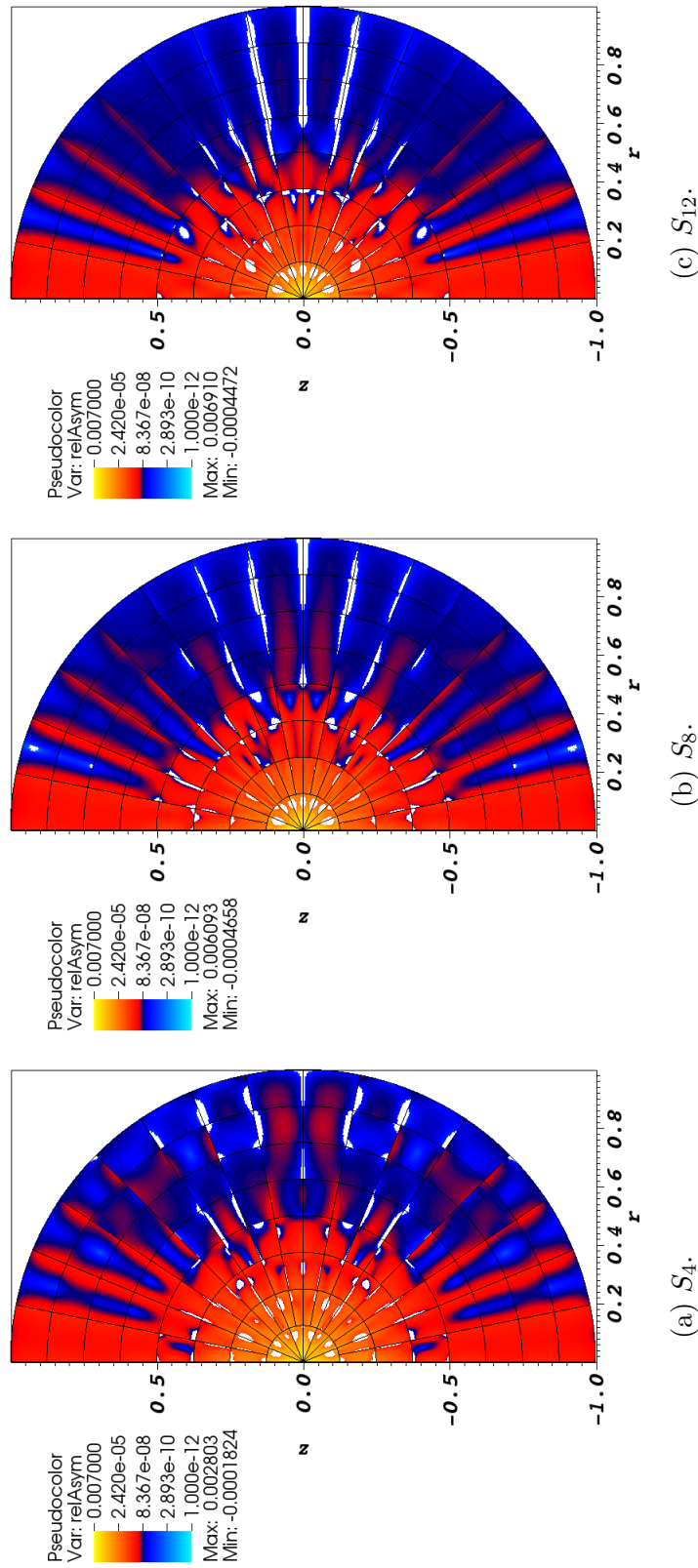


Figure 50: Relative asymmetry for 2<sup>nd</sup>-order finite elements on a 2<sup>nd</sup>-order mesh for given order of level-symmetric angular quadrature.

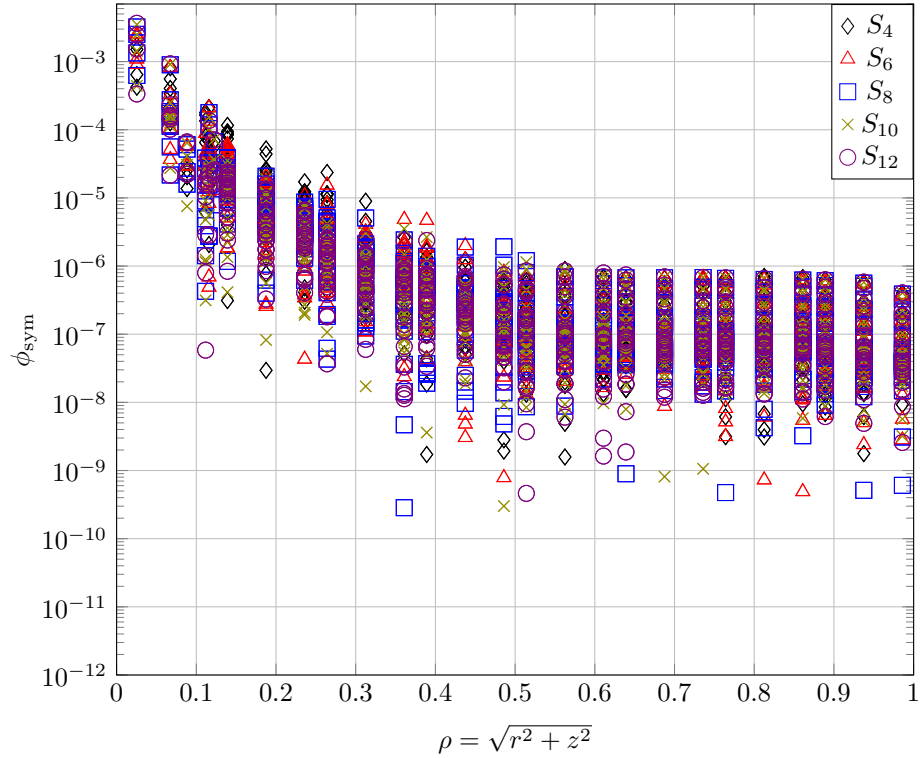


Figure 51: Measure of the asymmetry for each finite element node for the given level-symmetric angular quadrature order for 2<sup>nd</sup>-order DFEM and 2<sup>nd</sup>-order mesh with 120 zones (see Figure 50).

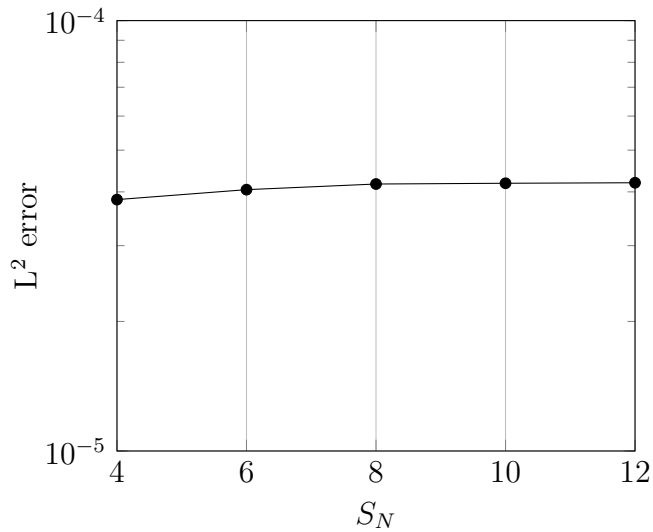


Figure 52: Accuracy of solutions for given angular quadrature using  $p = 2$  on a 2<sup>nd</sup>-order mesh with 120 zones.

Figure 53 shows the  $\phi_{\text{sym}}$  values calculated using Equation 80 for 4<sup>th</sup>-order finite elements on a 2<sup>nd</sup>-order mesh with 120 zones for several angular quadrature discretizations. The asymmetry is plotted on a log scale. The scale colors assist in demonstrating the qualitative locations of the asymmetries. The yellow region is the least symmetric, red regions have increased symmetry, and blue regions have the most symmetry. The  $\phi_{\text{sym}}$  solution is plotted using the same finite element shape functions as the scalar flux. There is no perceptible gain in symmetry by increasing the angular discretization order. However, plotting the asymmetry values as a function of the spherical radius (i.e.,  $\rho = \sqrt{r^2 + z^2}$ ) in Figure 54 shows that there may be a symmetry gain from  $S_4$  to higher angular discretization orders for  $\rho \geq 0.7$ . Unlike Figure 50, the asymmetry of the scalar flux appears to be a function of the spherical radius,  $\rho$ . Moreover, Figure 55 demonstrates there is no increase in accuracy by increasing the  $S_N$  order.

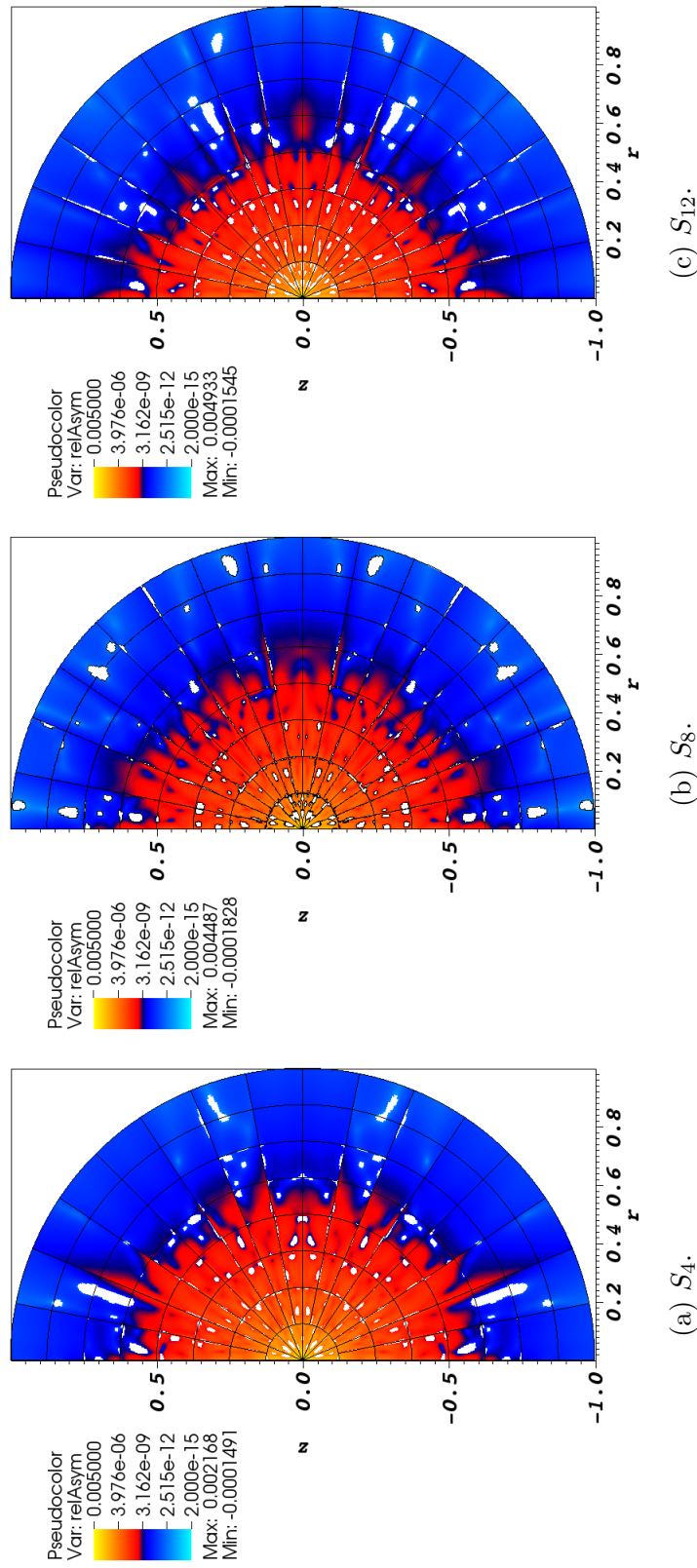


Figure 53: Relative asymmetry for 4<sup>th</sup>-order finite elements on a 2<sup>nd</sup>-order mesh for given order of level-symmetric angular quadrature.

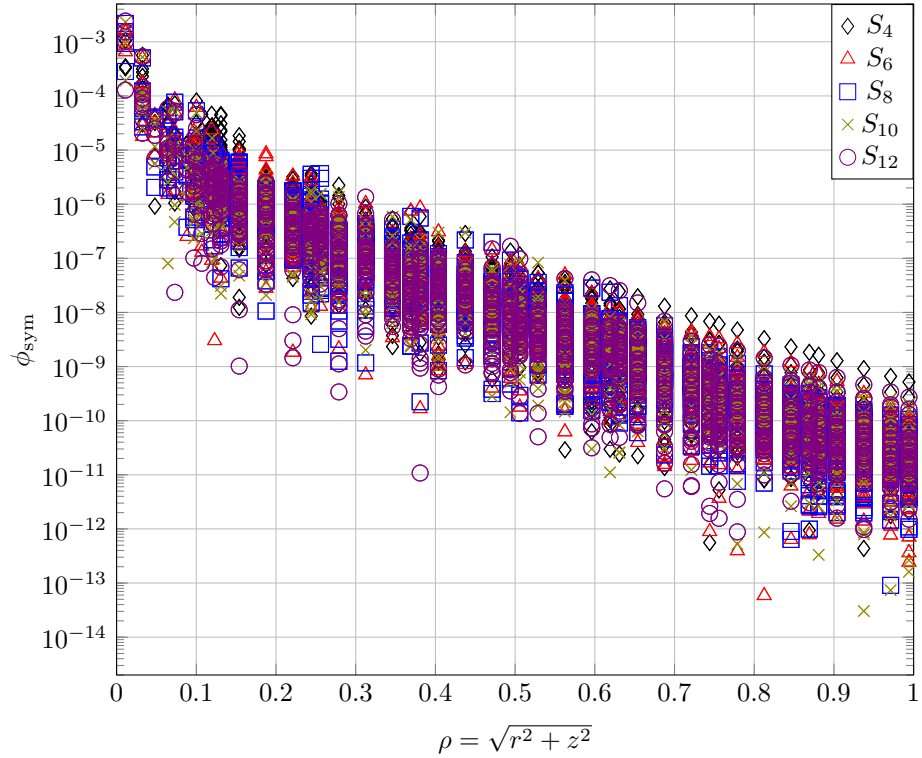


Figure 54: Measure of the asymmetry for each finite element node for the given level-symmetric angular quadrature order for 4<sup>th</sup>-order DFEM and 2<sup>nd</sup>-order mesh with 120 zones (see Figure 53).

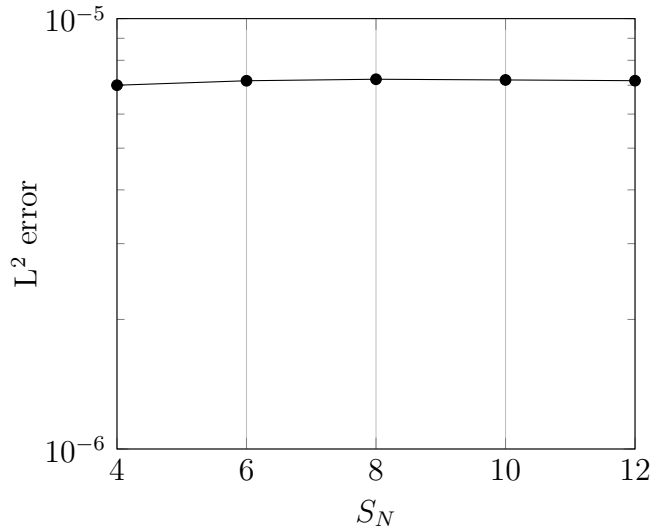


Figure 55: Accuracy of solutions for given angular quadrature using  $p = 4$  on a 2<sup>nd</sup>-order mesh with 120 zones.

Figure 56 shows the  $\phi_{\text{sym}}$  values calculated using Equation 80 for  $p = \{1, 2, 4\}$  finite elements on a 2<sup>nd</sup>-order mesh with 120 zones with  $S_8$  level-symmetric angular quadrature repeated from Figures 47, 50, 53 and plotted on the same scale. Increasing the finite element order from  $p = 1$  to  $p = 2$  increases the symmetry near the origin slightly, indicated by a reduction in yellow. However, increasing the finite element order to  $p = 4$  provides significant gains in symmetry shown by the relatively larger blue region for  $\rho = \sqrt{r^2 + z^2} \geq 0.5$ . We corroborate these results by plotting the asymmetry values as a function of the spherical radius (i.e.,  $\rho = \sqrt{r^2 + z^2}$ ) in Figure 57. It is evident that increasing the finite element order provides gains in spherical symmetry. Moreover, Figure 58 demonstrates there is an increase in accuracy by increasing the finite element order.

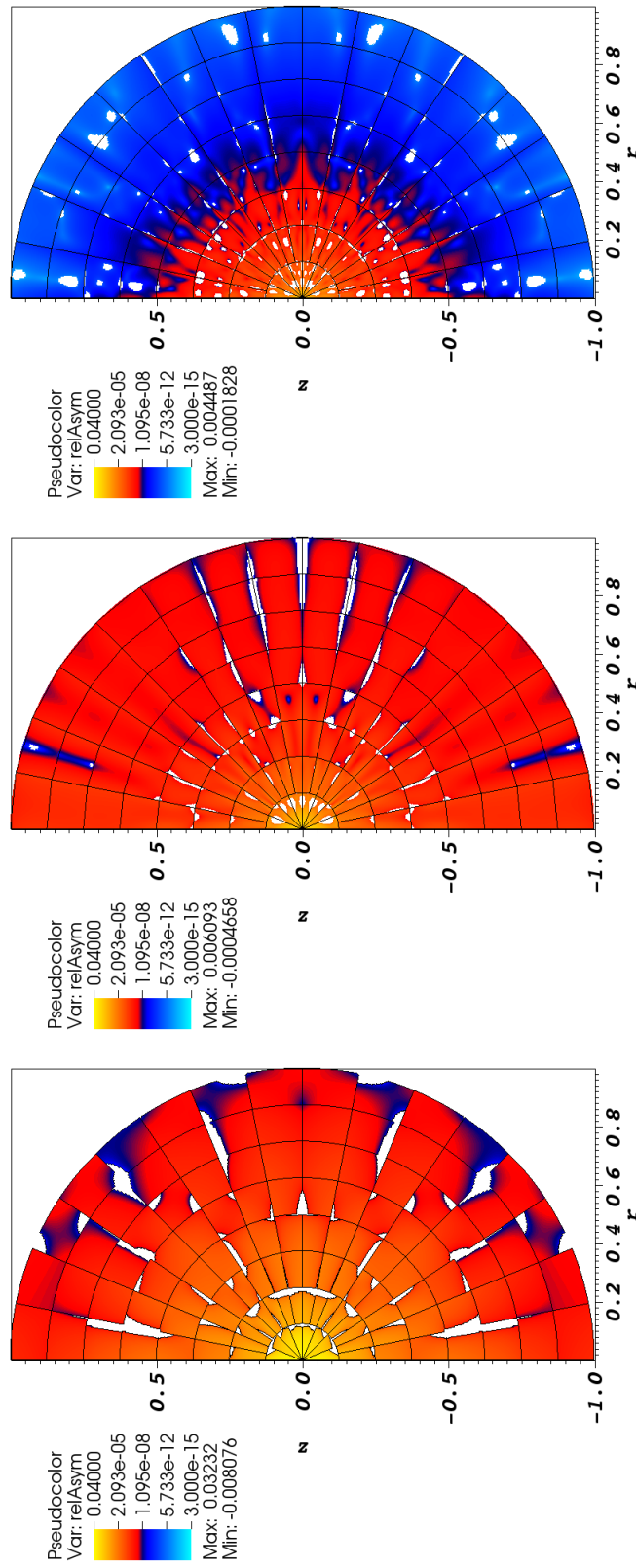


Figure 56: Relative asymmetry for  $p = \{1, 2, 4\}$  finite elements on a 2<sup>nd</sup>-order mesh for  $S_8$  level-symmetric angular quadrature.

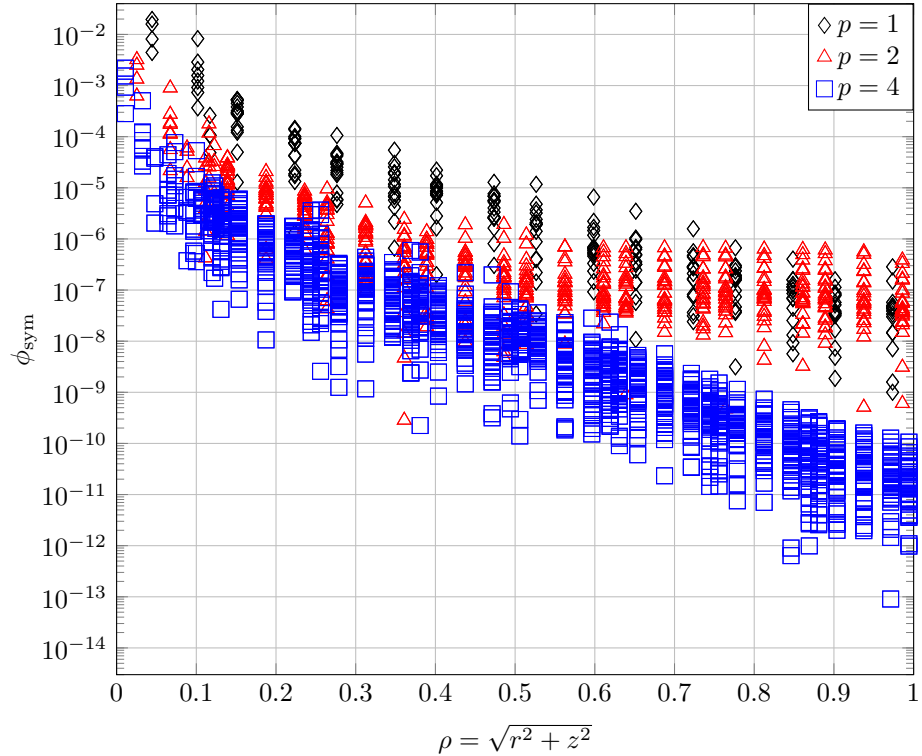


Figure 57: Measure of the asymmetry for each finite element node for the given finite element order using  $S_8$  level-symmetric angular quadrature on a 2<sup>nd</sup>-order mesh with 120 zones (see Figure 56).

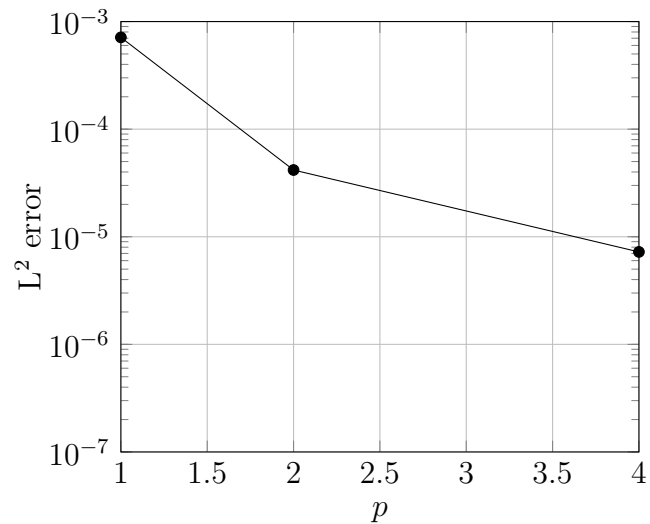


Figure 58: Accuracy of solutions for given angular quadrature using  $S_8$  level-symmetric angular quadrature on a 2<sup>nd</sup>-order mesh with 120 zones.

We investigated the symmetry preservation by performing sequential mesh refinements for  $p = 1$  with  $S_8$  level-symmetric angular quadrature. Figures 59 and 60 show the first several mesh refinement steps. The asymmetry is plotted on a log scale. The scale colors assist in demonstrating the qualitative locations of the asymmetries. The yellow region is the least symmetric, red regions have increased symmetry, and blue regions have the most symmetry. The  $\phi_{\text{sym}}$  solution is plotted using the same finite element shape functions as the scalar flux. As on the 1<sup>st</sup>-order mesh, there is tremendous gain (many orders of magnitude) in symmetry by refining the 2<sup>nd</sup>-order mesh. We observe large regions of  $\phi_{\text{sym}}$  changing from yellow to red to blue throughout the mesh refinement. Plotting the symmetry values as a function of the spherical radius (i.e.,  $\rho = \sqrt{r^2 + z^2}$ ) in Figure 61 confirms the substantial symmetry gain by refining the mesh. The largest asymmetry magnitude of the scalar flux remains near the origin (i.e.  $\rho = \sqrt{r^2 + z^2} = 0$ ) as previously seen, but also remains prevalent in the discrete ordinates directions as though there were ray effects. Moreover, Figure 62 demonstrates there is an increase in accuracy by refining the spatial mesh.

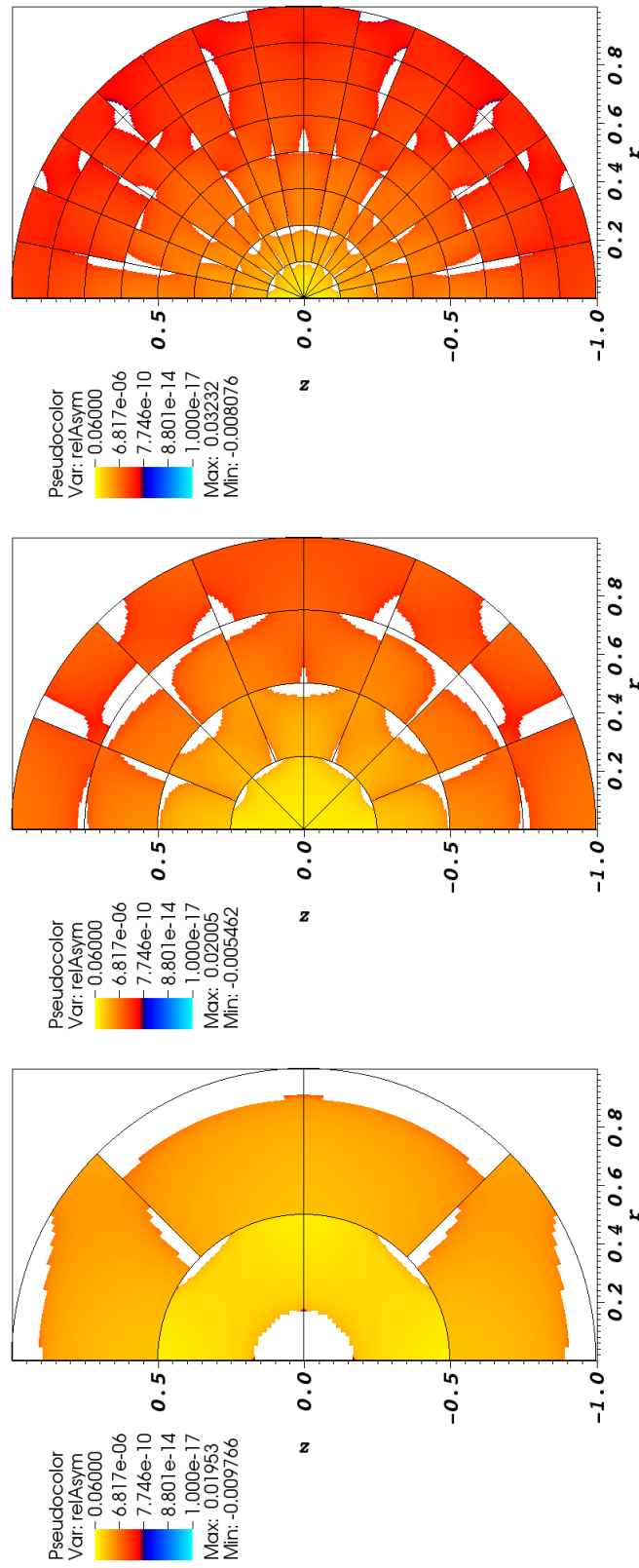


Figure 59: Relative asymmetry for  $p = 1$  finite elements on a 2<sup>nd</sup>-order mesh for  $S_8$  level-symmetric angular quadrature.

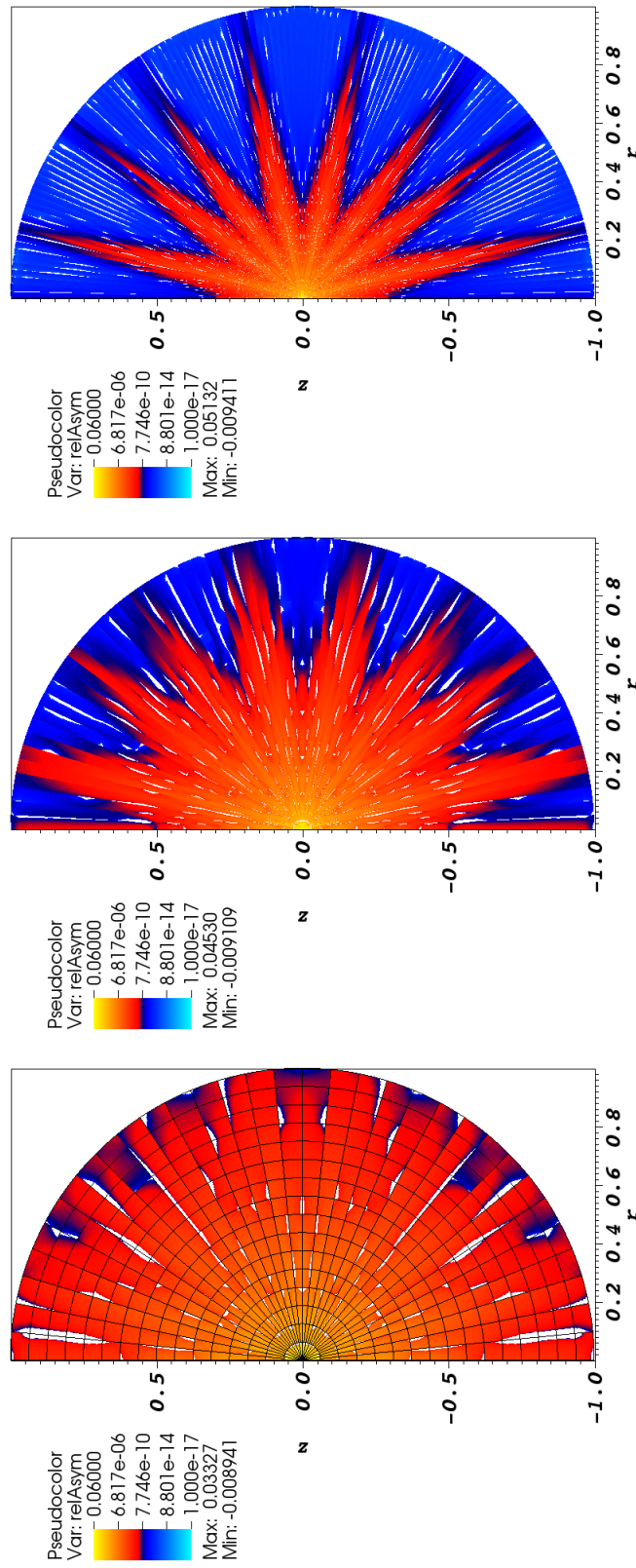


Figure 60: Relative asymmetry for  $p = 1$  finite elements on a 2<sup>nd</sup>-order mesh for  $S_8$  level-symmetric angular quadrature; mesh overlay may be removed for clarity.

Figure 61: Measure of the asymmetry for each finite element node for 1<sup>st</sup>-order finite elements using  $S_8$  level-symmetric angular quadrature on a 2<sup>nd</sup>-order mesh with various number of zones (see Figures 59-60).

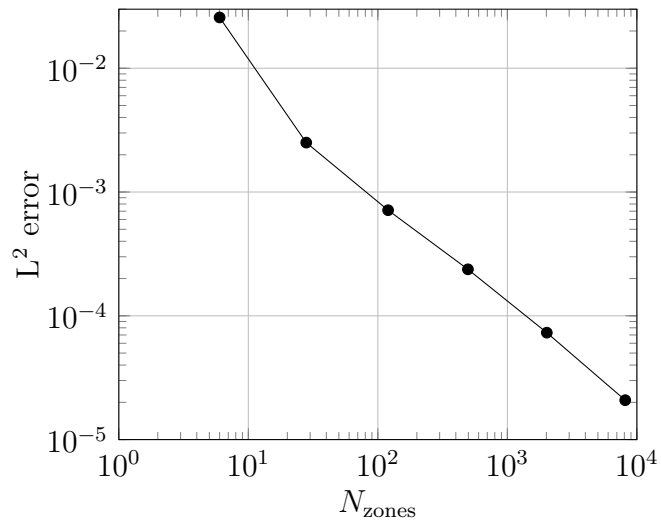


Figure 62: Accuracy of solutions for mesh refinement study using  $p = 1$ ,  $S_8$  level-symmetric angular quadrature, on a 2<sup>nd</sup>-order mesh.

We also investigated the symmetry preservation by performing sequential mesh refinements for  $p = 1$  with  $S_8$  level-symmetric angular quadrature. Figures 63 and 64 show the first several mesh refinement steps. The asymmetry is plotted on a log scale. The scale colors assist in demonstrating the qualitative locations of the asymmetries. The yellow region is the least symmetric, red regions have increased symmetry, and blue regions have the most symmetry. The  $\phi_{\text{sym}}$  solution is plotted using the same finite element shape functions as the scalar flux. As on the 1<sup>st</sup>-order mesh, there is tremendous gain (many orders of magnitude) in symmetry by refining the 2<sup>nd</sup>-order mesh. We observe large regions of  $\phi_{\text{sym}}$  changing from yellow to red to blue throughout the mesh refinement. Plotting the symmetry values as a function of the spherical radius (i.e.,  $\rho = \sqrt{r^2 + z^2}$ ) in Figure 65 confirms the substantial symmetry gain by refining the mesh. The largest asymmetry magnitude of the scalar flux remains near the origin (i.e.  $\rho = \sqrt{r^2 + z^2} = 0$ ) as previously seen, but also remains prevalent in the discrete ordinates directions as though there were ray effects. Moreover, Figure 66 demonstrates there is an increase in accuracy by refining the spatial mesh.

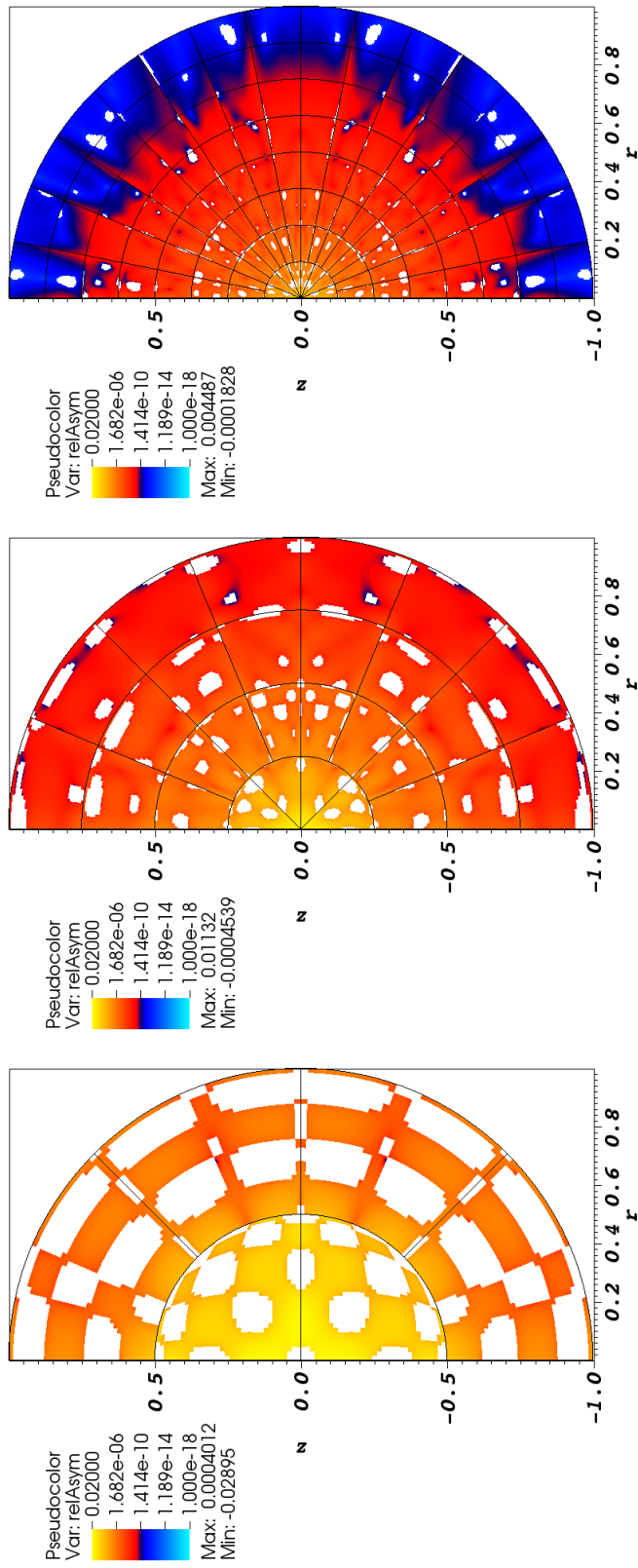


Figure 63: Relative asymmetry for  $p = 4$  finite elements on a 2<sup>nd</sup>-order mesh for  $S_8$  level-symmetric angular quadrature.

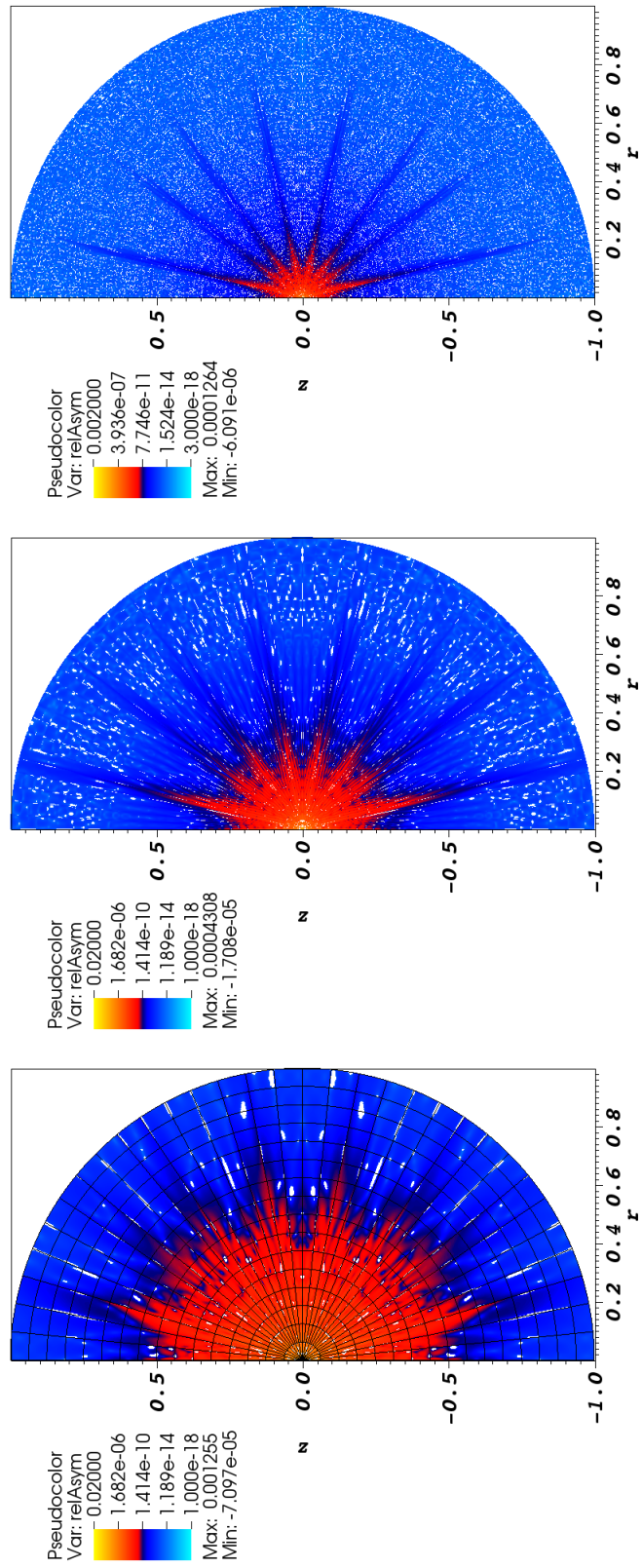


Figure 64: Relative asymmetry for  $p = 4$  finite elements on a 2<sup>nd</sup>-order mesh for  $S_8$  level-symmetric angular quadrature; mesh overlay may be removed for clarity.

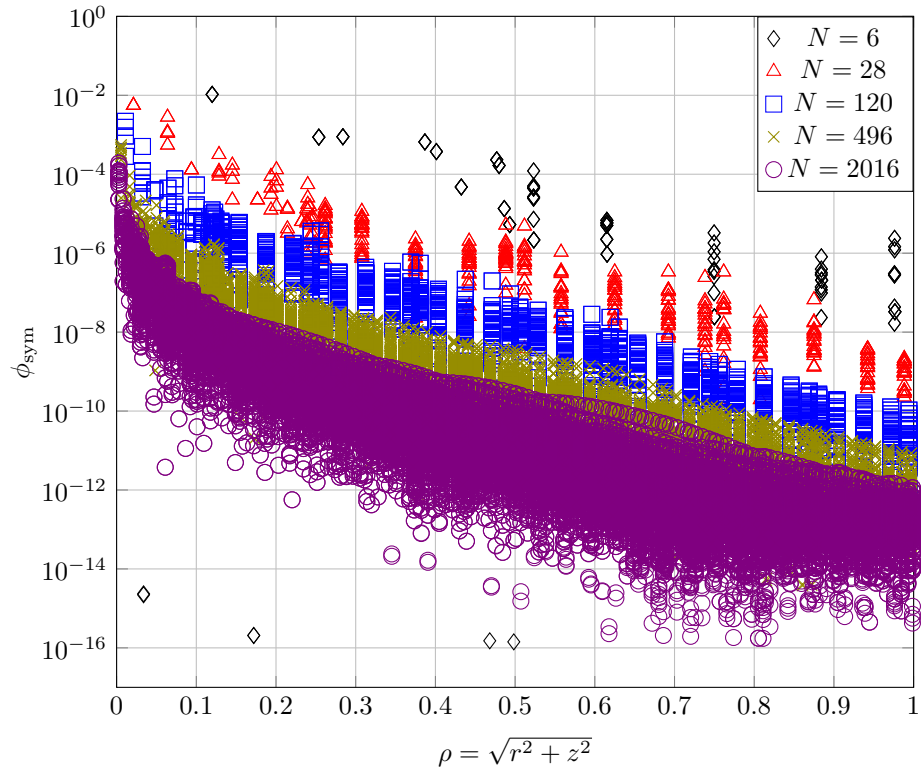


Figure 65: Measure of the asymmetry for each finite element node for 4<sup>th</sup>-order DFEM,  $S_8$  level-symmetric angular quadrature, and 2<sup>nd</sup>-order mesh with various number of zones (see Figures 63 - 64).

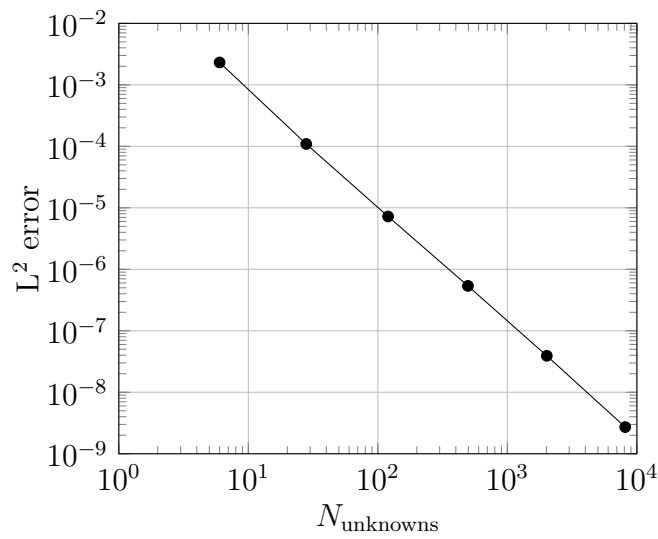


Figure 66: Accuracy of solutions for mesh refinement study using  $p = 4$ ,  $S_8$  level-symmetric angular quadrature, on a 2<sup>nd</sup>-order mesh.

In the most refined case of Figures 60 and 64, we observe some ray effects. These effects are dependent on the discrete ordinates discretization order. Here, we investigate the symmetry preservation by performing sequential discrete ordinates refinements for  $p = 1$  on a 2<sup>nd</sup>-order mesh with 8128 zones. Figure 67 show the first several mesh refinement steps. The asymmetry is plotted on a log scale. The scale colors assist in demonstrating the qualitative locations of the asymmetries. The yellow region is the least symmetric, red regions have increased symmetry, and blue regions have the most symmetry. The  $\phi_{\text{sym}}$  solution is plotted using the same finite element shape functions as the scalar flux. The ray effects are dependent upon the discrete ordinates discretization order. Despite the appearance of a reduction in overall symmetry, plotting the symmetry values as a function of the spherical radius (i.e.,  $\rho = \sqrt{r^2 + z^2}$ ) in Figure 65 demonstrates that the overall asymmetry is not very dependent upon the discrete ordinates discretization. The locations of these ray effects may introduce asymmetries themselves when coupling to other physics.

We also plot the asymmetry values as a function of the spherical radius (i.e.,  $\rho = \sqrt{r^2 + z^2}$ ). Figure 68 shows the  $\phi_{\text{sym}}$  values calculated using Equation 80 for 1<sup>st</sup>-order finite elements on a 2<sup>nd</sup>-order mesh with 8128 zones for several angular quadrature discretizations. Moreover, Figure 69 demonstrates there is no increase in accuracy by increasing the  $S_N$  order.

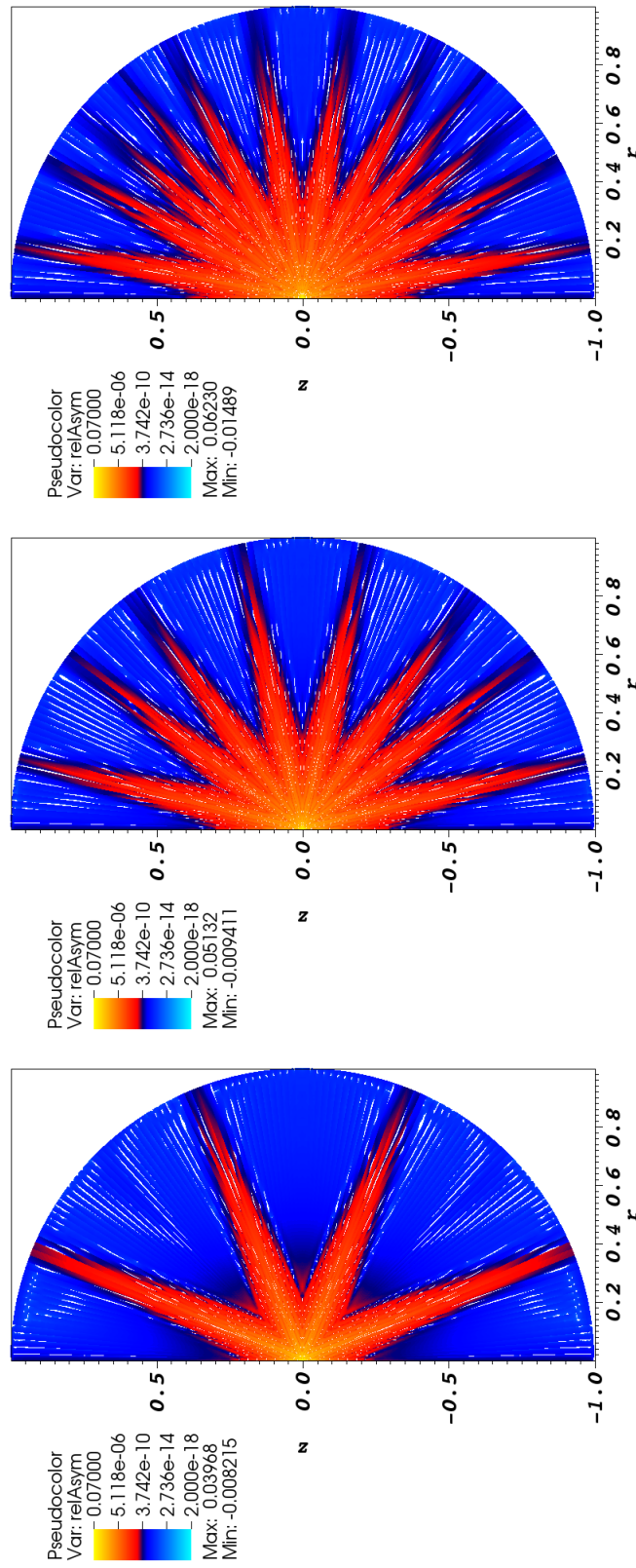


Figure 67: Relative asymmetry for  $p = 1$  finite elements on a 2nd-order mesh with 8128 zones; mesh overlay may be removed for clarity.

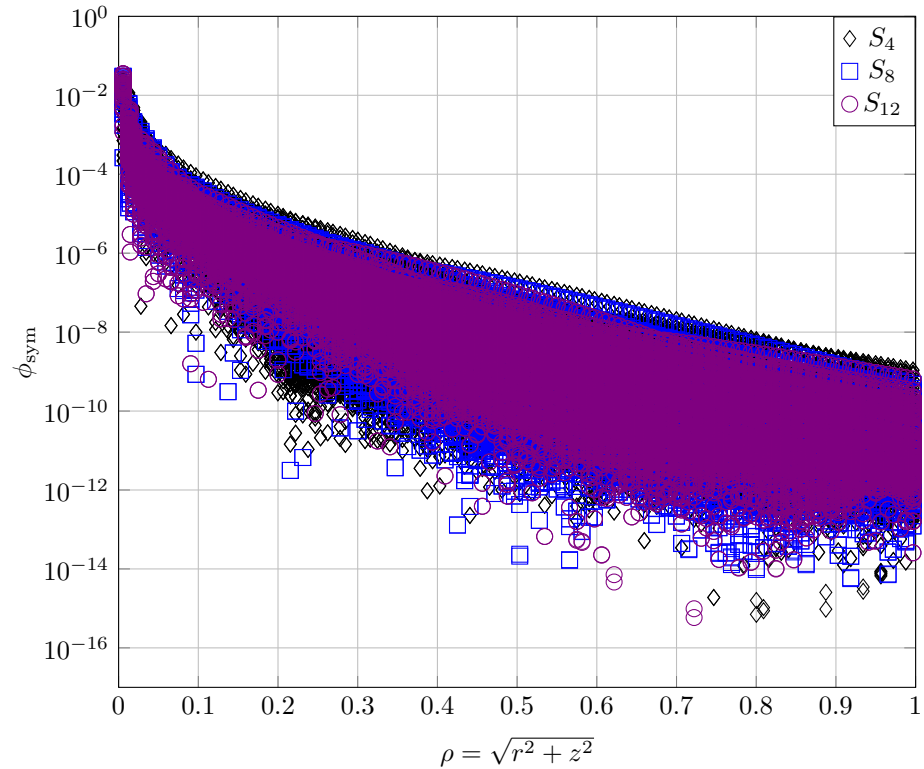


Figure 68: Measure of the asymmetry for each finite element node for the given level-symmetric angular quadrature order for 1<sup>st</sup>-order DFEM and 2<sup>nd</sup>-order mesh with 8128 zones.

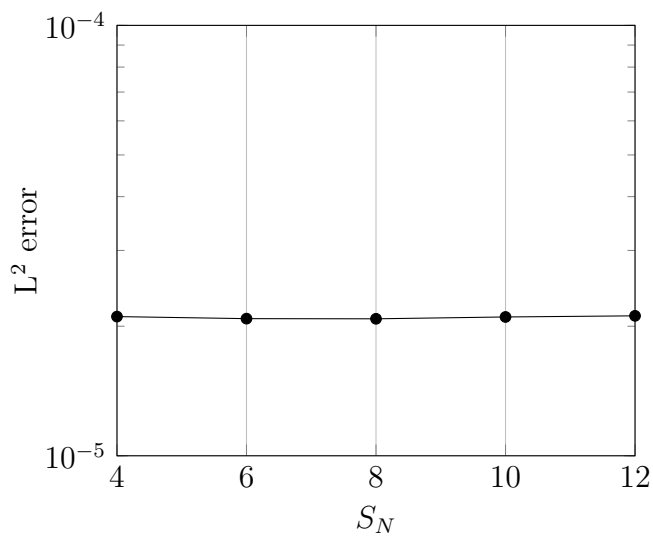


Figure 69: Accuracy of solutions for given angular quadrature using  $p = 4$  on a 2<sup>nd</sup>-order mesh with 8128 zones.

#### 4.4.3 Axisymmetry Summary and Discussion

For completeness, we compare some of the nodal asymmetry plots for ease of comparing the 2<sup>nd</sup>-order mesh to the 1<sup>st</sup>-order mesh on the same scales.

Figure 70 compares the 1<sup>st</sup>-order finite element solutions on both 1<sup>st</sup>- and 2<sup>nd</sup>-order meshes. While we have observed that the  $S_N$  order does not provide any additional accuracy or spherical symmetry, increasing the mesh order for 1<sup>st</sup>-order finite elements does increase the spherical symmetry with increasing  $\rho$ . However, Figure 71 demonstrates that the mesh curvature does not benefit the spherical symmetry with HO (4<sup>th</sup>-order) finite elements. Finally, Figure 72 illustrates that refining the mesh does increase the symmetry preservation for 4<sup>th</sup>-order finite elements but adding curvature to the mesh zones does not.

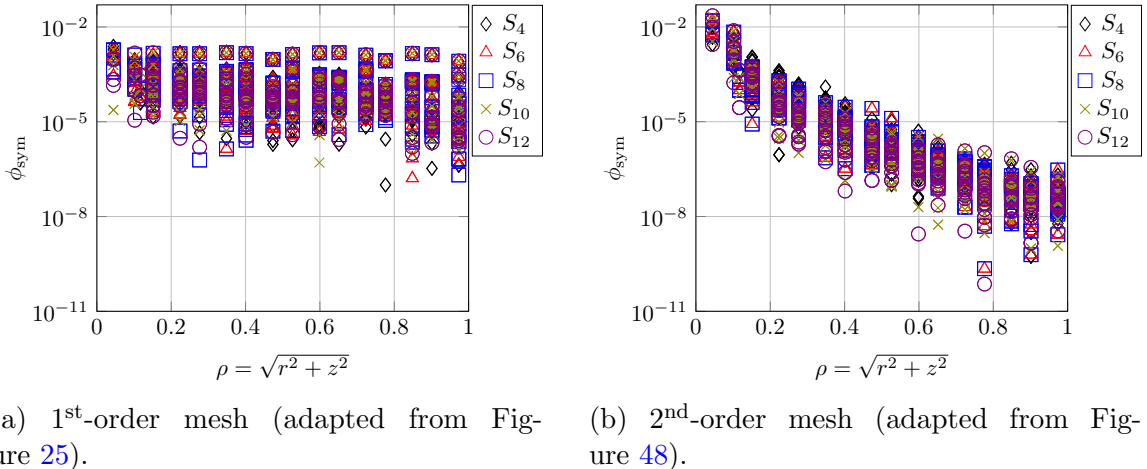


Figure 70: Measure of the asymmetry for each finite element node for the given level-symmetric angular quadrature order for 1<sup>st</sup>-order DFEM on the given mesh with 120 zones.

Table 3 summarizes these findings of whether or not each discretization property reduces the asymmetry or not.

Although the manufactured solution (Eq. 82) is seemingly simple, a steep gradient

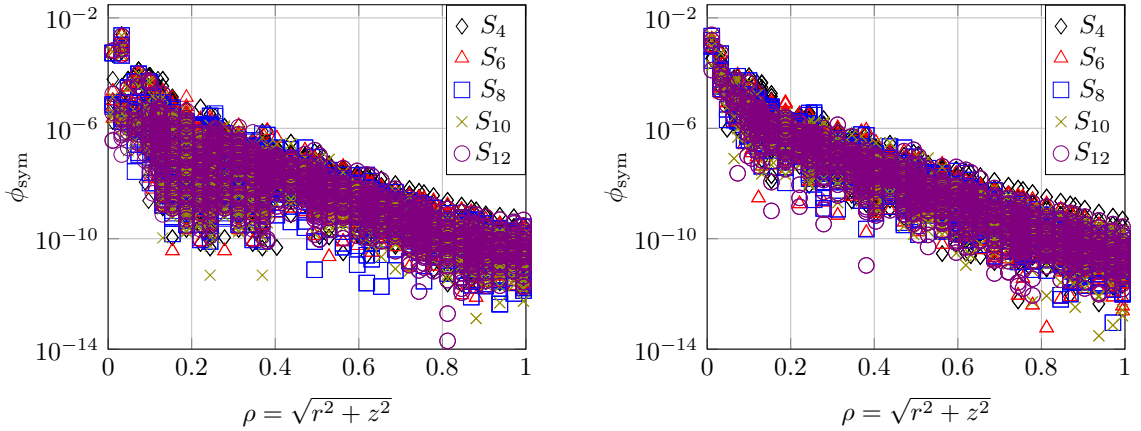
(a) 1<sup>st</sup>-order mesh (adapted from Figure 31).(b) 2<sup>nd</sup>-order mesh (adapted from Figure 54).

Figure 71: Measure of the asymmetry for each finite element node for the given level-symmetric angular quadrature order for 4<sup>th</sup>-order DFEM on the given mesh with 120 zones.

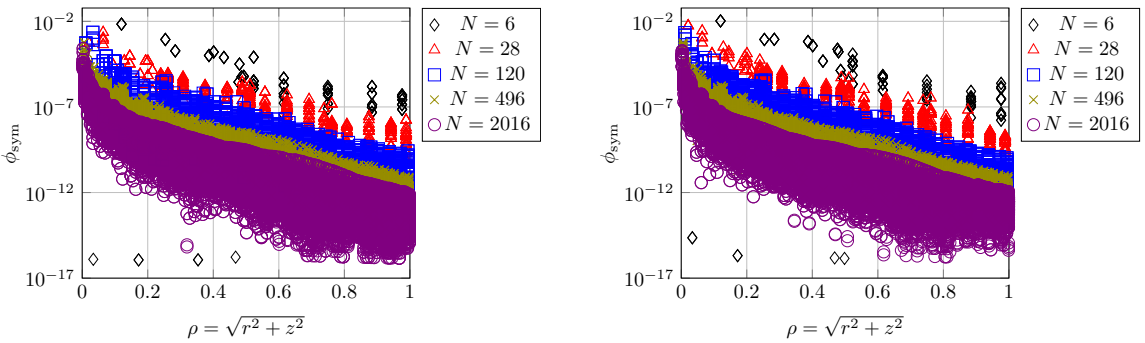
(a) 1<sup>st</sup>-order mesh (adapted from Figure 45).(b) 2<sup>nd</sup>-order mesh (adapted from Figure 65).

Figure 72: Measure of the asymmetry for each finite element node for 4<sup>th</sup>-order DFEM,  $S_8$  level-symmetric angular quadrature, on the given mesh with various number of zones.

appears in the MMS source term near  $(r, z) = (0, 0)$ . We look at each term of the transport equation using the manufactured solution in Figure 73. The gradient operated on the manufactured solution generates a very steep gradient near the origin. This contributes to the shape of the source term —  $S_0/(2\pi)$  is complicated near the origin. In practice, this source is an analytic driver for the radiation field in the

Table 3: Summary of discretizations and determination of whether they reduce the asymmetry.

Property	Reduce Asymmetry?
$S_N$ order	no
Finite element order	yes
mesh refinement	yes
mesh curvature	conditional

problem. The source term is approximated by the finite element shape function using the analytic values for the nodes. So although the source is exact at the node points, the shape function does not capture the analytic shape of the source term necessary to achieve the axisymmetry we desire.

In the future, we will examine this effect of the approximation on the analytical source term by one of two ways. We could utilize the same manufactured solution (Equation 82) in a spatial region that does not have as strong of a gradient (i.e., away from the origin). Or, we may have to consider alternative manufactured solutions that avoid the gradient at the origin. It would be ideal to have a manufactured solution that operates well in a region of interest but employing  $\rho = \sqrt{r^2 + z^2}$  will always result in some form of  $(r^2 + z^2)^{(-1/2)}$  in the streaming term.

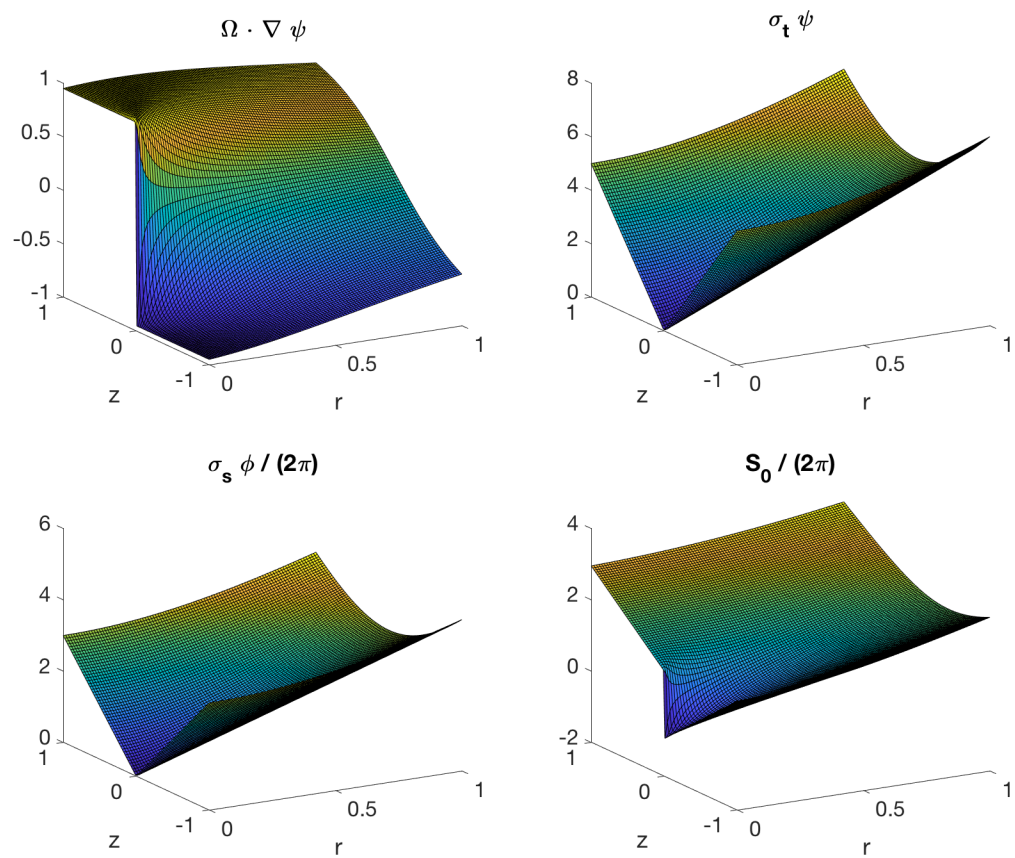


Figure 73: Analytic representation of each term of the transport equation using the manufactured solution, Equation 82, for  $(\mu, \xi) \approx (0.218, 0.951)$ . The complicated shapes of the streaming and source terms are typical of the other  $\Omega$  directions.

## 4.5 Strong Scatter with Alternating Boundaries Test

We previously tested a higher-order  $X$ - $Y$  transport methodology on an optically thick and highly scattering problem [26]. Here, we perform the same calculation in  $R$ - $Z$  geometry as originally introduced by Palmer and Adams [42] and Palmer [56]. The medium is homogeneous, highly scattering ( $c = 0.999$ ), has cross sections  $\sigma_t = 1000 \text{ cm}^{-1}$ ,  $\sigma_s = 999 \text{ cm}^{-1}$ , and has no external source. The incident angular flux boundary conditions of strength  $\psi_{inc} = 1/(2\pi) \text{ cm}^{-1} \text{ s}^{-1}$  on alternating locations denoted in Figure 74 by gray bars. This incident angular flux strength is an estimation to compare to previous research results [42, 56]. For comparison to previous research using BLD, we solve this problem using  $p = 1$  Gauss-Legendre DGFEM with  $S_4$  level-symmetric angular quadrature. The solution is shown in Figure 75. We observe oscillations in the solution that result in some negative scalar fluxes. The solution changes about 12 orders of magnitude. Compared to other research [56], we observe similar oscillations in the boundary layers, however the solution also presents oscillations in the problem interior. This may be due to the use of different basis functions or a result of not discretizing the conservation equation (Eq. 39).

We also solve with  $S_8$  level-symmetric angular quadrature using 4<sup>th</sup>-order finite elements. This solution is shown in Figure 76. We observe oscillations in the scalar flux that results in negative solutions. These are predominantly in the boundary layer regions near the upper right and lower left. The solution changes about 20 orders of magnitude.

Comparing Figures 75 and 76, we observe that the areas of negative solution in the problem interior is suppressed with the use of higher-order finite elements. We also observe that the higher-order FEM modeled a steeper gradient in the solution. The HO solution drove an additional 8 orders of magnitude further than the LO solution. While refining the mesh may help the LO method to model the steep gradient, the

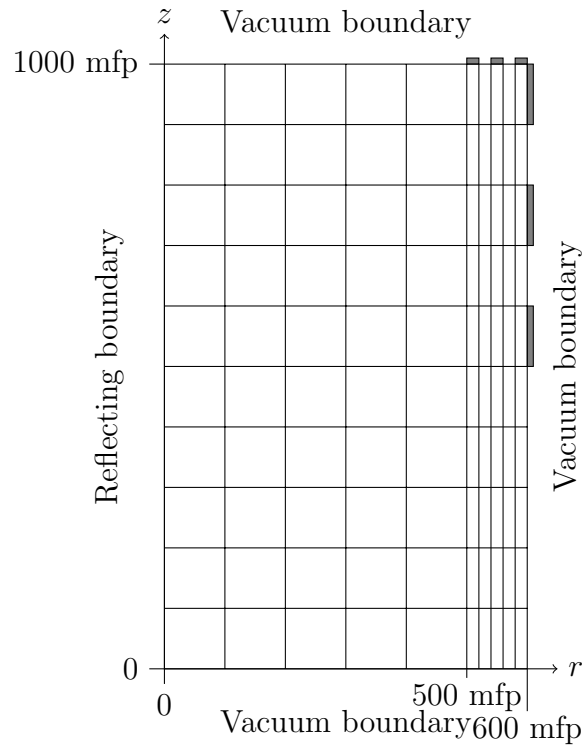


Figure 74: Strong scatter with discontinuous BCs with MIP DSA problem geometry; gray boundaries indicate incident boundary locations.

HO method was able to do so.

## 4.6 Material Discontinuity Stress Test

We adapted this problem from Palmer [56] and solved it without DSA in Woods et al. [26]. There are five different material regions described in Table 4 and Figure 78.

This problem has opacities that range several orders of magnitude, resulting in strong material discontinuities. We also introduce anisotropic incident intensities into the scattering region by preferentially attenuating intensities that are not perpendicular to the thick absorber. We expect some degradation in the DSA in problems with strong material discontinuities [25]. We also expect boundary layers to form from the anisotropic incident intensities [41]. The solution is shown in Figure 79.

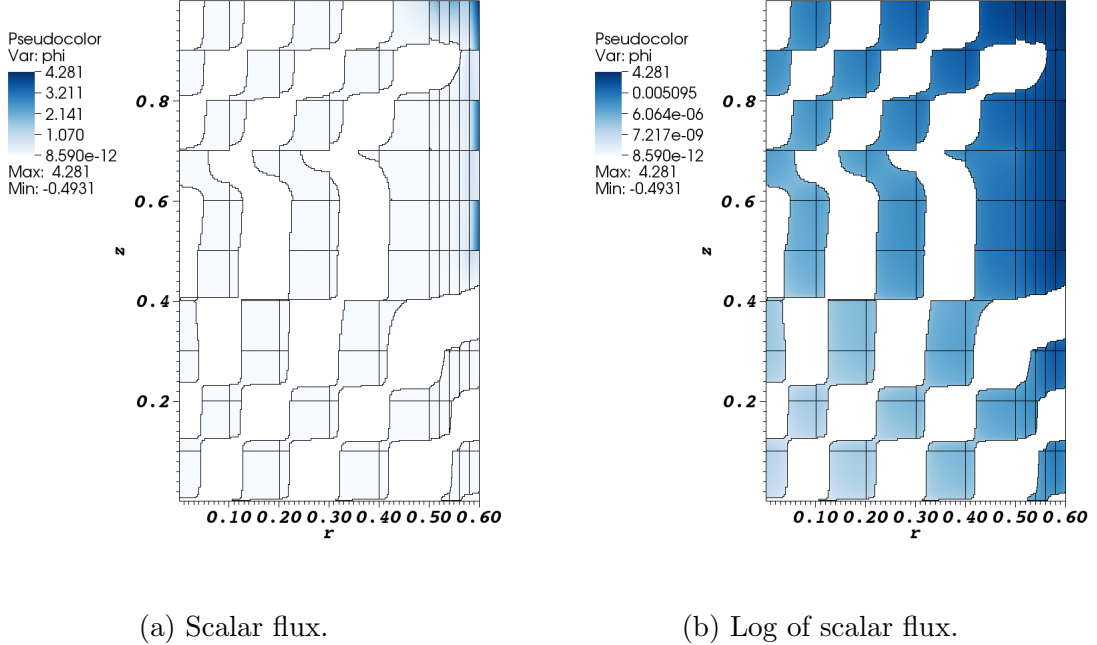


Figure 75: Solution to strong scatter with discontinuous boundary conditions with  $p = 1$  finite elements and  $S_4$  level-symmetric angular quadrature. White regions indicate negative scalar fluxes.

Table 4: Material discontinuity stress test with MIP DSA material properties.

Material Region	$\sigma_t \text{ cm}^{-1}$	$\sigma_s \text{ cm}^{-1}$	$S_0 \text{ cm}^{-2} \text{ s}^{-1}$
Source	1.0	1.0	1.0
Very thin absorber	0.0001	0.0	0.0
Thick absorber	10.0	0.0	0.0
Very thick absorber	100.0	0.0	0.0
Very thick scatterer	1000.0	1000.0	0.0

## 4.7 R-Z Geometry Conclusions

We discretized the transport equation in *R-Z* geometry and performed several test problems to qualitatively and quantitatively assess the behavior of the high-order finite element spatial discretization method. Instead of performing the spatial discretization on the conservation form of the transport equation, we performed a prod-

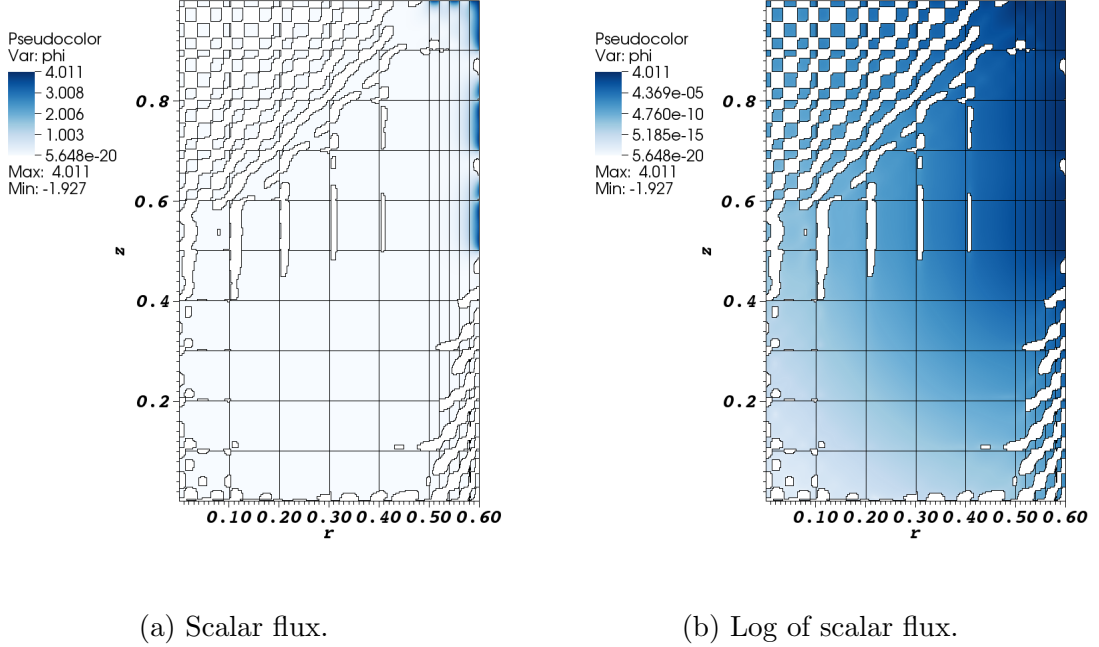


Figure 76: Solution to strong scatter with discontinuous boundary conditions with  $p = 4$  finite elements and  $S_8$  level-symmetric angular quadrature. White regions indicate negative scalar fluxes.

uct rule and pulled a radius variable out of the  $r$ -derivative term. This allowed us to easily extend a  $X$ - $Y$  geometry implementation in MFEM to  $R$ - $Z$  geometry. We discretized the direction of travel using level-symmetric angular quadrature and used the method of Morel and Montry to sweep across each angular quadrature level to solve for the angular flux at each discrete ordinate. The source iteration method was employed, where we calculate the scalar flux from a weighted sum of the angular fluxes, use that scalar flux in the scattering source, and iterate on the scalar flux until it converges.

This method was sufficiently able to solve a uniform infinite medium problem. We extended the analysis to a spatial convergence study using the method of manufactured solutions. The chosen manufactured solution is smooth everywhere and resulted in the expected  $O(p+1)$  spatial convergence rates, which was expected from

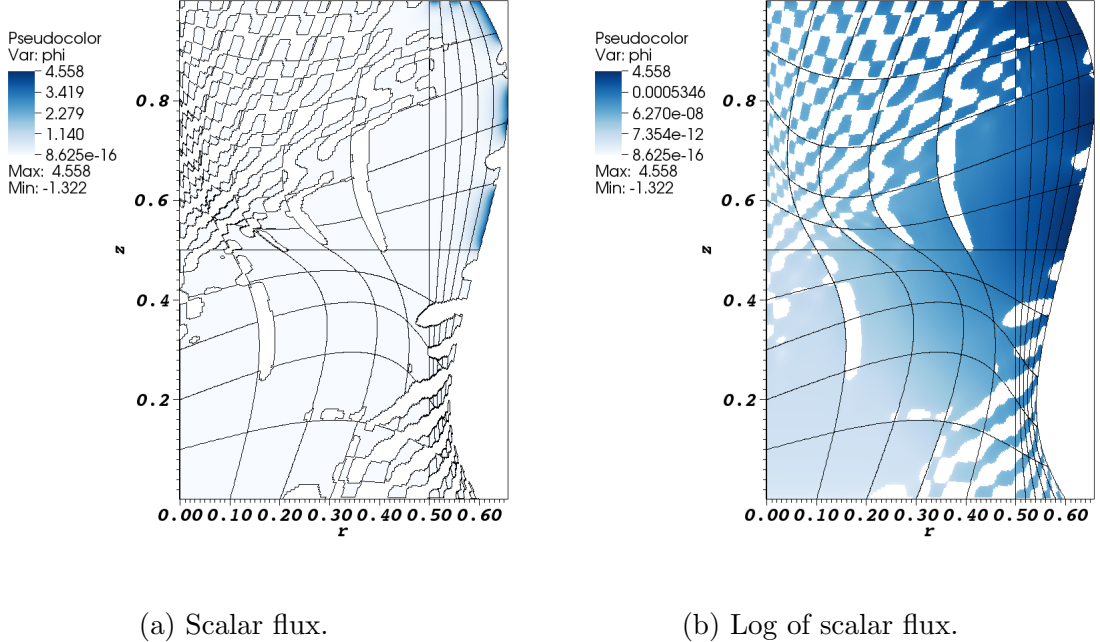


Figure 77: Solution to strong scatter with discontinuous boundary conditions with  $p = 4$  finite elements and  $S_{12}$  level-symmetric angular quadrature on a 2<sup>nd</sup>-order mesh. White regions indicate negative scalar fluxes.

other research.

Finally, we performed a study on preserving axisymmetry (i.e. 1-D spherical symmetry). An ideal method will be able to solve a 1-D spherical problem using a  $R$ - $Z$  geometry discretization. We solved using the method of manufactured solutions and determined a measure of symmetry. We varied the finite element order, angular quadrature order, spatial refinement, and mesh order. For a 1<sup>st</sup>-order mesh, we determined that the angular quadrature order has very little impact on the relative symmetry of the solution. At sufficient me

For a 2<sup>nd</sup>-order mesh, we determined that the angular quadrature order has very little impact on the relative symmetry of the solution. At a sufficient mesh refinement, the relative symmetry produces distinct “rays”. The number of these rays increases with the angular quadrature order. However, these rays were drastically damped by

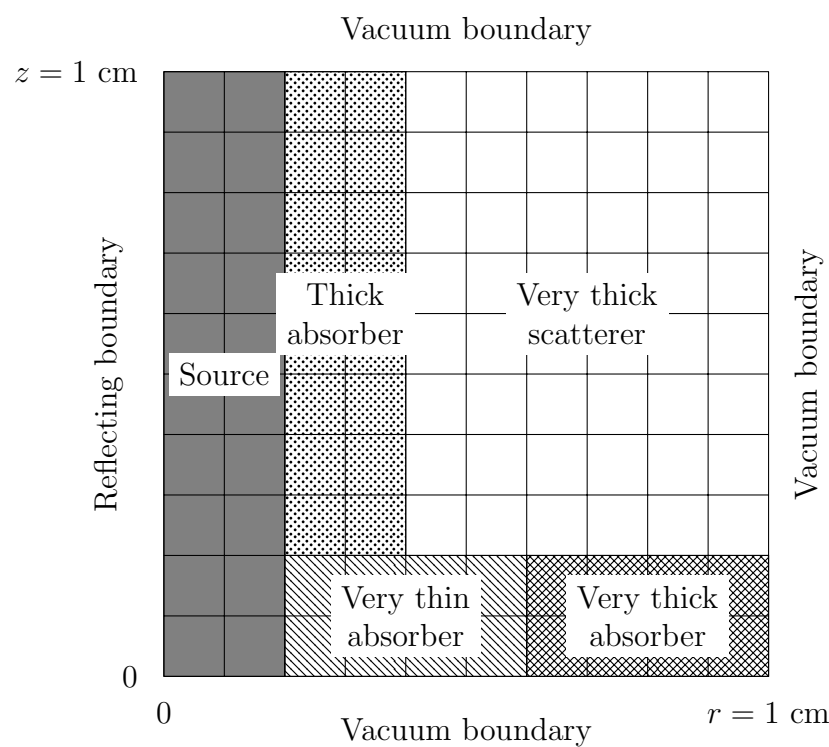


Figure 78: Material discontinuity stress test with MIP DSA problem geometry; materials defined in Table 4.

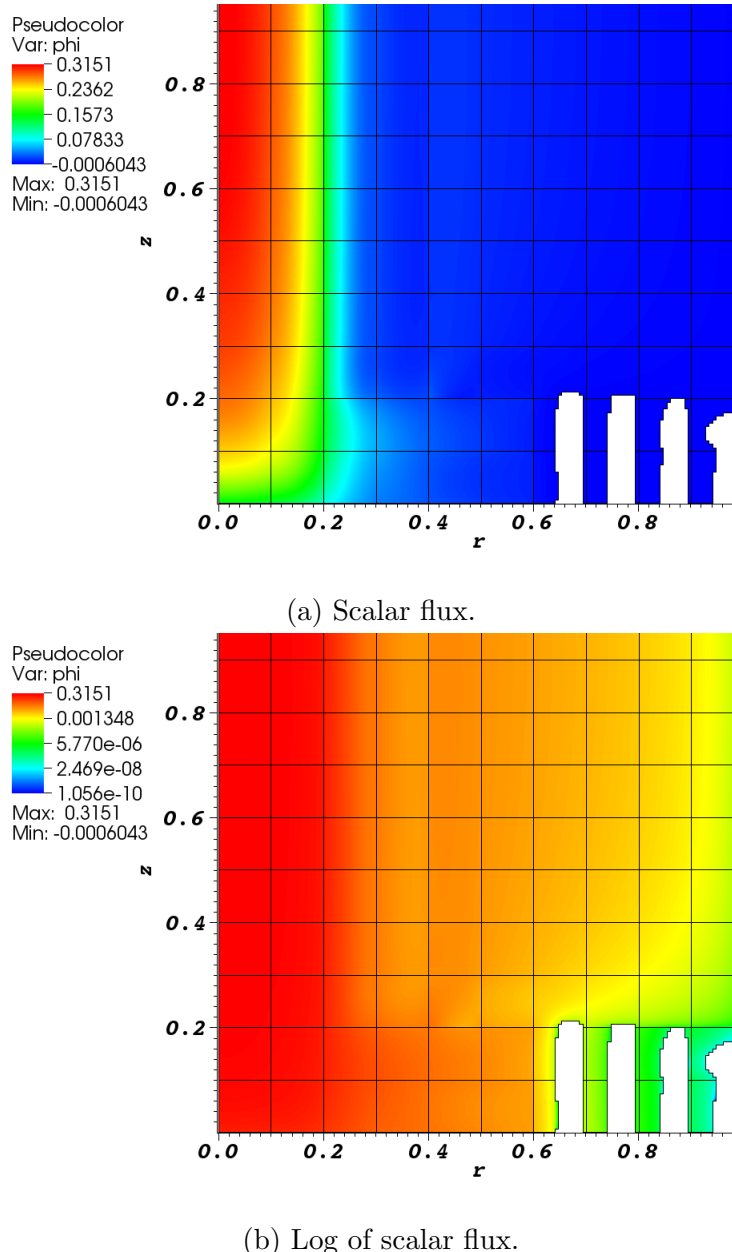


Figure 79: Solution to multi-material stress test. White regions indicate negative scalar fluxes.

increasing the finite element order.

In future work, we will investigate alternative methods for handling the angular derivative. Warsa and Prinja [68] proposed a method by performing a product rule on the angular derivative. We will also implement the numerical solution to the

conservative form of the radiation transport equation in  $R$ - $Z$  geometry.

It is common for the solution to the thermal radiation transport equation to be averaged over each mesh zone to be used in the energy balance equation for hydrodynamics calculations. We will also consider cell average axisymmetry. Also for the axisymmetric manufactured solution, we would like to develop other manufactured solutions that have simpler manufactured source terms near the origin. The complicated source term that we used was sufficient for  $(r, z)$  coordinates further from the origin, but the finite element approximated source term was not close enough to the analytical source near the origin to maintain symmetry. Lastly, the mesh used for the axisymmetry calculations was made entirely of quadrilaterals. That is, even the innermost zones were quadrilaterals with one vertex having a very oblique angle (nearly 180 degrees). We need to modify MFEM to handle mixed element types.

## 5 Conclusions

In this dissertation, we derived and implemented the Robin boundary condition for the modified interior penalty (MIP) diffusion synthetic acceleration (DSA) equations. The prior discretization was unconditionally convergent in all optical thicknesses but contained a dependency that was user defined. The Robin boundary condition tremendously reduces the impact of this dependency, while still being an unconditionally stable method. We observed a degradation in the convergence rate in optically thick material, that we leave to future work.

We additionally derived and implemented an *R-Z* geometry spatial discretization for the high-order (HO) discontinuous finite element method(DFEM). Using several numerical test problems we observed the preservation of the  $O(p+1)$  spatial convergence rates that was expected and has been seen for 1<sup>st</sup>-order methods on sufficiently smooth solutions. We also demonstrated that this convergence rate is unaffected by meshes with curved surfaces. This work has extended the results to high-order methods and onto meshes with curved surfaces. Regularity constrained solutions can have degraded spatial convergence rates, and we demonstrated that the convergence rates are no longer dependent upon the finite element order, although HO methods generally obtain smaller errors. Finally, we examined the ability to preserve spherical symmetry with *R-Z* geometry. In general, the finite element order and the mesh refinement determined the symmetry preservation. Neither the  $S_N$  order nor the curvature of the mesh had significant impact. The exception is that for 1<sup>st</sup>-order finite elements the mesh curvature did increase the spherical symmetry.

## 5.1 FutureWork

To efficiently solve for larger problems (i.e., more degrees of freedom), it is essential to investigate methods for solving the system of equations. Currently we simultaneously solve for every degree of freedom in the problem. This limits the overall number of unknowns that we can accommodate because they all get stored in memory. However, if we solved individual mesh cells and systematically “swept through the mesh” (solve the sparse system of equations for each quadrature direction, in parallel or sequentially), we eliminate this limitation. This research will require allowing for cycles in the mesh, which will require careful handling.

An investigation into numerical integration methods for the surfaces that have both incident and outgoing angular fluxes is prudent. On these meshes with curved surfaces, integrating a surfaces that has a discontinuous first-derivative with a polynomial approximation may not be the most effective method.

Negative scalar fluxes, observed in some of the test problems above, are non-physical and must be addressed. Other research has utilized lumping techniques on several of the matrices that constitute the bilinear form. Alternatively, negative flux fixup methods could be employed to correct the negativities after solving for the scalar flux. This results in a non-linear system of equations that may be acceptable in more complicated multiphysics applications that are already non-linear.

## References

- [1] Douglas N. Woods and Todd S. Palmer. Diffusion synthetic acceleration for high order  $S_N$  transport on meshes with curved surfaces. *Transactions of the American Nuclear Society*, (116):639–642, 2017.
- [2] E. E. Lewis and W. F. Miller, Jr. *Computational Methods of Neutron Transport*. American Nuclear Society, 1993.
- [3] James J. Duderstadt and Louis J. Hamilton. *Nuclear Reactor Analysis*. Wiley-Interscience, 1976.
- [4] Peter A. Sandwall, Yuntao Feng, Michael Platt, Michael Lamba, and Sudha Mahalingam. Evolution of brachytherapy treatment planning to deterministic radiation transport for calculation of cardiac dose. *Medical Dosimetry*, 43(2):150–158, 2018.
- [5] John Castor. *Radiation Hydrodynamics*. Cambridge, 2007.
- [6] R. Paul Drake. High-energy-density physics. *Physics Today*, 63(3):8–9, June 2010.
- [7] Veselin A. Dobrev, Tzanio V. Kolev, and Robert N. Rieben. High-order curvilinear finite element methods for Lagrangian hydrodynamics. *SIAM Journal of Scientific Computing*, 34(5):B606 – B641, 2012.
- [8] V. A. Dobrev, T. E. Ellis, Tz. V. Kolev, and R. N. Rieben. Curvilinear finite elements for lagrangian hydrodynamics. *International Journal for Numerical Methods in Fluids*, 2010.
- [9] MFEM: Modular finite element methods. [mfem.org](http://mfem.org), 2015.
- [10] K. D. Lathrop and B. G. Carlson. Discrete ordinates angular quadrature of the neutron transport equation. Technical report, Los Alamos Scientific Laboratory of the University of California, 1965.
- [11] Peter J. Spence. The generation of arbitrary order, non-classical, Gauss-type quadrature for transport applications. *Journal of Computational Physics*, 296:25–27, 2015.
- [12] Marvin L. Adams, Todd A. Wareing, and Wallace F. Walters. Characteristic methods in thick diffusive problems. *Nuclear Science and Engineering*, 130:18–46, 1998.
- [13] W. H. Reed and T. R. Hill. Triangular mesh methods for the neutron transport equation. Technical Report LA-UR-73-479, Los Alamos National Laboratory, 1973.

- [14] Edward W. Larsen and J. E. Morel. Asymptotic solutions of numerical transport problems in optically thick, diffusive regimes II. *Journal of Computational Physics*, 83:212–236, 1989.
- [15] P. Lasaint and P. A. Raviart. On a finite element method for solving the neutron transport equation. In Carl de Boor, editor, *Mathematical Aspects of Finite Elements in Partial Differential Equations*, pages 89–123. Academic Press, 1974.
- [16] Edward W. Larsen and Warren F. Miller, Jr. Convergence rates of spatial difference equations for the discrete-ordinates neutron transport equations in slab geometry. *Nuclear Science and Engineering*, 1980.
- [17] Steven Hamilton, Michele Benzi, and Jim Warsa. Negative flux fixups in discontinuous finite element  $S_N$  transport. *International Conference on Mathematics, Computational Methods & Reactor Physics*, May 2009.
- [18] Marvin L. Adams. Discontinuous finite element transport solutions in thick diffusive problems. *Nuclear Science and Engineering*, 137(3):298–333, 2001.
- [19] Todd A. Wareing, John M. McGhee, and Jim E. Morel. ATTILA: A three-dimensional, unstructured tetrahedral mesh discrete ordinates transport code. *Transactions of the American Nuclear Society*, 75:146–147, 1996.
- [20] J. M. McGhee and T.A. Wareing. *Attila Version 2: User's Manual*. Los Alamos National Laboratory, 2000.
- [21] Teresa S. Bailey, Marvin L. Adams, Jae H. Chang, and James S. Warsa. A piecewise linear discontinuous finite element spatial discretization of the transport equation in 2D cylindrical geometry. *International Conference on Mathematics, Computational Methods & Reactor Physics*, 2009.
- [22] Yaqi Wang and Jean C. Ragusa. Diffusion synthetic acceleration for high-order discontinuous finite element  $S_N$  transport schemes and application to locally refined unstructured meshes. *Nuclear Science and Engineering*, 166:145–166, 2010.
- [23] Yaqi Wang and Jean C. Ragusa. A high-order discontinuous Galerkin method for the  $S_N$  transport equations on 2D unstructured triangular meshes. *Annals of Nuclear Energy*, 36:931–939, 2009.
- [24] Yaqi Wang and Jean C. Ragusa. On the convergence of DGFEM applied to the discrete ordinates transport equation for structured and unstructured triangular meshes. *Nuclear Science and Engineering*, 163:56–72, 2009.
- [25] Yaqi Wang. *Adaptive Mesh Refinement Solution Techniques for the Multigroup  $S_N$  Transport Equation Using a Higher-Order Discontinuous Finite Element Method*. PhD thesis, Texas A&M University, 2009.

- [26] Douglas N. Woods, Thomas A. Brunner, and Todd S. Palmer. High order finite elements  $S_N$  transport in X-Y geometry on meshes with curved surfaces. *Transactions of the American Nuclear Society*, 114:377 – 380, June 2016.
- [27] Douglas N. Woods. High order finite elements  $S_N$  transport in X-Y geometry on meshes with curved surfaces in the thick diffusion limit. Master’s thesis, Oregon State University, February 2016.
- [28] Peter G. Maginot, Jim E. Morel, and Jean C. Ragusa. A non-negative moment-preserving spatial discretization scheme for the linearized Boltzmann transport equation in 1-D and 2-D Cartesian geometries. *Journal of Computational Physics*, 231:6801–6826, 2012.
- [29] Peter G. Maginot, Jean C. Ragusa, and Jim E. Morel. Lumping techniques for DFEM  $S_N$  transport in slab geometry. *Nuclear Science and Engineering*, 2015.
- [30] Thomas A. Brunner. Preserving positivity of solutions to the diffusion equation for higher-order finite elements in under resolved regions. In *ANS M&C - Joint International Conference on Mathematics and Computation (M&C), Supercomputing in Nuclear Applications (SNA) and the Monte Carlo (MC) Method*, April 2015.
- [31] Jim E. Morel, Alejandro Gonzales-Aller, and James S. Warsa. A lumped linear-discontinuous spatial discretization scheme for triangular-mesh  $S_N$  calculations in r-z geometry. *Nuclear Science and Engineering*, 155:168–178, 2007.
- [32] *Discrete Ordinates Methods with Curved Spatial Grids : an Alternative Method to MOC*, September 2015.
- [33] Sebastian Schunert, Yaqi Wang, Vincent Laboure, Javier Ortensi, and Mark DeHart. Approximate transport sweeps for DFEM on higher order meshes with spatially varying cross sections. *Transactions of the American Nuclear Society*, 117:701–705, 2017.
- [34] Juan Cheng and Chi-Wang Shu. A third order conservative Lagrangian type scheme on curvilinear meshes for the compressible Euler equations. *Communications in Computational Physics*, 4(5):1008–1024, 2008.
- [35] Veselin A. Dobrev, Truman E. Ellis, Tzanio V. Kolev, and Robert N. Rieben. High-order curvilinear finite elements for axisymmetric Lagrangian hydrodynamics. *Computers & Fluids*, 2012.
- [36] Edward W. Larsen, J. E. Morel, and Warren F. Miller, Jr. Asymptotic solutions of numerical transport problems in optically thick, diffusive regimes. *Journal of Computational Physics*, 69:283–324, 1987.

- [37] F. Malvagi and G. C. Pomraning. Initial and boundary conditions for diffusive linear transport problems. *Journal of Mathematical Physics*, 32(3):805–820, 1991.
- [38] Edward W. Larsen. The asymptotic diffusion limit of discretized transport problems. *Nuclear Science and Engineering*, 112:336–346, 1992.
- [39] Christoph Börgers, Edward W. Larsen, and Marvin L. Adams. The asymptotic diffusion limit of a linear discontinuous discretization of a two-dimensional linear transport equation. *Journal of Computational Physics*, 98(2):285–300, 1992.
- [40] Jim E. Morel and James S. Warsa. An  $S_N$  spatial discretization scheme for tetrahedral meshes. *Nuclear Science and Engineering*, 151:157–166, 2005.
- [41] Marvin L. Adams. Discontinuous finite-element transport solutions in the thick diffusion limit in Cartesian geometry. *The American Nuclear Society International Topical Meeting*, 1991.
- [42] Todd S. Palmer and Marvin L. Adams. Curvilinear geometry transport discretization in the "thick" diffusion limit. *Proceedings of the International Conference Math. Methods & Supercomputing in Nuc. Appl.*, 1993.
- [43] J. E. Morel and J. S. Warsa. A lumped bilinear-discontinuous  $S_N$  spatial discretization for R-Z quadrilateral meshes. *Transactions of the American Nuclear Society*, 95:873, 2006.
- [44] Hiromi G. Stone and Marvin L. Adams. A piecewise linear finite element basis with application to particle transport. *Nuclear Mathematical and Computational Sciences: A Century in Review, A Century Anew*, 2003.
- [45] Teresa Bailey. *A Piecewise Linear Discontinuous Finite Element Method Applied to the RZ and XYZ Transport Equations*. PhD thesis, Texas A&M University, 2008.
- [46] T. S. Bailey, J. H. Chang, J. S. Warsa, and M. L. Adams. A piecewise bi-linear discontinuous finite element spatial discretization of the  $S_N$  transport equation. *International Conference on Mathematics and Computational Methods Applied to Nuclear Science and Engineering*, 2011.
- [47] Edward W. Larsen. Unconditionally stable diffusion-synthetic acceleration methods for the slab geometry discrete ordinates equations. part I: Theory. *Nuclear Science and Engineering*, 82(1):47–63, 1982.
- [48] Todd A. Wareing, Edward W. Larsen, and Marvin L. Adams. Diffusion accelerated discontinuous finite element schemes for the  $S_N$  equations in slab and X,Y geometries. 1991.

- [49] James S. Warsa, Todd A. Wareing, and Jim E. Morel. Fully consistent diffusion synthetic acceleration of linear discontinuous  $S_N$  transport discretizations on unstructured tetrahedral meshes. *Nuclear Science and Engineering*, 141:236–251, 2002.
- [50] Marvin L. Adams and Edward W. Larsen. Fast iterative methods for discrete-ordinates particle transport calculations. *Progress in Nuclear Energy*, 40(1):3–159, 2002.
- [51] Donald R. McCoy and Edward W. Larsen. Unconditionally stable diffusion-synthetic acceleration methods for the slab geometry discrete ordinates equations. part II: Numerical results. *Nuclear Science and Engineering*, 82(1):64–70, 1982.
- [52] Marvin L. Adams and William R. Martin. Diffusion synthetic acceleration of discontinuous finite element transport iterations. *Nuclear Science and Engineering*, 111:145–167, 1992.
- [53] Bruno Turcksin and Jean C. Ragusa. Discontinuous diffusion synthetic acceleration for  $S_N$  transport on 2D arbitrary polygonal meshes. *Journal of Computational Physics*, 274:356–369, 2014.
- [54] Bruno Turcksin and Jean C. Ragusa. A diffusion synthetic acceleration scheme for rectangular geometries based on bilinear discontinuous finite elements. In *International Conference on Mathematics and Computational Methods, Applied to Nuclear Science and Engineering*. Sun Valley, Idaho, 2013.
- [55] Guido Kanschat. *Discontinuous Galerkin Methods for Viscous Incompressible Flow*. Deutscher Universitäts-Verlag, 2007.
- [56] Todd S. Palmer. *Curvilinear Geometry Transport Discretization in Thick Diffusive Regions*. PhD thesis, University of Michigan, 1993.
- [57] Douglas N. Woods and Todd S. Palmer. R-Z geometry discrete ordinates radiation transport using higher-order finite element spatial discretizations on meshes with curved surfaces. *Journal of Computational and Theoretical Transport*, In Review.
- [58] Thomas A. Brunner, Tzanio V. Kolev, and Teresa S. Bailey. Preserving spherical symmetry in axisymmetric coordinates for diffusion problems. *International Conference on Mathematics and Computational Methods Applied to Nuclear Science and Engineering*, 2013.
- [59] F. Chaland and G. Samba. Discrete ordinates method for the transport equation preserving one-dimensional spherical symmetry in two-dimensional cylindrical geometry. *Nuclear Science and Engineering*, 182:417–434, 2016.

- [60] C. Lingus. Analytical test case's for neutron and radiation transport codes. In *Second Conference on Transport Theory*, pages 655–659, Los Alamos, New Mexico, January 1971. United States Atomic Energy Commission - Division of Technical Information.
- [61] Shawn D. Pautz. An algorithm for parallel  $S_n$  sweeps on unstructured meshes. *Nuclear Science and Engineering*, 140:111–136, 2002.
- [62] Todd A. Wareing, John M. McGhee, Jim E. Morel, and Shawn D. Pautz. Discontinuous finite element  $S_N$  methods on three-dimensional unstructured grids. *Nuclear Science and Engineering*, 138:256–268, 2001.
- [63] Timothy A. Davis. *Direct Methods for Sparse Linear Systems*. Society for Industrial and Applied Mathematics, 2006.
- [64] Timothy A. Davis. Algorithm 832: Umfpack v4.3 — an unsymmetric-pattern multifrontal method. *ACM Transactions on Mathematical Software*, 30(2):196–199, June 2004.
- [65] James S. Warsa, Todd A. Wareing, and Jim E. Morel. Krylov iterative methods and the degraded effectiveness of diffusion synthetic acceleration for multidimensional  $S_N$  calculations in problems with material discontinuities. *Nuclear Science and Engineering*, 147(3):218–248, 2004.
- [66] J. E. Morel and G. R. Montry. Analysis and elimination of the discrete-ordinates flux dip. *Transport Theory and Statistical Physics*, 13(5):615–633, 1984.
- [67] Mohammad Asadzadeh. Analysis of a fully discrete scheme for neutron transport in two-dimensional geometry. *SIAM Journal of Numerical Analysis*, 23(3):543–561, 1986.
- [68] J. S. Warsa and A. K. Prinja. Differential quadrature approximation of the angular derivative terms in the curvilinear-coordinates  $S_N$  equations. *Transactions of the American Nuclear Society*, 111:689–692, 2014.
- [69] Hank Childs, Eric Brugger, Brad Whitlock, Jeremy Meredith, Sean Ahern, David Pugmire, Kathleen Biagas, Mark Miller, Cyrus Harrison, Gunther H. Weber, Hari Krishnan, Thomas Fogal, Allen Sanderson, Christoph Garth, E. Wes Bethel, David Camp, Oliver Rübel, Marc Durant, Jean M. Favre, and Paulr Navrátil. Visit: An end-user tool for visualizing and analyzing very large data. In *High Performance Visualization—Enabling Extreme-Scale Scientific Insight*, pages 357–372. Oct 2012.
- [70] Douglas N. Woods, Thomas A. Brunner, and Todd S. Palmer. High order finite element  $S_N$  radiation transport on meshes with curved surfaces. *Nuclear Science and Engineering*, In Review.

## A Implementation in MFEM

The open source finite element library Modular Finite Elements Method (MFEM<sup>7</sup>) [9] was used to create the system of linear equations to be solved by a linear algebra solver. The user chooses various parameters to create the system of equations and passes them into MFEM as arguments (i.e. the order of finite elements, the mesh, the number of times to refine the mesh, the order of the mesh, any mesh transformations, the linear algebra solver method, the source iteration convergence criteria, the maximum number of source iterations to perform, the initial guess for the scalar flux, and, in diffusion limit problems, the scaling factor to be applied).

MFEM creates the matrices and a linear solver computes the angular flux. This research utilizes the serial version of MFEM (as opposed to the parallel version where the spatial domain is solved in parallel) and the direct solver UMFPack<sup>8</sup> [63, 64] to solve the equations using a *LU* decomposition. It is common for transport solvers to solve the local system of equations for an individual spatial cell and sweep through the problem domain, propagating information from one cell to the next. Instead, we use MFEM to create the system of equations for the entire problem domain and solve for all of the unknowns in all cells simultaneously. This is more computationally intensive because all of the degrees of freedom in the entire problem domain must be solved for simultaneously. However, mesh zone complications, such as cycles, may be present in the mesh. We avoid having to “break the cycles” by solving for the entire problem simultaneously.

The following two sections describe the operators used in MFEM to accomplish this research. Specifically, Section A.1 describes the operators used to solve the transport equation. Section A.2 describes the operators used to solve the MIP DSA

---

<sup>7</sup>[mfem.org](http://mfem.org)

<sup>8</sup><http://faculty.cse.tamu.edu/davis/suitesparse.html>

equations.

## A.1 Transport Operators

Shown in Table 5 are the functions within MFEM that integrate and assemble the various operators of the transport equation in  $X$ - $Y$  geometry. These are all available by default in the MFEM distribution. The functions are displayed along with the general form of their equation and their translation to the applicable component of the transport equation. The last two entries of Table 5 are the interior boundaries using the upstream values (no. 5) and the problem boundary (no. 6). Several of the MFEM equations have coefficients,  $\alpha$  and  $\beta$ , that are required input.

The normal vector  $\hat{n}$  in MFEM is outward of the upwind mesh surface so a negative was applied to the normal vector to convert it to be the outward normal of the surface of cell  $k$  like it has been previously defined in this dissertation.

In order to perform the spatial integrations with a factor of  $r$  we needed to modify the existing MFEM integrators. In general, this required multiplying the integrand by the physical  $r$  location. Since we performed an integration by parts on the streaming operator to remove the  $r$  from the  $r$ -derivative term, this greatly simplified our modification of these terms. Future research may require multiplying the basis function by  $r$  prior to calculating the derivative at the integration point in order to preserve the conservation form of the  $R$ - $Z$  transport equation. The operators for the  $R$ - $Z$  transport equation and their MFEM implementations are shown in Table 6.

MFEM has default settings for determining the degree of numerical integration to integrate each of the integrals of Tables 5 and 6. These default integration orders are shown in Table 7. It was discovered that integrating all of the terms consistently was important for numerical conservation. For simplicity, each of the integration orders were set to the largest of the default integration orders. Table 7 shows that the

integration order is the same for all of the integrators except DomainLFIntegrator, which is the largest integration order only if  $p = 0$  (piecewise constant). While the results presented in this dissertation do not consider the circumstance of piecewise constant finite elements, this integration order was included in the code for future use.

MFEM is equipped to visualize data using various tools requiring additional user input. The images presented in this dissertation were produced with VisIt, an open source visualization analysis tool [69].

## A.2 MIP DSA Operators

There are some specific function calls to MFEM for the diffusion equation that are listed in Table 8. Items 3 and 4 have a  $\sigma_D$  value that controls the DG method to be used, where  $\sigma_D = -1$  is for the symmetric interior penalty method. Item 6 is for the Robin boundary condition described by Equation 25.

no.	Discretized Equation	MFEM Equation	MFEM Integrator Function
1	$(\boldsymbol{\Omega} \cdot \nabla \psi_j, v_i)_{\mathcal{D}_k}$	$(\alpha \boldsymbol{\Omega} \cdot \nabla \psi, v)_{\mathcal{D}_k}$	ConvectionIntegrator( $\boldsymbol{\Omega}, \alpha$ )
2	$(\sigma_t \psi_j, v_i)_{\mathcal{D}_k}$	$(\sigma_t \psi, v)_{\mathcal{D}_k}$	MassIntegrator( $\sigma_t$ )
3	$(\sigma_s \phi, v_i)_{\mathcal{D}_k}$	$(\varphi, v)_{\mathcal{D}_k}$	DomainLFIIntegrator( $\varphi$ )
4	$(S_0, v_i)_{\mathcal{D}_k}$	$(S_0, v)_{\mathcal{D}_k}$	DomainLFIIntegrator( $S_0$ )
5	$(\boldsymbol{\Omega} \cdot \hat{n} \psi_j, v_i)_{\partial \mathcal{D}_k^e}$	$\alpha (\boldsymbol{\Omega} \cdot \hat{n} \psi, v)_{\partial \mathcal{D}_k^e}$ + $\beta ( \boldsymbol{\Omega} \cdot \hat{n}  \psi, v)_{\partial \mathcal{D}_k^e}$	DGTraceIntegrator( $\boldsymbol{\Omega}, \alpha, \beta$ )
6	$(\boldsymbol{\Omega} \cdot \hat{n} \psi_j, v_i)_{\partial \mathcal{D}_k^b}$	$\alpha (\boldsymbol{\Omega} \cdot \hat{n} \psi, v)_{\partial \mathcal{D}_k^b}$ + $\beta ( \boldsymbol{\Omega} \cdot \hat{n}  \psi, v)_{\partial \mathcal{D}_k^b}$	DGTraceIntegrator( $\boldsymbol{\Omega}, \alpha, \beta$ )
7	$(\boldsymbol{\Omega} \cdot \hat{n} \psi_{inc}, v_i)_{\partial \mathcal{D}_k}$	$\frac{\alpha}{2} (\psi_{inc} \boldsymbol{\Omega} \cdot \hat{n}, v)_{\partial \mathcal{D}_k}$ - $\beta (\psi_{inc}  \boldsymbol{\Omega} \cdot \hat{n} , v)_{\partial \mathcal{D}_k}$	BoundaryFlowIntegrator( $\psi_{inc}, \boldsymbol{\Omega}, \alpha, \beta$ )

Table 5: MFEM transport operator function calls where the arguments have been dropped.

no.	Discretized Equation	MFEM Equation	MFEM Integrator Function
1	$(r \mu_{n,m} \cdot \partial_r \psi_{n,m,j}, v_i)_{\mathcal{D}_k}$ $(r \xi_m \cdot \partial_z \psi_{n,m,j}, v_i)_{\mathcal{D}_k}$	$(r \alpha \Omega \cdot \nabla \psi, v)_{\mathcal{D}_k}$	RZConvectionIntegrator( $\Omega, \alpha$ )
2	$(r \mu_{n,m} \cdot \hat{n} \psi_{n,m,j}, v_i)_{\mathcal{D}_k^e}$ $(r \xi_m \cdot \hat{n} \psi_{n,m,j}, v_i)_{\mathcal{D}_k^e}$	$\alpha(r \Omega \cdot \hat{n} \psi, v)_{\partial \mathcal{D}_k^e}$ $+ \beta(r  \Omega \cdot \hat{n}  \psi, v)_{\partial \mathcal{D}_k^e}$	RZDGTraceIntegrator( $\Omega, \alpha, \beta$ )
3	$(r \mu_{n,m} \cdot \hat{n} \psi_{n,m,j}, v_i)_{\mathcal{D}_k^b}$ $(r \xi_m \cdot \hat{n} \psi_{n,m,j}, v_i)_{\mathcal{D}_k^b}$	$\alpha(r \Omega \cdot \hat{n} \psi, v)_{\partial \mathcal{D}_k^b}$ $+ \beta(r  \Omega \cdot \hat{n}  \psi, v)_{\partial \mathcal{D}_k^b}$	RZDGTraceIntegrator( $\Omega, \alpha, \beta$ )
4	$(\mu_{n,m} \psi_j, v_i)_{\mathcal{D}_k}$	$(\mu_{n,m} \psi, v)_{\mathcal{D}_k}$	MassIntegrator( $\mu_{n,m}$ )
5	$\left( \frac{\alpha_{m+1/2} n}{\tau_{n,m} w_{n,m}} \psi_j, v_i \right)_{\mathcal{D}_k}$	$\left( \frac{\alpha_{m+1/2} n}{\tau_{n,m} w_{n,m}} \psi, v \right)_{\mathcal{D}_k}$	MassIntegrator( $\frac{\alpha_{m+1/2} n}{\tau_{n,m} w_{n,m}}$ )
6	$(r \sigma_t \psi_j, v_i)_{\mathcal{D}_k}$	$(r \sigma_t \psi, v)_{\mathcal{D}_k}$	RZMassIntegrator( $\sigma_t$ )
7	$\frac{1}{4\pi} (r \sigma_s \phi, v_i)_{\mathcal{D}_k}$	$(r \varphi, v)_{\mathcal{D}_k}$	RZDomainLFIntegrator( $\frac{1}{4\pi} \sigma_s \phi$ )
8	$\frac{1}{4\pi} (r S_0, v_i)_{\mathcal{D}_k}$	$(r S_0, v)_{\mathcal{D}_k}$	RZDomainLFIntegrator( $\frac{S_0}{4\pi}$ )
9	$(r \Omega \cdot \hat{n} \psi_{inc}, v_i)_{\partial \mathcal{D}_k}$	$\frac{\alpha}{2} (r \psi_{inc} \Omega \cdot \hat{n}, v)_{\partial \mathcal{D}_k}$ $- \beta(r \psi_{inc}  \Omega \cdot \hat{n} , v)_{\partial \mathcal{D}_k}$	RZBoundaryFlowIntegrator( $\psi_{inc}, \Omega, \alpha, \beta$ )

Table 6: MFEM  $R$ - $Z$  transport operator function calls where the arguments have been dropped.

Table 7: MFEM default integration orders for transport operators. The notation for the finite element order is  $p$ , mesh order is  $g$ , and problem spatial dimension is  $d$ .

MFEM Integrator	Default Integration Order
DGTraceIntegrator	$g \cdot d + 2 \cdot p - 1$
ConvectionIntegrator	$g \cdot d + 2 \cdot p - 1$
MassIntegrator	$g \cdot d + 2 \cdot p - 1$
DomainLFIntegrator	$2 \cdot g$
BoundaryFlowIntegrator	$g \cdot d + 2 \cdot p - 1$

no.	FEM Equations	MFEM Equation	User Input
1	$(\sigma_a \phi, v)_{\mathcal{D}}$	$(\sigma_a \phi, v)_{\mathcal{D}}$	MassIntegrator( $\sigma_a$ )
2	$(D \nabla \phi, \nabla v)_{\mathcal{D}}$	$(D \nabla \phi, \nabla v)_{\mathcal{D}}$	DiffusionIntegrator( $D$ )
3	$(\{\{ D \partial_n \phi \}, [v] \})_{\partial \mathcal{D}^e}$ + $([\phi], \{\{ D \partial_n v \}\})_{\partial \mathcal{D}^e}$ + $(\kappa_e [\phi], [v])_{\partial \mathcal{D}^e}$	$(\{\{ D \nabla \phi \cdot \hat{n} \}, [v] \})_{\partial \mathcal{D}^e}$ + $\sigma_D ([\phi], \{\{ D \nabla v \cdot \hat{n} \}\})_{\partial \mathcal{D}^e}$ + $\kappa \left( \left\{ \left\{ \frac{D}{h_{\perp}} \right\} [\phi], [v] \right\} \right)_{\partial \mathcal{D}^e}$	DGDiffusionIntegrator( $D, \sigma_D, \kappa$ )
4	$(\{\{ D \partial_n \phi \}, [v] \})_{\partial \mathcal{D}^b}$ - $\frac{1}{2} ([\phi], \{\{ D \partial_n v \}\})_{\partial \mathcal{D}^b}$ - $\frac{1}{2} (\kappa_e [\phi], [v])_{\partial \mathcal{D}^b}$	$(\{\{ D \nabla \phi \cdot \hat{n} \}, [v] \})_{\partial \mathcal{D}^b}$ + $\sigma_D ([\phi], \{\{ D \nabla v \cdot \hat{n} \}\})_{\partial \mathcal{D}^b}$ + $\kappa \left( \left\{ \left\{ \frac{D}{h_{\perp}} \right\} [\phi], [v] \right\} \right)_{\partial \mathcal{D}^b}$	DGDiffusionIntegrator( $D, \sigma_D, \kappa$ )
5	$(\sigma_s [\phi^{(\ell+1/2)} - \phi^{(\ell)}], v)_{\mathcal{D}}$	$(Q_0, v)_{\mathcal{D}}$	DomainLFIntegrator( $Q_0$ )
6	$\left( \frac{1}{2} \phi, v \right)_{\partial \mathcal{D}^b}$	$\left( \frac{1}{2} \phi, v \right)_{\partial \mathcal{D}^b}$	BoundaryMassIntegrator( $\frac{1}{2}$ )

Table 8: MFEM diffusion equation function calls.

## B Mesh Examples

## C Supplementary Results in $X-Y$ Geometry

In this section, we present additional results in  $X-Y$  geometry to supplement the work done in Woods [27]. Some of this work appears in Woods et al. [70].

### C.1 Uniform Infinite Medium

We solved a uniform infinite medium problem on a high-order mesh that has sufficient curvature to have incident and outgoing angular fluxes on some mesh surfaces for the same angular direction  $\Omega$ . The mesh is overlaid on top of the solution in Figure 80.

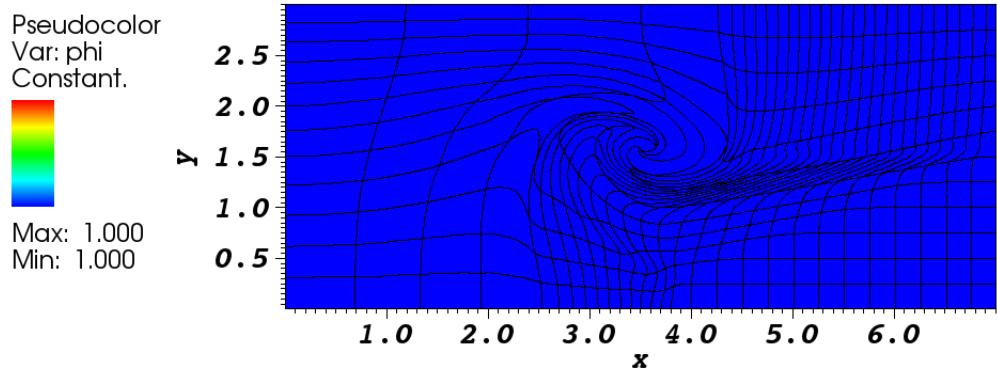


Figure 80: Uniform infinite medium scalar flux solution.

### C.2 Spatial Convergence Study

We use the manufactured solution

$$\psi(x, y, \mu, \eta) = (1 - \mu^2)(1 - \eta^2) \sin(\alpha\pi x) \cos(\beta\pi y) \quad (91)$$

on a *highly* curved mesh with  $\alpha = 4$  and  $\beta = 7/2$ . The solution using  $p = 4$  and  $S_{12}$  level-symmetric angular quadrature is shown in Figure 81 with the coarsest mesh overlaid. Figure 82 shows the errors from a spatial convergence study with select

reference lines. For coarser meshes, we observe degraded convergence rates as low as  $O(1/2)$ . As the mesh is refined, the convergence rates tend toward  $O(p + 1)$ . This is likely the effect of zones tending to have fewer surfaces that have both incident and outgoing intensities for any given  $\Omega_m \cdot \hat{n}(\mathbf{x})$  as the mesh is refined. Figure 82 reveals that the error for any given mesh refinement is reduced with higher-order finite elements. Inspection of the first mesh refinement step shows that the spatial convergence rate for higher-order finite elements is not as degraded as lower-order methods.

This particular solution has a scattering and external source so the solution is not discontinuous within the zone but rather has a function whose first derivative is discontinuous along some surfaces. The  $O(1/2)$  convergence rate is similar to the convergence rate of solutions that are discontinuous within a mesh zone [24]. In this work, we numerically compute all integrals with Gaussian quadrature, which does not accurately integrate functions with discontinuous derivatives.

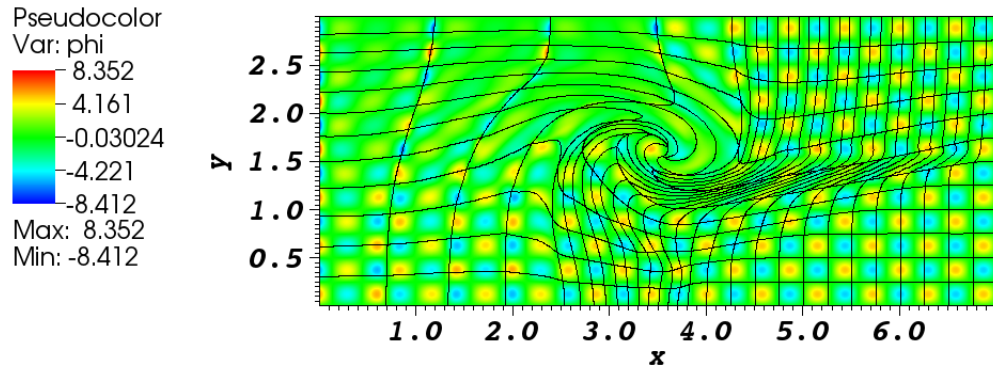


Figure 81: MMS on a *highly* curved mesh.

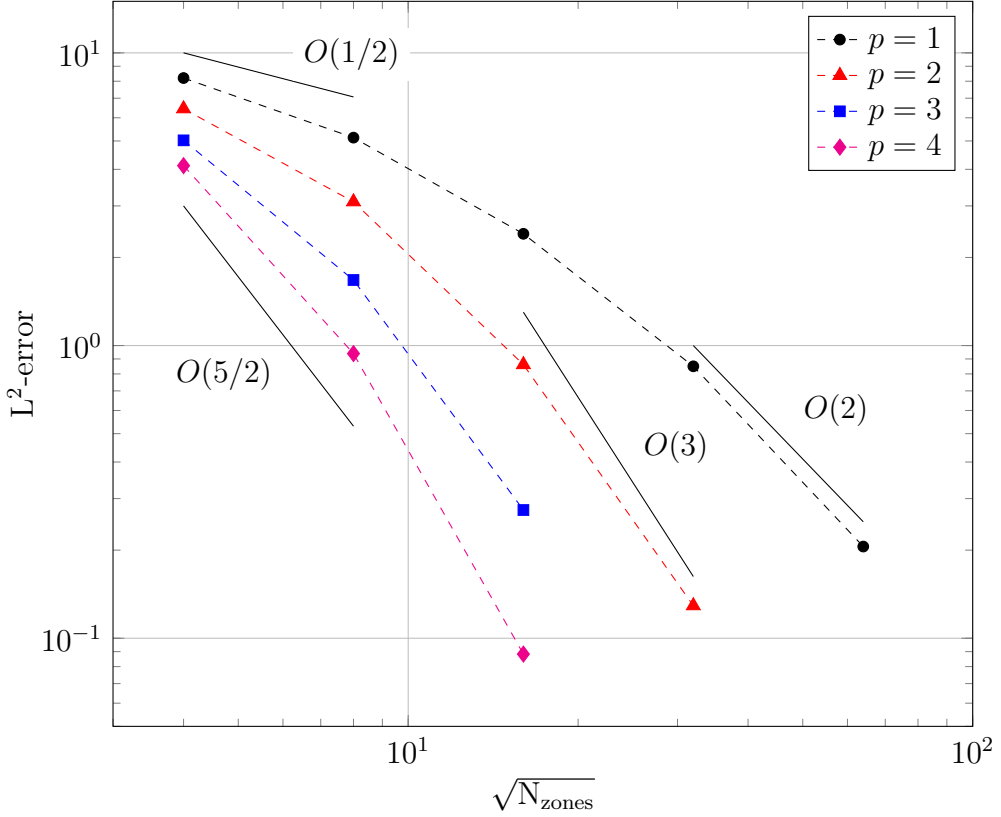
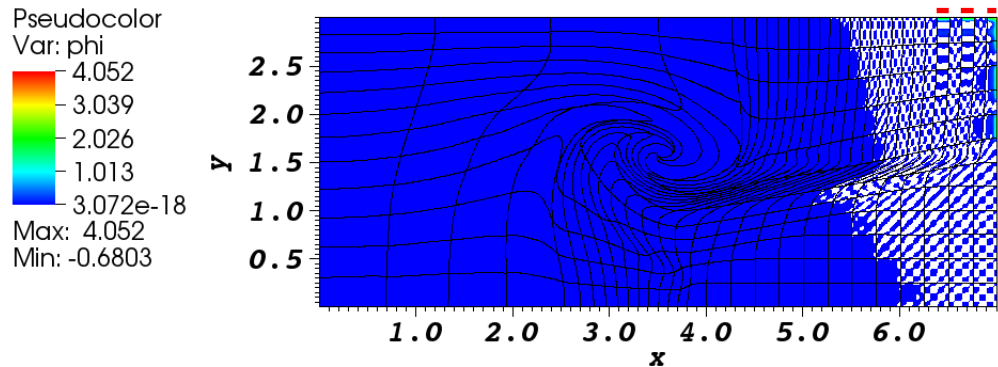


Figure 82: Errors between the manufactured and DFEM solutions. Reference lines depict order of spatial convergence  $O(n) \equiv O((N_{\text{zones}})^{n/2})$ .

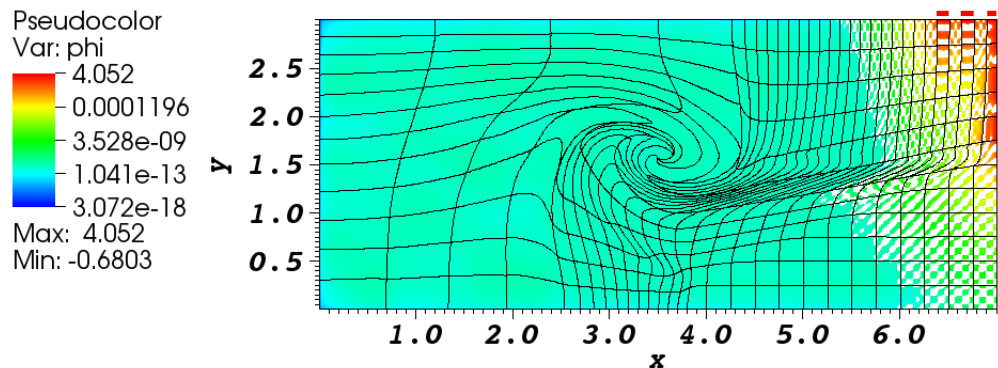
### C.3 Alternating Incident Boundary Condition

Figure 83 demonstrates the solution to an alternating incident angular flux problem similar to what appears in Woods [27] and Woods et al. [26]. Adams [41] and Palmer and Adams [42] demonstrate that transport solutions in the optically thick diffusion limit that have anisotropic and/or discontinuous incident fluxes can permit unphysical oscillations in the interior solution. The material is defined by  $\sigma_t = 1000$ ,  $\sigma_s = 0.999\sigma_t$ , and  $S_0 = 0$ . We solved this using 4<sup>th</sup>-order finite elements and  $S_{12}$  level-symmetric angular quadrature. These solutions demonstrate that a boundary layer is created by the discontinuous incident flux and propagates into the problem interior. These oscillations dip below zero and are non-physical. The oscillations do not reach

the region of interest so we alter this problem.



(a) Scalar flux; red bars denote incident boundary locations.

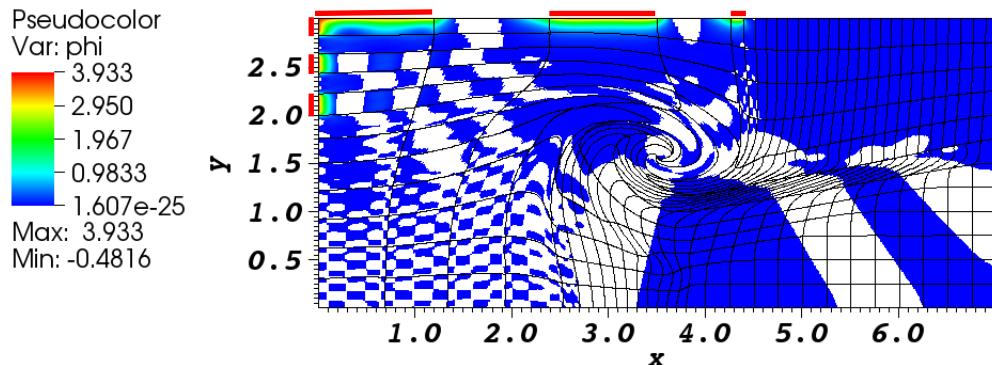


(b) Log of scalar flux solution; red bars denote incident boundary locations.

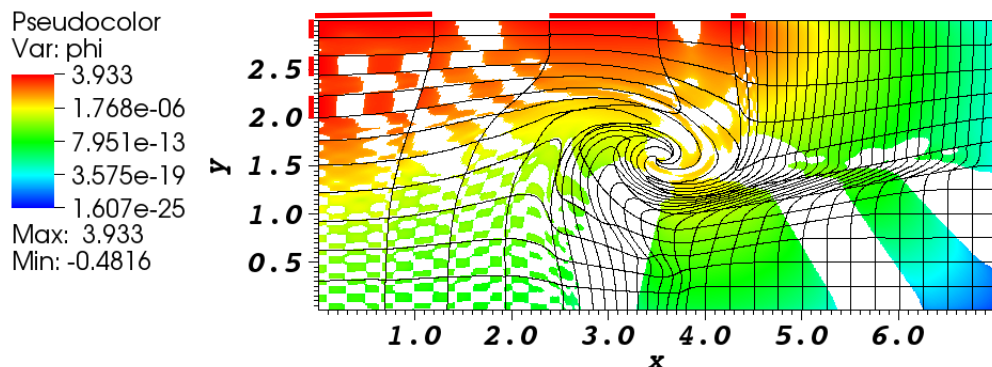
Figure 83: Alternating incident flux problem solution.

We solve a similar problem with the incident boundary condition locations in the upper right of the problem. Figure 84 shows the scalar flux solution with red bars denoting the incident flux locations. The material is defined by  $\sigma_t = 250$ ,  $\sigma_s = 0.999\sigma_t$ , and  $S_0 = 0$ . We solved this using 4<sup>th</sup>-order finite elements and  $S_{12}$  level-symmetric angular quadrature. The total cross-section was reduced for this problem so that there are some mesh zones that the zones in the bottom right region have comparable mfp

sizes compared to the problem described by Figure 74. We observe oscillations that dip below zero throughout the solution, however they are preferentially in the zones that have larger mfp sizes (i.e., left side of the mesh). Many of the zones comprising the spiral are large in this sense and exhibit the oscillations. An interesting result is that these oscillations are propagated away from the boundaries of spiral region.



(a) Scalar flux; red bars denote incident boundary locations.



(b) Log of the scalar flux; red bars denote incident boundary locations.

Figure 84: Scalar flux solution to alternating incident flux problem.

## D Alternative Implementations for DSA with Robin Boundary Conditions

We considered two other implementations for the Robin boundary conditions. Method 1 substitutes Equation 25 into Equation 16a:

$$\begin{aligned} b_{MIP,1}(\varphi, v) = & (\sigma_a \varphi, v)_D + (D \nabla \varphi, \nabla v)_D \\ & + (\kappa_e [\![\varphi]\!], [\![v]\!])_{\partial D^e} + ([\![\varphi]\!], \{D \partial_n v\})_{\partial D^e} + (\{D \partial_n \varphi\}, [\![v]\!])_{\partial D^e} \\ & + (\kappa_e \varphi, v)_{\partial D^b} - \frac{1}{2} (\varphi, D \partial_n v)_{\partial D^b} + \frac{1}{4} (\varphi, v)_{\partial D^b} \end{aligned} \quad (92)$$

Method 2 is very similar to Method 1 with one term removed:

$$\begin{aligned} b_{MIP,2}(\varphi, v) = & (\sigma_a \varphi, v)_D + (D \nabla \varphi, \nabla v)_D \\ & + (\kappa_e [\![\varphi]\!], [\![v]\!])_{\partial D^e} + ([\![\varphi]\!], \{D \partial_n v\})_{\partial D^e} + (\{D \partial_n \varphi\}, [\![v]\!])_{\partial D^e} \\ & + (\kappa_e \varphi, v)_{\partial D^b} + \frac{1}{4} (\varphi, v)_{\partial D^b} \end{aligned} \quad (93)$$

Method 3 is the Robin boundary condition we implemented in Section 3.2. An analytic one-dimensional diffusion equation solution with zero incident current boundary conditions was used to benchmark the solution to the diffusion equation using three proposed Robin boundary condition methods. The original MIP DSA method (Equation 16a) was also solved for comparison. The analytic solution to the 1-D

diffusion equation with homogeneous Robin boundary conditions is

$$\phi(x) = c_1 e^{x/L} + c_2 e^{-x/L} + \frac{S_0}{\sigma_a} \quad (94)$$

$$c_1 = \frac{1}{4} \frac{S_0}{\sigma_a} \left[ \left( \frac{1}{4} + \frac{1}{2} \frac{D}{L} \right) e^{1/L} - \left( \frac{1}{4} - \frac{1}{2} \frac{D}{L} \right) \right] \left[ \left( \frac{1}{4} - \frac{1}{2} \frac{D}{L} \right)^2 - \left( \frac{1}{4} + \frac{1}{2} \frac{D}{L} \right)^2 e^{2/L} \right]^{-1} \quad (95)$$

$$c_2 = \left[ -c_1 \left( \frac{1}{4} + \frac{1}{2} \frac{D}{L} \right) e^{1/L} - \frac{1}{4} \frac{S_0}{\sigma_a} \right] e^{1/L} \left( \frac{1}{4} - \frac{1}{2} \frac{D}{L} \right)^{-1} \quad (96)$$

where  $L^2 = D/\sigma_a$ . The opacities and source values were  $\sigma_t = 1/\varepsilon$ ,  $\sigma_a = \varepsilon$ ,  $S_0 = \varepsilon$ , and  $D = 1/(3\sigma_t)$ . A first-order orthogonal mesh, 3<sup>rd</sup> order finite elements,  $S_8$  level-symmetric angular quadrature, and convergence criteria (see Eq. 15)  $\varepsilon_{\text{conv}} = 10^{-10}$  were used. Table 9 summarizes the  $L_2$  norm of the errors between the FEM diffusion equation solution and the analytic solution. Method 1 (Eq. 92), Method 2 (Eq. 93), and the MIP DSA method solve the problem with increasing accuracy as the problem gets more optically thick (i.e.  $\varepsilon \rightarrow 0$ ). The accuracy of Method 3 appears to be significantly less dependent on the optical thickness of the problem. However, we do observe the accuracy is slightly reduced as the problem becomes optically thick. Method 3 is the most accurate discretization in all the problems considered here.

Table 9:  $L_2$  norm of the errors between the diffusion equation using the given boundary condition method and the reference solution (1-D analytic solution) using 3<sup>rd</sup>-order elements,  $C = 4$ , on an orthogonal mesh with 2304 zones.

$\varepsilon$	Method 1	Method 2	Method 3	MIP DSA
10	0.722	0.722	$4.05 \times 10^{-11}$	0.722
1	0.363	0.363	$2.03 \times 10^{-10}$	0.363
0.1	0.0607	0.0606	$3.39 \times 10^{-10}$	0.0607
0.01	0.00650	0.00647	$3.63 \times 10^{-10}$	0.00650
$1 \times 10^{-3}$	$6.55 \times 10^{-4}$	$6.21 \times 10^{-4}$	$3.66 \times 10^{-10}$	$6.55 \times 10^{-4}$
$1 \times 10^{-4}$	$6.56 \times 10^{-5}$	$4.25 \times 10^{-5}$	$3.66 \times 10^{-10}$	$6.56 \times 10^{-5}$
$1 \times 10^{-5}$	$6.56 \times 10^{-6}$	$2.19 \times 10^{-6}$	$3.67 \times 10^{-10}$	$6.54 \times 10^{-6}$
$1 \times 10^{-6}$	$6.56 \times 10^{-7}$	$2.18 \times 10^{-7}$	$4.08 \times 10^{-10}$	$3.91 \times 10^{-7}$

## E Mathematica Scripts

### E.1 Mass Matrix Entries for RZ BLD Gauss-Legendre on Quadrilaterals

```
(*Mass matrix entry for RZ BLD Gauss-Legendre on quadrilaterals*)
\

Clear[r0, r1, r2, r3, z0, z1, z2, z3, mr0, mr1, mr2, mr3, mz0, mz1,
mz2, mz3]

(*Define physical integration point coordinates to compare to MFEM \
output:r0=(1+(-Sqrt[1/3]))/(1-(-1))*(0.25-0);
r1=(1+(Sqrt[1/3]))/(1-(-1))*(0.25-0);
z0=(1+(-Sqrt[1/3]))/(1-(-1))*(0.25-0);
z3=(1+(Sqrt[1/3]))/(1-(-1))*(0.25-0);*)

(*These make the mesh \

```

```

rectangular:*)
z2 := z3
z1 := z0
r2 := r1
r3 := r0
(*Quadrilateral transformation back to reference square-more general \
than rectangle transofrmation-but NOT curved mesh*)

r[rho_, kappa_] := (r1 - r0) rho + (r3 - r0) kappa + (r2 + r0 - r1 -
r3) rho kappa + r0
z[rho_, kappa_] := (z1 - z0) rho + (z3 - z0) kappa + (z2 + z0 - z1 -
z3) rho kappa + z0

(*Mesh nodes are needed to conserve cell volume.Cannot define mr0=0 \
nor mz0=0 here.Perform integration and then set the values.*)
\

(*Comment out to get the general mesh element mr1=0.25;
mz3=0.25;*)

mr2 := mr1
mr3 := mr0
mz1 := mz0
mz2 := mz3
mr[rho_, kappa_] := (mr1 - mr0) rho + (mr3 - mr0) kappa + (mr2 + mr0 -
mr1 - mr3) rho kappa + mr0
mz[rho_, kappa_] := (mz1 - mz0) rho + (mz3 - mz0) kappa + (mz2 + mz0 -
mz1 - mz3) rho kappa + mz0

```

```

a = {mr[rho, kappa], mz[rho, kappa]};

b = {rho, kappa};

(*Determinant of the Jacobian-for determining area of the physical \
element.*)

j = Det[D[a, {b}]];

(*Basis functions.The coefficients are from MATLAB script \
"GaussLegendreQuadrilateral.m".*)

BLD1[rho_, kappa_] :=
  3*rho*kappa - (3 + Sqrt[3])/2*rho - (3 + Sqrt[3])/2*
    kappa + (1 + Sqrt[3]/2)

BLD2[rho_, kappa_] := -3*rho*kappa + (3 + Sqrt[3])/2*rho +
  3/(3 + Sqrt[3])*kappa - 0.5

BLD3[rho_, kappa_] :=
  3*rho*kappa - 3/(3 + Sqrt[3])*rho -
  3/(3 + Sqrt[3])*kappa + (1 - Sqrt[3]/2)

BLD4[rho_, kappa_] := -3*rho*kappa +
  3/(3 + Sqrt[3])*rho + (3 + Sqrt[3])/2*kappa - 0.5

(*Check for orthogonality.*)

BLD1[r0, z0]*BLD2[r0, z0];

(*The r variable gets transformed back to the reference element*)

M =
  Integrate[
    mr[rho, kappa]*BLD1[rho, kappa]*BLD1[rho, kappa]*j, {rho, 0,
    1}, {kappa, 0, 1}]

```

```

mr0 = 0.25;
mz0 = 0.25;
mr1 = 0.5;
mz3 = 0.5;

```

M

## E.2 Angular Redistribution Matrix Entries for RZ BLD Gauss-Legendre on Quadrilaterals

```

(*Angular Redistribution matrix for RZ BLD Gauss-Legendre on \
quadrilaterals*)Clear[r0, r1, r2, r3, z0, z1, z2, z3, mr0, mr1, mr2, \
mr3, mz0, mz1, mz2, mz3]

(*Define physical integration point coordinates to compare to MFEM \
output:r0=(1+(-Sqrt[1/3]))/(1-(-1))*(0.25-0);
r1=(1+(Sqrt[1/3]))/(1-(-1))*(0.25-0);
z0=(1+(-Sqrt[1/3]))/(1-(-1))*(0.25-0);
z3=(1+(Sqrt[1/3]))/(1-(-1))*(0.25-0);*)

(*These make the mesh \
rectangular:*)
z2 := z3
z1 := z0
r2 := r1
r3 := r0

(*Quadrilateral transformation back to reference square-more general \
than rectangle transofrmation-but NOT curved mesh*)

```

```

r[rho_, kappa_] := (r1 - r0) rho + (r3 - r0) kappa + (r2 + r0 - r1 -
r3) rho kappa + r0
z[rho_, kappa_] := (z1 - z0) rho + (z3 - z0) kappa + (z2 + z0 - z1 -
z3) rho kappa + z0

(*Mesh nodes are needed to conserve cell volume.Cannot define mr0=0 \
nor mz0=0 here.Perform integration and then set the values.*)
\

(*Comment out to get the general mesh element mr1=0.25;
mz3=0.25;*)

mr2 := mr1
mr3 := mr0
mz1 := mz0
mz2 := mz3
mr[rho_, kappa_] := (mr1 - mr0) rho + (mr3 - mr0) kappa + (mr2 + mr0 -
mr1 - mr3) rho kappa + mr0
mz[rho_, kappa_] := (mz1 - mz0) rho + (mz3 - mz0) kappa + (mz2 + mz0 -
mz1 - mz3) rho kappa + mz0
a = {mr[rho, kappa], mz[rho, kappa]};
b = {rho, kappa};
(*Determinant of the Jacobian-for determining area of the physical \
element.*)
j = Det[D[a, {b}]];
(*Basis functions.The coefficients are from MATLAB script \
"GaussLegendreQuadrilateral.m"*)

```

```

BLD1[rho_, kappa_] :=

3*rho*kappa - (3 + Sqrt[3])/2*rho - (3 + Sqrt[3])/2*

kappa + (1 + Sqrt[3]/2)

BLD2[rho_, kappa_] := -3*rho*kappa + (3 + Sqrt[3])/2*rho +

3/(3 + Sqrt[3])*kappa - 1/2

BLD3[rho_, kappa_] :=

3*rho*kappa - 3/(3 + Sqrt[3])*rho -

3/(3 + Sqrt[3])*kappa + (1 - Sqrt[3]/2)

BLD4[rho_, kappa_] := -3*rho*kappa +

3/(3 + Sqrt[3])*rho + (3 + Sqrt[3])/2*kappa - 1/2

M = Integrate[

BLD1[rho, kappa]*BLD1[rho, kappa]*j, {rho, 0, 1}, {kappa, 0, 1}]

mr0 = 0;

mz0 = 0;

mr1 = 0.25;

mz3 = 0.25;

thisalpha = 0.350021175;

w = 0.523598775598298;

M*thisalpha

```

### E.3 r-Leakage Matrix Entries for RZ BLD Gauss-Legendre on Quadrilaterals

```
(*r-Leakage matrix for RZ BLD Gauss-Legendre on \
quadrilaterals*)Clear[r0, r1, r2, r3, z0, z1, z2, z3, mr0, mr1, mr2, \
mr3, mz0, mz1, mz2, mz3, mu, rho, kappa]

(*Define physical integration point coordinates to compare to MFEM \
output: *)

r0 = (1 + (-Sqrt[1/3]))/(1 - (-1))*(0.25 - 0);
r1 = (1 + (Sqrt[1/3]))/(1 - (-1))*(0.25 - 0);
z0 = (1 + (-Sqrt[1/3]))/(1 - (-1))*(0.25 - 0);
z3 = (1 + (Sqrt[1/3]))/(1 - (-1))*(0.25 - 0);

(*Use to define rectangular mesh:*)

r2 = r1;
r3 = r0;
z1 = z0;
z2 = z3;

(*Transform arbitrary quadrilateral to reference square*)

r[rho_, kappa_] := (r1 - r0) rho + (r3 - r0) kappa + (r2 + r0 - r1 - \
r3) rho kappa + r0
z[rho_, kappa_] := (z1 - z0) rho + (z3 - z0) kappa + (z2 + z0 - z1 - \
z3) rho kappa + z0

(*Mesh nodes are needed to conserve cell volume. Cannot define mr0=0 \
nor mz0=0 here. Perform integration and then set the values.*)

\
```

```

(*Comment out to get the general mesh element mr1=0.25;
mz3=0.25;*)

mr2 := mr1

mr3 := mr0

mz1 := mz0

mz2 := mz3

mr[rho_, kappa_] := (mr1 - mr0) rho + (mr3 - mr0) kappa + (mr2 + mr0 -
mr1 - mr3) rho kappa + mr0

mz[rho_, kappa_] := (mz1 - mz0) rho + (mz3 - mz0) kappa + (mz2 + mz0 -
mz1 - mz3) rho kappa + mz0

a = {mr[rho, kappa], mz[rho, kappa]};

b = {rho, kappa};

(*Determinant of the Jacobian-for determining area of the physical \
element.*)

j = Det[D[a, {b}]];

(*Basis functions.The coefficients are from MATLAB script \
"GaussLegendreQuadrilateral.m".*)

BLD1[rho_, kappa_] :=
3*rho*kappa - (3 + Sqrt[3])/2*rho - (3 + Sqrt[3])/2*
kappa + (1 + Sqrt[3]/2)

BLD2[rho_, kappa_] := -3*rho*kappa + (3 + Sqrt[3])/2*rho +
3/(3 + Sqrt[3])*kappa - 1/2

BLD3[rho_, kappa_] :=
3*rho*kappa - 3/(3 + Sqrt[3])*rho -
3/(3 + Sqrt[3])*kappa + (1 - Sqrt[3]/2)

```

```

BLD4[rho_, kappa_] := -3*rho*kappa +
3/(3 + Sqrt[3])*rho + (3 + Sqrt[3])/2*kappa - 1/2
(*The r value gets transformed back to the reference element*)

Kr = \
-mu*Integrate[
BLD1[rho, kappa]*D[BLD1[rho, kappa], rho]*j, {rho, 0, 1}, {kappa,
0, 1}]

mr0 = 0.0;
mr1 = 0.25;
mz0 = 0.0;
mz3 = 0.25;
mu = -0.495004692;
BLD1[r0, z0]
rho = r1;
D[BLD1[rho, kappa], kappa]
Kr

```

## E.4 z-Leakage Matrix Entries for RZ BLD Gauss-Legendre on Quadrilaterals

```

(*z-Leakage matrix for RZ BLD Gauss-Legendre on \
quadrilaterals*)Clear[r0, r1, r2, r3, z0, z1, z2, z3, mr0, mr1, mr2, \
mr3, mz0, mz1, mz2, mz3, xi, rho, kappa]
(*Define physical integration point coordinates to compare to MFEM \
output:*)
r0 = (1 + (-Sqrt[1/3]))/(1 - (-1))*(0.25 - 0);

```

```

r1 = (1 + (Sqrt[1/3]))/(1 - (-1))*(0.25 - 0);
z0 = (1 + (-Sqrt[1/3]))/(1 - (-1))*(0.25 - 0);
z3 = (1 + (Sqrt[1/3]))/(1 - (-1))*(0.25 - 0);

(*Use to define rectangular mesh*)
r2 = r1;
r3 = r0;
z1 = z0;
z2 = z3;

(*Transform arbitrary quadrilateral to reference square*)

r[rho_, kappa_] := (r1 - r0) rho + (r3 - r0) kappa + (r2 + r0 - r1 -
r3) rho kappa + r0
z[rho_, kappa_] := (z1 - z0) rho + (z3 - z0) kappa + (z2 + z0 - z1 -
z3) rho kappa + z0

(*Mesh nodes are needed to conserve cell volume.Cannot define mr0=0 \
nor mz0=0 here.Perform integration and then set the values.*)
\

(*Comment out to get the general mesh element mr1=0.25;
mz3=0.25;*)

mr2 := mr1
mr3 := mr0
mz1 := mz0
mz2 := mz3
mr[rho_, kappa_] := (mr1 - mr0) rho + (mr3 - mr0) kappa + (mr2 + mr0 -
mr1 - mr3) rho kappa + mr0

```

```

mz[rho_, kappa_] := (mz1 - mz0) rho + (mz3 - mz0) kappa + (mz2 + mz0 -
mz1 - mz3) rho kappa + mz0
a = {mr[rho, kappa], mz[rho, kappa]};
b = {rho, kappa};

(*Determinant of the Jacobian-for determining area of the physical \
element.*)

j = Det[D[a, {b}]];
(*Basis functions.The coefficients are from MATLAB script \
"GaussLegendreQuadrilateral.m".*)

BLD1[rho_, kappa_] :=
3*rho*kappa - (3 + Sqrt[3])/2*rho - (3 + Sqrt[3])/2*
kappa + (1 + Sqrt[3]/2)

BLD2[rho_, kappa_] := -3*rho*kappa + (3 + Sqrt[3])/2*rho +
3/(3 + Sqrt[3])*kappa - 1/2

BLD3[rho_, kappa_] :=
3*rho*kappa - 3/(3 + Sqrt[3])*rho -
3/(3 + Sqrt[3])*kappa + (1 - Sqrt[3]/2)

BLD4[rho_, kappa_] := -3*rho*kappa +
3/(3 + Sqrt[3])*rho + (3 + Sqrt[3])/2*kappa - 1/2

(*The r value gets transformed back to the reference element*)

Kz = \
-xi*Integrate[
BLD1[rho, kappa]*D[BLD1[rho, kappa], kappa]*j, {rho, 0, 1}, {kappa,
0, 1}]

mr0 = 0.0;

```

```

mr1 = 0.25;
mz0 = 0.0;
mz3 = 0.25;
xi = -0.868890301;
D[BLD1[rho, kappa], kappa]
xi*j
Kz
Kr + Kz

```

## E.5 z-Leakage Matrix Entries for RZ BLD Gauss-Legendre on Quadrilaterals

```

(*z-Leakage matrix for RZ BLD Gauss-Legendre on \
quadrilaterals*)Clear[r0, r1, r2, r3, z0, z1, z2, z3, mr0, mr1, mr2, \
mr3, mz0, mz1, mz2, mz3, xi, rho, kappa]
(*Define physical integration point coordinates to compare to MFEM \
output:*)
r0 = (1 + (-Sqrt[1/3]))/(1 - (-1))*(0.25 - 0);
r1 = (1 + (Sqrt[1/3]))/(1 - (-1))*(0.25 - 0);
z0 = (1 + (-Sqrt[1/3]))/(1 - (-1))*(0.25 - 0);
z3 = (1 + (Sqrt[1/3]))/(1 - (-1))*(0.25 - 0);

(*Use to define rectangular mesh:*)
r2 = r1;
r3 = r0;
z1 = z0;

```

```

z2 = z3;

(*Transform arbitrary quadrilateral to reference square*)

r[rho_, kappa_] := (r1 - r0) rho + (r3 - r0) kappa + (r2 + r0 - r1 -
r3) rho kappa + r0
z[rho_, kappa_] := (z1 - z0) rho + (z3 - z0) kappa + (z2 + z0 - z1 -
z3) rho kappa + z0

(*Mesh nodes are needed to conserve cell volume.Cannot define mr0=0 \
nor mz0=0 here.Perform integration and then set the values.*)

\

(*Comment out to get the general mesh element mr1=0.25;
mz3=0.25;*)

mr2 := mr1
mr3 := mr0
mz1 := mz0
mz2 := mz3

mr[rho_, kappa_] := (mr1 - mr0) rho + (mr3 - mr0) kappa + (mr2 + mr0 -
mr1 - mr3) rho kappa + mr0
mz[rho_, kappa_] := (mz1 - mz0) rho + (mz3 - mz0) kappa + (mz2 + mz0 -
mz1 - mz3) rho kappa + mz0

a = {mr[rho, kappa], mz[rho, kappa]};
b = {rho, kappa};

(*Determinant of the Jacobian-for determining area of the physical \
element.*)

j = Det[D[a, {b}]];
(*Basis functions.The coefficients are from MATLAB script \

```

```

"GaussLegendreQuadrilateral.m"*)

```

$$\text{BLD1}[\rho, \kappa] := \frac{3\rho\kappa - (3 + \sqrt{3})/2}{(3 + \sqrt{3})/2} - \frac{(1 + \sqrt{3})/2}{(1 + \sqrt{3})/2}$$

$$\text{BLD2}[\rho, \kappa] := -\frac{3\rho\kappa + (3 + \sqrt{3})/2}{(3 + \sqrt{3})/2} + \frac{1/2}{(3 + \sqrt{3})/2}$$

$$\text{BLD3}[\rho, \kappa] := \frac{3\rho\kappa - 3/(3 + \sqrt{3})\rho}{(3 + \sqrt{3})/2} - \frac{(1 - \sqrt{3})/2}{(1 - \sqrt{3})/2}$$

$$\text{BLD4}[\rho, \kappa] := -\frac{3\rho\kappa + (3 + \sqrt{3})/2}{(3 + \sqrt{3})/2} + \frac{1/2}{(3 + \sqrt{3})/2}$$

(\*The r value gets transformed back to the reference element\*)

$$Kz = \text{Integrate}[-\xi \cdot \text{D}[\text{BLD1}[\rho, \kappa], \kappa] \cdot j, \{\rho, 0, 1\}, \{\kappa, 0, 1\}]$$

$$mr0 = 0.0;$$

$$mr1 = 0.25;$$

$$mz0 = 0.0;$$

$$mz3 = 0.25;$$

$$\xi = -0.868890301;$$

$$D[\text{BLD1}[\rho, \kappa], \kappa]$$

$$\xi \cdot j$$

$$Kz$$

$$Kr + Kz$$

## E.6 r Surface-Integral Matrix Entries for RZ BLD Gauss-Legendre on Quadrilaterals

```
(*r surface-integral matrix for RZ BLD Gauss-Legendre on \
quadrilaterals*)

Clear[r0, r1, r2, r3, z0, z1, z2, z3]

(*Define physical integration point coordinates to compare to MFEM \
output:

r0=(1+(-Sqrt[1/3]))/(1-(-1))*(0.25-0);
r1=(1+(Sqrt[1/3]))/(1-(-1))*(0.25-0);
z0=(1+(-Sqrt[1/3]))/(1-(-1))*(0.25-0);
z3=(1+(Sqrt[1/3]))/(1-(-1))*(0.25-0);*)

(*Use to define rectangular \
mesh:*)
r2 = r1;
r3 = r0;
z1 = z0;
z2 = z3;

(*Transform arbitrary quadrilateral to reference square*)

r[rho_, kappa_] := (r1 - r0) rho + (r3 - r0) kappa + (r2 + r0 - r1 -
r3) rho kappa + r0
z[rho_, kappa_] := (z1 - z0) rho + (z3 - z0) kappa + (z2 + z0 - z1 -
z3) rho kappa + z0
a = {r[rho, kappa], z[rho, kappa]};
b = {rho, kappa};
```

```

(*Determinant of the Jacobian-for determining area of the physical \
element.*)

j = Det[D[a, {b}]] ;

(*Basis functions.The coefficients are from MATLAB script \
"GaussLegendreQuadrilateral.m".*)

BLD1[rho_, kappa_] :=
3*rho*kappa - (3 + Sqrt[3])/2*rho - (3 + Sqrt[3])/2*
kappa + (1 + Sqrt[3]/2)

BLD2[rho_, kappa_] := -3*rho*kappa + (3 + Sqrt[3])/2*rho +
3/(3 + Sqrt[3])*kappa - 1/2

BLD3[rho_, kappa_] :=
3*rho*kappa - 3/(3 + Sqrt[3])*rho -
3/(3 + Sqrt[3])*kappa + (1 - Sqrt[3]/2)

BLD4[rho_, kappa_] := -3*rho*kappa +
3/(3 + Sqrt[3])*rho + (3 + Sqrt[3])/2*kappa - 1/2

(*The r value gets transformed back to the reference element*)

Lr =
Integrate[r1*BLD1[1, kappa]*BLD1[1, kappa]*j, {kappa, 0, 1}] -
Integrate[r0*BLD1[0, kappa]*BLD1[0, kappa]*j, {kappa, 0, 1}]

r0 = 0.0;
r1 = 0.25;
z0 = 0.0;
z3 = 0.25;

```

## E.7 z Surface-Integral Matrix Entries for RZ BLD Gauss-Legendre on Quadrilaterals

```
(*z surface-integral matrix for RZ BLD Gauss-Legendre on \
quadrilaterals*)

Clear[r0, r1, r2, r3, z0, z1, z2, z3]

(*Define physical integration point coordinates to compare to MFEM \
output:

r0=(1+(-Sqrt[1/3]))/(1-(-1))*(0.25-0);
r1=(1+(Sqrt[1/3]))/(1-(-1))*(0.25-0);
z0=(1+(-Sqrt[1/3]))/(1-(-1))*(0.25-0);
z3=(1+(Sqrt[1/3]))/(1-(-1))*(0.25-0);*)

(*Use to define rectangular \
mesh:*)
r2 = r1;
r3 = r0;
z1 = z0;
z2 = z3;

(*Transform arbitrary quadrilateral to reference square*)

r[rho_, kappa_] := (r1 - r0) rho + (r3 - r0) kappa + (r2 + r0 - r1 -
r3) rho kappa + r0
z[rho_, kappa_] := (z1 - z0) rho + (z3 - z0) kappa + (z2 + z0 - z1 -
z3) rho kappa + z0
a = {r[rho, kappa], z[rho, kappa]};
b = {rho, kappa};
```

```

(*Determinant of the Jacobian-for determining area of the physical \
element.*)

j = Det[D[a, {b}]];

(*Basis functions.The coefficients are from MATLAB script \
"GaussLegendreQuadrilateral.m".*)

BLD1[rho_, kappa_] :=
  3*rho*kappa - (3 + Sqrt[3])/2*rho - (3 + Sqrt[3])/2*
    kappa + (1 + Sqrt[3]/2)

BLD2[rho_, kappa_] := -3*rho*kappa + (3 + Sqrt[3])/2*rho +
  3/(3 + Sqrt[3])*kappa - 1/2

BLD3[rho_, kappa_] :=
  3*rho*kappa - 3/(3 + Sqrt[3])*rho -
  3/(3 + Sqrt[3])*kappa + (1 - Sqrt[3]/2)

BLD4[rho_, kappa_] := -3*rho*kappa +
  3/(3 + Sqrt[3])*rho + (3 + Sqrt[3])/2*kappa - 1/2

(*The r value gets transformed back to the reference element*)

Lz =
  Integrate[r[rho, 1]*BLD1[rho, 1]*BLD1[rho, 1]*j, {rho, 0, 1}] -
  Integrate[r[rho, 0]*BLD1[rho, 0]*BLD1[rho, 0]*j, {rho, 0, 1}]

r0 = 0.0;
r1 = 0.25;
z0 = 0.0;
z3 = 0.25;

Lz
Lr + Lz

```

## E.8 LinearForm Angular Redistribution Matrix Entries for RZ BLD Gauss-Legendre on Quadrilaterals

```
(*LinearForm Angular Redistribution matrix for RZ BLD Gauss-Legendre \
on quadrilaterals*)Clear[r0, r1, r2, r3, z0, z1, z2, z3, mr0, mr1, \
mr2, mr3, mz0, mz1, mz2, mz3]

(*Define physical integration point coordinates to compare to MFEM \
output:r0=(1+(-Sqrt[1/3]))/(1-(-1))*(0.25-0);
r1=(1+(Sqrt[1/3]))/(1-(-1))*(0.25-0);
z0=(1+(-Sqrt[1/3]))/(1-(-1))*(0.25-0);
z3=(1+(Sqrt[1/3]))/(1-(-1))*(0.25-0);*)

(*These make the mesh \
rectangular:*)
z2 := z3
z1 := z0
r2 := r1
r3 := r0

(*Quadrilateral transformation back to reference square-more general \
than rectangle transofrmation-but NOT curved mesh*)

r[rho_, kappa_] := (r1 - r0) rho + (r3 - r0) kappa + (r2 + r0 - r1 - \
r3) rho kappa + r0
z[rho_, kappa_] := (z1 - z0) rho + (z3 - z0) kappa + (z2 + z0 - z1 - \
z3) rho kappa + z0

(*Mesh nodes are needed to conserve cell volume.Cannot define mr0=0 \
```

```

nor mz0=0 here.Perform integration and then set the values.*)
\

(*Comment out to get the general mesh element mr1=0.25;
mz3=0.25;*)

mr2 := mr1

mr3 := mr0

mz1 := mz0

mz2 := mz3

mr[rho_, kappa_] := (mr1 - mr0) rho + (mr3 - mr0) kappa + (mr2 + mr0 -
mr1 - mr3) rho kappa + mr0

mz[rho_, kappa_] := (mz1 - mz0) rho + (mz3 - mz0) kappa + (mz2 + mz0 -
mz1 - mz3) rho kappa + mz0

a = {mr[rho, kappa], mz[rho, kappa]};

b = {rho, kappa};

(*Determinant of the Jacobian-for determining area of the physical \
element.*)

j = Det[D[a, {b}]];

(*Basis functions.The coefficients are from MATLAB script \
"GaussLegendreQuadrilateral.m".*)

BLD1[rho_, kappa_] :=
3*rho*kappa - (3 + Sqrt[3])/2*rho - (3 + Sqrt[3])/2*
kappa + (1 + Sqrt[3])/2

BLD2[rho_, kappa_] := -3*rho*kappa + (3 + Sqrt[3])/2*rho +
3/(3 + Sqrt[3])*kappa - 1/2

BLD3[rho_, kappa_] :=

```

```

3*rho*kappa - 3/(3 + Sqrt[3])*rho -
3/(3 + Sqrt[3])*kappa + (1 - Sqrt[3]/2)

BLD4[rho_, kappa_] := -3*rho*kappa +
3/(3 + Sqrt[3])*rho + (3 + Sqrt[3])/2*kappa - 1/2

M = Integrate[
BLD2[rho, kappa]*BLD2[rho, kappa]*j, {rho, 0, 1}, {kappa, 0, 1}]

mr0 = 0;
mz0 = 0;
mr1 = 0.25;
mz3 = 0.25;

alphatau = 0.845025867;
psiMinusHalf = 0.1591549;
M*alphatau*psiMinusHalf

```

## E.9 LinearForm Scattering/Fixed Source Matrix Entries for RZ BLD Gauss-Legendre on Quadrilaterals

```

(*LinearForm scattering/fixed sources for RZ BLD Gauss-Legendre on \
quadrilaterals*)Clear[r0, r1, r2, r3, z0, z1, z2, z3, mr0, mr1, mr2, \
mr3, mz0, mz1, mz2, mz3, Source]

(*Define physical integration point coordinates to compare to MFEM \
output:r0=(1+(-Sqrt[1/3]))/(1-(-1))*(0.25-0);
r1=(1+(Sqrt[1/3]))/(1-(-1))*(0.25-0);
z0=(1+(-Sqrt[1/3]))/(1-(-1))*(0.25-0);
```

```

z3=(1+(Sqrt[1/3]))/(1-(-1))*(0.25-0);*)

(*These make the mesh \
rectangular:*)

z2 := z3

z1 := z0

r2 := r1

r3 := r0

(*Quadrilateral transformation back to reference square-more general \
than rectangle transofrmation-but NOT curved mesh*)

r[rho_, kappa_] := (r1 - r0) rho + (r3 - r0) kappa + (r2 + r0 - r1 -
r3) rho kappa + r0

z[rho_, kappa_] := (z1 - z0) rho + (z3 - z0) kappa + (z2 + z0 - z1 -
z3) rho kappa + z0

(*Mesh nodes are needed to conserve cell volume.Cannot define mr0=0 \
nor mz0=0 here.Perform integration and then set the values.*)

\

(*Comment out to get the general mesh element mr1=0.25;
mz3=0.25;*)

mr2 := mr1

mr3 := mr0

mz1 := mz0

mz2 := mz3

mr[rho_, kappa_] := (mr1 - mr0) rho + (mr3 - mr0) kappa + (mr2 + mr0 -
mr1 - mr3) rho kappa + mr0

```

```

mz[rho_, kappa_] := (mz1 - mz0) rho + (mz3 - mz0) kappa + (mz2 + mz0 -
mz1 - mz3) rho kappa + mz0
a = {mr[rho, kappa], mz[rho, kappa]};
b = {rho, kappa};
(*Determinant of the Jacobian-for determining area of the physical \
element.*)
j = Det[D[a, {b}]];
(*Basis functions.The coefficients are from MATLAB script \
"GaussLegendreQuadrilateral.m".*)

```

```

BLD1[rho_, kappa_] :=
3*rho*kappa - (3 + Sqrt[3])/2*rho - (3 + Sqrt[3])/2*
kappa + (1 + Sqrt[3]/2)
BLD2[rho_, kappa_] := -3*rho*kappa + (3 + Sqrt[3])/2*rho +
3/(3 + Sqrt[3])*kappa - 1/2
BLD3[rho_, kappa_] :=
3*rho*kappa - 3/(3 + Sqrt[3])*rho -
3/(3 + Sqrt[3])*kappa + (1 - Sqrt[3]/2)
BLD4[rho_, kappa_] := -3*rho*kappa +
3/(3 + Sqrt[3])*rho + (3 + Sqrt[3])/2*kappa - 1/2
M = Integrate[
Source*mr[rho, kappa]*BLD2[rho, kappa]*j, {rho, 0, 1}, {kappa, 0, 1}]
(*Source=0.7/(2*Pi);*)
Source = (0.3*1)/(2*Pi);
mr0 = 0;
mz0 = 0;

```

mr1 = 0.25;

mz3 = 0.25;

M